Università Politecnica delle Marche
Scuola di Dottorato di Ricerca in Scienze dell'Ingegneria
Curriculum in Ingegneria Civile, Ambientale, Edile e Architettura

---

Existing Bridge Vulnerabilities:

The Case of Prestressed RC Dapped-end Beams

Ph.D. Dissertation of:

Riccardo Martini

Advisor:

Prof. Fabrizio Gara

Co-Advisor:

Prof. Sandro Carbonari

XXXVI edition

Abstract

The safety of existing bridges has assumed a primary role over the years, especially after recent disasters involving various structures both domestically and internationally. For the risk assessment and management of existing bridges, Italy has adopted a new multi-level risk-based approach. For proper risk assessment, evaluating the vulnerability and defects of the structures through visual inspections assumes a key role in this approach. The results of an extensive campaign of visual inspections, carried out as part of the research project involving the Università Politecnica delle Marche, the inter-university consortium FABRE and the road network owner ANAS, highlight the main issues found on existing bridges. The inspection campaign reveals the need to thoroughly investigate the behaviour of critical elements such as dapped-end beams prestressed with post tensioned cables, whose brittle failure mechanism can lead to sudden collapse of the structure. The scientific literature was reviewed thoroughly, and a discussion and analysis of the numerical models that estimate the maximum load of dapped-end beams and the main experiments that were done was conducted. The focus of the analysis was on the details of the construction and the defects that were examined, as well as the testing methods that were used. Based on what was found on the literature, two experimental campaigns are designed: one in the laboratory and one in situ, with the aim of investigating the failure behaviour of post-tensioned dapped-end beams. The laboratory campaign involves six scaled specimens based on the design details of an existing bridge. The effect of different prestressing levels on the ultimate shear capacity will be evaluated using three-point non-symmetrical bending tests. The design of the

experimental tests is supported by an extensive numerical investigation using both simple Strut-and-Tie and solid finite element models. The design of the in situ experimental campaign on an existing bridge is presented, which will be conducted when the structure is demolished and rebuild. A 30-metre hinged drop-in span will be the subject of the tests and diagnostic investigations, and a three-point bending test will evaluate the capacity of the dapped-end beam in situ.

Abstract

La sicurezza dei ponte esistenti ha assunto negli anni un ruolo primario, specialmente dopo i recenti disastri che hanno coinvolto diverse opere sia nel territorio nazionale che internazionale. Per la valutazione e gestione del rischio dei ponte esistenti, l'Italia si è dotata di un nuovo approccio multi-livello basato sul rischio. Nella corretta valutazione del rischio, la valutazione della vulnerabilità e dei difetti dell'opera attraverso le ispezione visive assume un ruolo fondamentale all'interno del framework. I risultati di una estesa campagna di ispezioni visive, svolta nell'ambito del progetto di ricerca che ha coinvolto l'Università Politecnica delle Marche insieme a, il consorzio inter-universitario FABRE e all'ente gestore ANAS, sono vengono presentati in questo lavoro di tesi con l'obiettivo di evidenziare le maggiori criticità riscontrate sui ponti esistenti. Dalla campagna di indagini emerge la necessità di indagare approfonditamente il comportamento di elementi critici come le travi con selle Gerber post-tese, il cui meccanismo fragile di rottura può portare a collassi improvvisi dell'opera. Grazie ad un'accurata analisi della Attraverso lo studio della letteratura scientifica, sono stati approfonditi e analizzati studiati i modelli numerici proposti per valutare la capacità ultima delle travi con selle Gerber e le principali indagini sperimentali condotte, con particolare attenzione ai dettagli costruttivi e difettologici studiati e al metodo di prova impiegato. Sulla base di Partendo da quanto presente fatto in letteratura, sono state progettate due campagne sperimentali di indagine, una in laboratorio e un'altra in situ, sono progettate con il fine di indagare il comportamento a rottura delle selle Gerber post-tese. La campagna in laboratorio prevede la realizzazione di sei travi in scala con selle Gerber

progettate per riprodurre in scala ridotta le selle delle travi basate sugli elaborati di progetto di un ponte esistente. Il contributo di differenti livelli di precompressione sulla capacità ultima a taglio saranno valutati attraverso prove di flessione non-simmetrica su tre punti. Il progetto della campagna sperimentale è affiancato da un estesa indagine numerica sia con semplici modelli Strut-and-Tie sia con modelli agli elementi finiti solidi. Infine, viene è presentato il progetto della campagna sperimentale in situ su un ponte esistente che saranno condotte condotta in occasione della demolizione e sostituzione dell'opera. Le prove e le indagini diagnostiche saranno eseguite sulla campata tampone di 30 metri e mentre la capacità della sella Gerber sarà testata in situ attraverso mediante una prova di flessione su tre punti.

Contents

List of Figures

List of Tables

Introduction

Existing bridges and infrastructures risk classification and management have a primary role in national and international research. Recent disasters involving strategic structures have shaken the public and scientific opinion, and risk classification and safety assessment are becoming more and more urgent issues. The questions to be asked are: how accurately can we assess the safety of existing bridges? Can we predict their possible collapse?

The primary focus is mostly on structures characterized by statically determinate schemes and construction details that are, by design, vulnerable elements and were often employed in the past to build strategic constructions such as bridges. The majority of Italy's road network infrastructures were built after World War II and it is composed by a statically determinate bridges, such as the simple supported girders or continuous beams bridges. These structures achieve statically determinacy by adopting specific construction details as the half-joint connections.

Such bridges have a greater vulnerability than other structural types and require greater attention in the safety evaluation, especially regarding their fragile failure mechanisms that may develop very rapidly without early warning signs [1,2].

The after-war is, also, an historical period characterized by the development and use of the concrete tensioning system technology. The majority of patents registered for this technology dates back to the early 1900s, such as the Freyssinet patent from 1928, Dischinger's patent on external prestressing from 1933, and Morandi's patent in 1948, just to name a few.

This technology allows significant improvements of the concrete performance enabling the average span length in concrete bridges; however, it also hides some dangers, often underestimated in the past, foremost among them being corrosion, which is promoted by the presence of infiltration water and supported by carbonation phenomena. This can lead to compromise the health condition of high-tensile steel and its anchorages, causing local strength and tension losses in the girders critical sections, such as the midspan and supports.

In post-tensioned structures, the higher risk is connected to defects found in the injection grout inside the ducts. This defect is hardly detectable from the outside during visual inspection activities or even with appropriate non-destructive tests, i.e. tomography and georadar techniques. Hence, the presence of corrosion and missed duct injection may establish failure mechanisms or brittle structure collapse.

Several existing bridges show the above-mentioned critical aspects as they were designed by post-tensioned girders with half-joint connections [3]. In accordance with recent guidelines for risk classification and management, safety evaluation and existing bridges monitoring, these structures must be deeply investigated and safety assessed, with the help of special surveys that involve the use of non-destructive or semi-destructive tests.

The dapped-beam end safety evaluation, in particular on pre-stressed ones, is not easy, because it involves disturbed regions where the hypothesis on Eulero-Bernoulli classical beam theory breaks down. In literature the disturbed regions are treated with various approaches: from the simplest

methods of strut-and-tie to stress field models, up to nonlinear tridimensional models.

Several experimental studies were conducted on concrete corbels and dapped-end beams to evaluate their strength mechanisms and to investigate their ultimate capacity [4–21], yet only few of them involve prestressed elements [22–25]. Prestressing inside disturbed zones lead to tensions redistribution altering strength mechanisms and the element's ultimate capacity.

The aim of the thesis is to study the influence of prestressed levels on the strength mechanisms of a beam with dapped ends. This investigation is led by planning two experimental campaigns: one held in the Materials and Structures Official Testing Laboratory (LPMS) of the DICEA department at the Università Politecnica delle Marche and the other in situ on an existing bridge that will be demolished and replaced. In both cases, the experimental campaigns will be joined and supported by numerical analysis, adopting both strut-and-tie models and refined non-linear solid models. The laboratory experimentation involves the development of 5 prestressed specimens and 1 ordinary concrete specimen. Different levels of prestress will be applied to the 5 dapped-end beams, and two of the most common defects, such as the inadequacy of stirrups and corrosion, will be applied. The in-situ campaign involves the drop-in hinged span of a post-tensioned dapped-end box beam with an omega-shaped section and a total span length of 30 meters. The in-situ campaign will use the main diagnostic techniques provided by the new bridge guidelines [26,27] and new technical documents released by the interuniversity consortium FABRE [28,29] for conducting special investigations on post-tensioned prestressed bridges and dapped-beam ends.

The testing campaign is designed to identify the most useful and reliable techniques to be adopted in the case of post-tensioned cable bridges, to study the path of the cables, the state of preservation of the grout within the cables, and the assessment of residual stress on cables and concrete.

Chapter one of this thesis introduces the new bridge guidelines for risk assessment, management, safety evaluation and monitoring of existing bridges. Specifically, the multilevel approach will be described, focusing on level 2, which is related to the definition of the attention class of the structure.

Chapter two focuses on the project conducted in collaboration with the inter-university consortium FABRE and the national road management agency ANAS that applies the new bridge guidelines to define the class of attention on a selected sample of 1,000 bridges. The chapter presents the experience of visual inspections conducted on 43 bridges that showed the main defects and problems that can be found on existing bridges of different typologies. Special attention was paid to bridges with critical elements such as post-tensioning cables and dapped-end beams, as reported in the guidelines.

Chapter three discusses the state of the art on dapped-end beams, focusing on the strut-and-tie models developed to determine the ultimate capacity of dapped ends and on the experimental campaigns available in the literature highlighting the lack of tests investigating the prestress levels effects on the ultimate capacity of the elements.

Chapter four is focused on the design of the experimental campaigns and the numerical analysis performed to predict the tests results. In the first part, starting from the description of the design documents of an inspected bridge, the test design is described in all its phases: production, equipment and

specimens testing. In the second part, strut-and-tie and solid models, used to predict the failure behavior and to evaluate the ultimate capacity of the specimens, are presented. The research here presented initially foresaw also the execution of tests and the post-processing of results. Unfortunately, for delays due to specimen production (out of the control of the research group), it was not possible to execute the tests.

Chapter five presents a study of the feasibility and design of the experimental campaign to be carried out in situ on the existing bridge. In addition to the test design, an extensive survey campaign is proposed with the aim of investigating the main defects found during the ordinary visual inspection and of assessing the state of preservation of the structure, with an in-depth investigation on the post-tensioning system condition.

1 The new Italian guidelines for the risk assessment of bridges

The national technical code for construction [30], known in general as the NTC 2018, is the main regulatory framework for the design, construction and verification of buildings and infrastructures. The NTC 2018 provide some general criteria for the verification and intervention of existing structures, based on these main aspects:

- state of knowledge at the time of design and construction. focusing on possible deficiencies in design and execution
- knowledge of the actions acting on the structure, both ordinary and extraordinary, such as earthquakes, floods or landslides
- presence of degradation or significant changes from the original situation

The safety assessment must be carried out with numerical models that are constructed taking into account the level of knowledge of the structure, which depends on the documentation available and the quality and number of investigations carried out to determine the geometry, mechanical properties of materials and soils, and permanent loads. However, these principles and criteria are not specific or detailed enough for the existing bridges, which require a more tailored and comprehensive approach. As an example, the technical standards give indications on the number of investigations to be carried out on the structure in order to obtain a certain level of knowledge, but these indications are mostly based on existing buildings and not on

bridges. The safety factor that is applied in the numerical models, which depends on the level of knowledge achieved, has limited significance for the verification of existing bridges.

The Morandi bridge collapse was a tragic event that exposed the vulnerability of many existing bridges in Italy and represented a turning point in the Italian regulatory scenario. After the disaster, the Consiglio Superiore dei Lavori Pubblici (CSLP), the highest technical authority for public works in Italy, released new guidelines to complement and integrate the NTC 2018, by providing a more systematic and consistent methodology for the classification and risk management, safety evaluation and monitoring of existing bridges. The guidelines adopt a multilevel approach to address the problem of existing bridges, which begins with risk analysis and bridge classification at a regional scale and then proceeds to safety assessment and monitoring procedures. Additionally, it's a method that takes into account different kinds of risk that result from environmental factors and structural weaknesses. Specifically, the structural and foundation risks, the seismic risk and the landslide and hydraulic risks are all analyzed and assessed collectively. The aims of the new guidelines are to define common standards for the census, risk classification, safety verification and monitoring of existing bridges, which include both roadway and railway bridges with spans greater than 6 meters, and to obtain a single tool to be applied to all bridges in the country in order to establish a risk-based maintenance plans.

The guidelines approach is a multilevel framework based on 6 consequent levels of analysis, from level 0 to level 5, although the latter is not explicitly addressed within the guidelines. A graphic representation of the complexity

of the framework is shown by the Figure 1, extracted from the guidelines themselves.

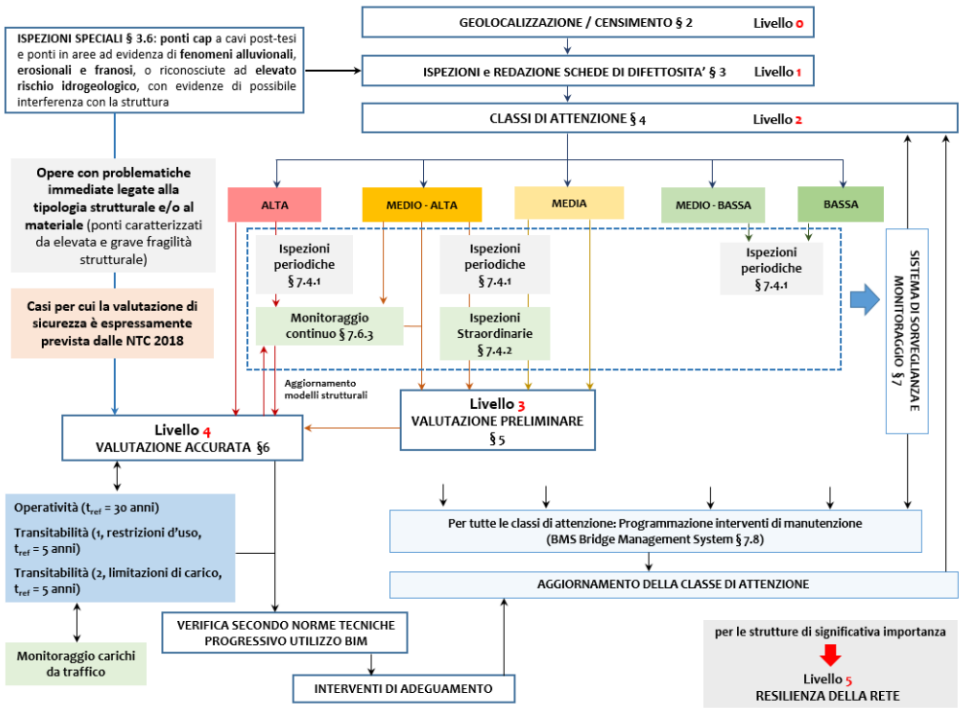

Figure 1. Multi-level framework for the risk classification and assessment of bridges from the new Italian guidelines [26].

The first step of the analysis is the Level 0 which is the knowledge level assessment of the investigated bridge. The purpose of this step is to collect the available data of the bridge, by consulting the original documents and design drawings, as well as other technical documents that are relevant for the bridge, to define characteristics, structural typology, construction materials, year of construction, geometric dimensions, etc. Moreover, at this stage the road networks are examined and data related to the volume and type of traffic and the availability, length, and feasibility of potential road

alternatives in case of any restrictions or closures on bridges are collected. The data gathered are standardized and summarized in a tabular form for uploading to the AINOP digital database (https://ainop.mit.gov.it/portale/), which aims to collect all the relevant information about the infrastructures in the national territory, including bridges.

Level 1 involves performing visual inspections on all catalogued bridges and are finalized to verify the reliability of the data collected in the census phase (level 0), with the possibility of gathering additional information about the geometric characteristics and site of construction and to verify the state of preservation of the structures. The objective condition of the structure is attested by an accurate photographic and geometric survey and by a survey of the main deterioration phenomena involving each structural element of both the superstructure and substructure, which must therefore be easily accessible, as in the case of box girders or hollow piers. Each structural element has a special inspection sheet to record the information on deterioration phenomena from visual inspections. The sheets depend on the element type and material, such as concrete pier or steel girder and they present a list of typical defects based on the technical literature and experimental applications on existing bridges. Each defect has a weight, G, that varies from 1 to 5 according to a severity scale. The defect extent and intensity parameters, k_1 and k_2, are evaluated based on the defect manual and can be 0.2, 0.5 or 1. In case of highly severe defects ($G=4$ or $G=5$), it is also possible to report if the global stability of the structure is compromise by checking a specific box. For each defect, boxes indicate the number of photos and any remarks, and if the defect is absent due to being not applicable, not detectable, or not present. All bridges must have appropriate inspection

description sheets that compile the census information (level 0) and the visual inspection information. A special sheet for landslide and hydraulic hazard must be completed during the visual inspection to identify the bridge's hazard, vulnerability, and exposure to these phenomena.

At level 1, it is essential to identify critical elements that are prone to degradation and may affect the structure's stability. The critical elements depend on the bridge type and the attention class being evaluated. For structural and foundational risk, they are dapped-beam ends, prestressing cables, extensive and intense cracking scenarios, loss-of-support mechanisms, ongoing kinematics and scouring of foundations. For seismic attention class, they are highly degraded bearings, substructures with significant defectiveness, loss-of-support mechanisms and ongoing kinematics. The guidelines in section 3.6 introduce mandatory 'special inspections' , which consist of an in-depth investigation of the structural status with semi-destructive and non-destructive tests to verify the need for accurate safety checks, for major defects on critical elements, post-tensioned concrete bridges with injected cables, or bridges in areas subjected to flooding or landslide phenomena. Post-tensioned concrete bridges with injected cables built in the 1960s/70s and those with intense damage should have priority for special tests; the corrosion of prestressing cables reduces the structure's strength and can cause sudden collapses without traffic or added loads. It also decreases the prestressing force in critical sections with high shear and bending stresses, causing extend crack damages and permanent displacements. According to American *guidelines for Sampling, Assessing, and Restoring Defective Grouts in Prestressed Concrete Bridge Post-*

Tensioning Ducts[31], special inspections conducted on prestressing cables have these main purposes:

i. **Identification of cable path and location of defects**
   The reconstruction of the cable path starts with the analysis of the design documentation recovered during Level 0. If the documentation is insufficient or totally absent, nondestructive investigations, such as pacometric tests, georadar surveys, ultrasonic tomography, or impact-echo techniques, must be performed to locate the cable path. The latter, along with magnetic (such as the Magnet Flux Leakage or MFL) and electrochemical (like the half-cell potential measurement) methods, are also useful in determining the presence of any voids or cracks within the sheathing and possible corrosion of the cables

ii. **Experimental campaign to assess the intensity of element defects**
   Defects found during nondestructive testing should be investigated by semi-destructive tests such as endoscopic surveys and vacuometric tests to verify the real presence of defects in the injection mortars and corrosion of the cables. Where necessary, the concrete cover may be removed and the metal sheathing cut to inspect the cables, and mortar samples taken for chemical tests to determine the presence of moisture and chlorides. Hardness and tension release tests can be conducted on prestressing cables to estimate the material resistance and the residual level of prestressing

Regular inspections must be carried out with a minimum frequency that depends directly on the Class of Attention (CoA). The minimum frequency is

different for type 1 bridges, which have already been subject to ordinary inspections, and for newly built bridges, type 2, which have not yet been subject to visual inspections. For works that have already been inspected, the minimum frequency ranges from every two years for the Low attention class to every six months for the Medium-High and High attention classes; in addition, a monitoring system is to be installed for these structures. The Type 2 structures have a minimum inspection frequency that is half of that of the Type 1 works that have already been supervised; the minimum frequency varies from once a year for the Low attention class to once every three months for the Medium-High and High attention classes. The minimum frequencies of routine inspections were summarized in Table 1.

Table 1. Minimum frequency of regular inspections.

CoA	Low	Medium-Low	Medium	Medium-High	High
Minimum frequency (Type 1)	2 years	18 Months	1 year	Based on monitoring system or 6 Months	Based on monitoring system or 6 Months
Minimum frequency (Type 2)	1 year	9 Months	6 Months	Based on monitoring system or 3 Months	Based on monitoring system or 3 Months

Special inspections must be carried out within 5 years of the previous inspection for bridges with Low and Medium-Low Attention Classes, and within 2 years otherwise. If the attention class is found to have worsened, special inspections must be conducted within 60 days.

Level 2 is dedicated to the evaluation of the attention class of the structure for the individual risk factors to which the structure is subject: structural and foundational risk, seismic risk, landslide and hydraulic risks. Following the determination of the individual attention classes, it is then possible, by means of logical operators, to arrive at the definition of the overall attention class of the structure. For each of the CoA determination procedures, a qualitative risk evaluation is carried out accounting for three parameters: hazard, vulnerability, and exposure. For the purpose of this thesis, we will focus on the determination of structural/foundational and seismic attention classes only.

Focusing the attention on the structural and foundational risk, hazard depends on traffic loads in terms Average Daily Traffic (ADT) of heavy vehicles passing over a single lane of the bridge and permissible maximum weights. The frequency of heavy vehicle passages is defined as High for ADT $\geq$ 700, Medium for values between 300 and 700 and Low for values below or equal 300. The maximum permissible load on the structure defines the class of the bridge from Class A to Class E, where Class A corresponds to permissible loads according to NTC18 and Class E corresponds to permissible maximum weights of 3.5 ton, whereas B, C and D correspond to intermediate values (44 ton – 26 ton and 8 ton). The combination with logical operators of the two parameters gives the structural and foundational hazard, as show in Figure 2. It is worth emphasizing that for Class A bridges, i.e., where no specific load limitation is applied, the hazard is Medium-High or High, namely for bridges with High or Medium-High frequency of heavy vehicle passages.

Class A (permissible maximum weights from NTC18)	**Average Daily Traffic of heavy vehicles**		
	High	Medium	Low
	High	**High**	**Medium-High**
Class B (permissible maximum weights 44 ton)	**Average Daily Traffic of heavy vehicles**		
	High	Medium	Low
	High	**Medium-High**	**Medium**
Class C (permissible maximum weights 26 ton)	**Average Daily Traffic of heavy vehicles**		
	High	Medium	Low
	Medium-High	**Medium**	**Medium-Low**
Class D (permissible maximum weights 8 ton)	**Average Daily Traffic of heavy vehicles**		
	High	Medium	Low
	Medium	**Medium-Low**	**Low**
Class E (permissible maximum weights 3.5 ton)	**Low**		

Figure 2. Hazard class as a function of the maximum permissible weights and the daily traffic frequency of heavy vehicles on a single lane.

Structural/foundational vulnerability depends on main parameters such as, the level of defect, structural scheme, maximum span length, material and number of spans, and secondary parameters such as the speed of degradation evolution and the design standards adopted. The level of defects is classified into 5 intensity levels:

- **High**: Highly severe defects (*G=4* or *G=5*) of any intensity, which involve critical elements or presence of critical conditions for the structural stability

- **Medium-High**: Highly severe defects (*G=4* or *G=5*) with high intensity (k_2), which involve essential elements for the global stability.
- **Medium**: Highly severe defects (*G=4* or *G=5*) with high intensity (k_2), which does not involve essential elements for the global stability.
- **Medium-Low**: Medium-High defects (*G=4*) with Medium-Low intensity (k_2) and Medium and Low defects (*G=3, G=2, G=1*) with any intensity (k_2) on numerous elements.
- **Low**: Medium and Low defects (*G=3, G=2, G=1*) with any intensity (k_2) on a few elements.

To evaluate how fast the degradation evolves, the bridge's construction period is considered; indeed, if a young bridge has heavy degradation, it means that the degradation rate is high. The design code age indicates the design loads that affect the bridge's structural capacity. The vulnerability of structures is related to the structural scheme, length of spans and by the material of construction; specifically, parameters like, the number of degrees of freedom, the susceptibility to fragile failures, such as in dapped-end beams or corbels, and materials sensitive to degradation phenomena, must be considered in the overall vulnerability of the structure (Figure 3). If the bridge has more than 3 spans, the vulnerability associated with the structural type must be increased by one level.

The vulnerability class is determined by following a logical path that starts from the damage level (obtained from on-site inspections) and that combines,

sequentially, the speed of the damage evolution, the design code age, and the combination of structural typology, construction materials and the maximum span length, L, expressed in meters (Figure 4).

Structural Scheme	Material	L ≤ 5 m	5 m < L < 15 m	15 m ≤ L < 25 m	L ≥ 25 m
Supported beams	RC	Medium-Low	Medium	Medium-High	High
	Prestressed RC	Medium-Low	Medium	Medium	Medium-High
	Steel	Low	Medium-Low	Medium	Medium-High
	Iron	Medium-Low	Medium	Medium-High	High
	Wood	Medium	Medium-High	High	High
	Composite	Medium-Low	Medium	Medium-High	High
Continuos beams / Frame	RC	Low	Medium-Low	Medium	Medium-High
	Prestressed RC	Low	Medium-Low	Medium	Medium
	Steel	Low	Low	Medium-Low	Medium
	Iron	Low	Medium-Low	Medium	Medium-High
	Composite	Low	Medium-Low	Medium	Medium-High
Arch	Masonry	Low	Medium-Low	Medium-Low	Medium
	RC	Low	Medium-Low	Medium	Medium
Deck arch	RC	Medium-Low	Medium	Medium	Medium-High
Dapped-end beams / Half-joint connections	RC	Medium-High	High	High	High
	Prestressed RC	Medium-High	Medium-High	Medium-High	High
	Steel	Medium	Medium-High	Medium-High	High
	Iron	Medium-High	Medium-High	High	High
	Composite	Medium-High	High	High	High
Supported slab	RC	Medium-Low	Medium	Medium-High	High
Fixed slab	RC	Low	Medium-Low	Medium	Medium-High

Figure 3. Vulnerability class as a function of static scheme, maximum length of spans, and material.

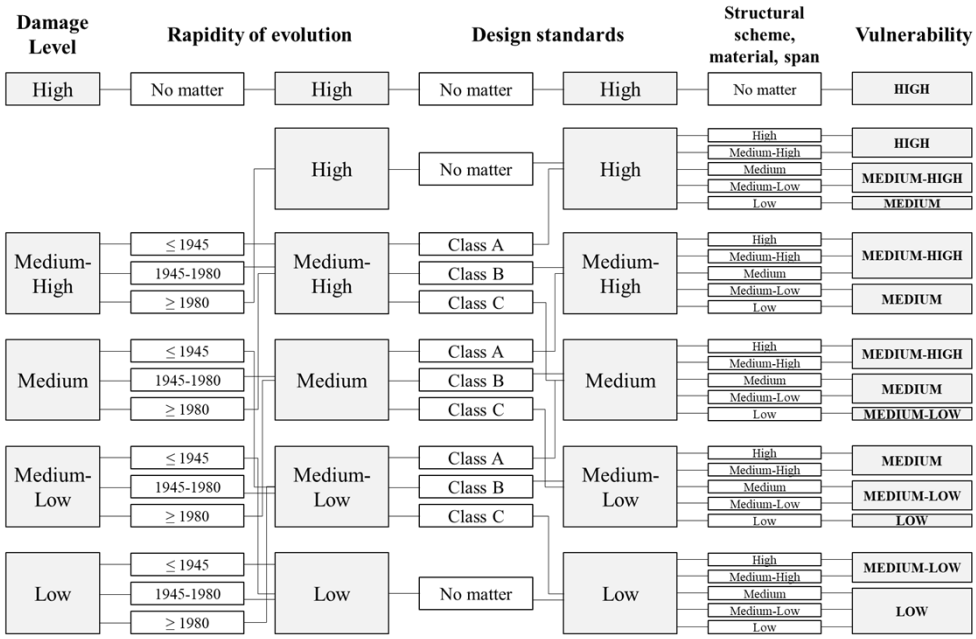

Figure 4. Vulnerability class of the structural and foundation Class of Attention.

The exposure level of the bridge depends on traffic parameters and the type of previously described entities. Thus, the main parameters considered are the average daily traffic related to the entire roadway and the average length of the spans; The level of exposure due to the daily traffic is rated with three levels: High (ADT ≥ 25000 vehicles/day), Medium (10000 vehicles/day < ADT < 25000 vehicles/day), and Low (ADT ≤ 10000 vehicles/day) and is combined with the average span length as shown in Figure 5. The final level of exposure also takes into account the presence or absence of alternative roads and the type of overridden entity; in the absence of alternative road, the exposure class is increased by one level, while the type of previously described entity takes into account the presence of crowding below the structure: High level for bridges placed above main roads or railways,

Medium level in case of secondary roads or rivers and lakes, and Low level in case of natural discontinuities characterized by sporadic presence of people. The logical paths leading to the definition of the exposure class are shown in Figure 6.

	Level of ADT		
Average span length	High	Medium	Low
L ≥ 50 m	High	Medium-High	Medium
20 m < L < 50 m	Medium-High	Medium	Medium-Low
L ≤ 20 m	Medium	Medium-Low	Low

Figure 5. Level of Average Daily Traffic and average span length.

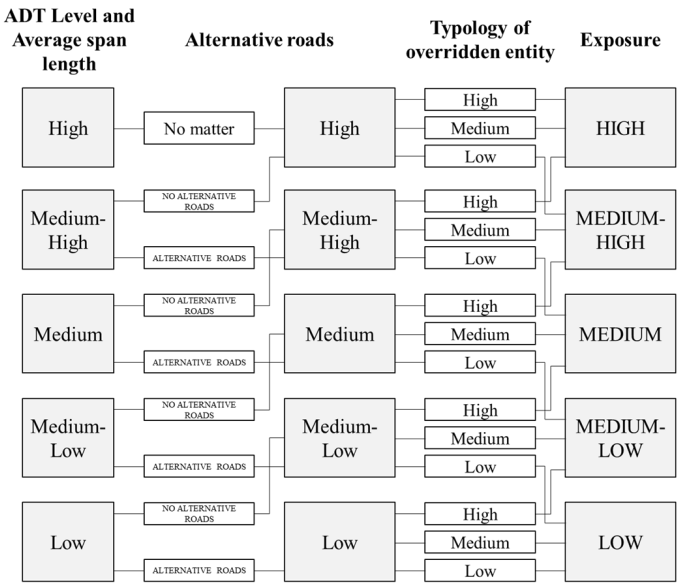

Figure 6. Exposure class of the structural and foundation Class of Attention.

The structural and foundation class of attention can be calculated by combining the three hazard, vulnerability and exposure classes with the following logical paths (Figure 7).

Hazard High		**Exposure**				
		High	Medium-High	Medium	Medium-Low	Low
Vulnerability	High	High				
	Medium-High	High		Medium-High		
	Medium	High	Medium-High		Medium	
	Medium-Low	Medium-High	Medium			
	Low	Medium-High	Medium		Medium-Low	

Hazard Medium-High		**Exposure**				
		High	Medium-High	Medium	Medium-Low	Low
Vulnerability	High	High				
	Medium-High	High	Medium-High			Medium
	Medium	Medium-High		Medium		
	Medium-Low	Medium			Medium-Low	
	Low	Medium		Medium-Low		Low

Hazard Medium		**Exposure**				
		High	Medium-High	Medium	Medium-Low	Low
Vulnerability	High	High				
	Medium-High	Medium-High			Medium	
	Medium	Medium-High	Medium			
	Medium-Low	Medium			Medium-Low	
	Low	Medium		Medium-Low	Low	

Hazard Medium-Low		**Exposure**				
		High	Medium-High	Medium	Medium-Low	Low
Vulnerability	High	High				
	Medium-High	Medium-High		Medium		
	Medium	Medium-High	Medium		Medium-Low	
	Medium-Low	Medium		Medium-Low		Low
	Low	Medium	Medium-Low		Low	

Hazard Low		**Exposure**				
		High	Medium-High	Medium	Medium-Low	Low
Vulnerability	High	High				
	Medium-High	Medium-High	Medium			Medium-Low
	Medium	Medium			Medium-Low	Low
	Medium-Low	Medium		Medium-Low	Low	
	Low	Medium-Low	Low			

Figure 7. Structural/foundation Class of Attention.

The seismic attention class considers the main response parameters of bridges and road networks to seismic actions, and it depends on hazard, vulnerability, and exposure factors. The seismic hazard of the site depends on the Peak Ground Acceleration (PGA), the topographic category of the site, and the subsoil category. The PGA, evaluated for a probability of exceedance of 10% in 50 years and referred to the bedrock action, i.e. a Category A subsoil for the Italian technical code [30], is related to four topographic categories, from flat terrain profiles with maximum slope value of 15 degrees (T1) to slopes of 30 degrees (T4), as shown in Figure 8.

	T1,T2,T3	**T4**
$a_g \geq 0.25$ g	High	High
$0.15 \text{ g} \leq a_g < 0.25$ g	Medium-High	High
$0.10 \text{ g} \leq a_g < 0.15$ g	Medium	Medium-High
$0.05 \text{ g} \leq a_g < 0.10$ g	Medium-Low	Medium
$a_g < 0.05$ g	Low	Medium-Low

Figure 8. Seismic hazard classification based on the Peak Ground Acceleration and topographic categories.

The overall seismic hazard class is assessed by combining the hazard class calculated as a function of the two parameters PGA and topographic category and the subsoil category (A – B – C – D – E), which is based on the shear velocity averaged on the first 30 meters ($V_{s,30} > 800$ m/s, $360 \text{ m/s} < V_{s,30} \leq 800$ m/s, $180 \text{ m/s} < V_{s,30} \leq 360$ m/s, $100 \text{ m/s} < V_{s,30} \leq 180$ m/s, $V_{s,30} \leq 100$ m/s). The logical paths leading to the definition of seismic hazard are shown in Figure 9.

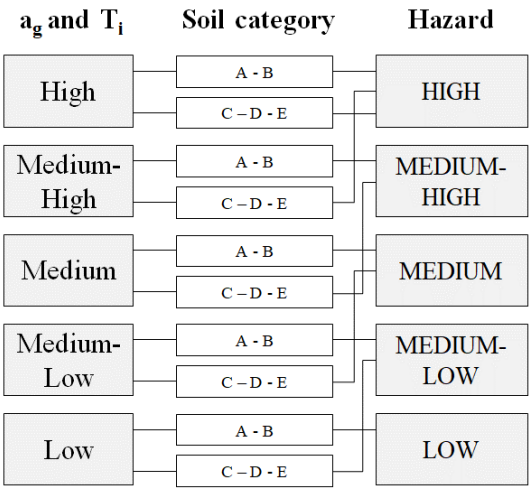

Figure 9. Hazard class of the seismic Class of Attention.

The seismic vulnerability of bridges depends on several factors, first and foremost the static scheme. In particular, parameters such as the number of degrees of freedom, the number of structural elements vulnerable to seismic actions, the mass of the structure and the state of preservation play a primary role in the assessment of seismic vulnerability. The first vulnerability classification is then made by combining: the static scheme and maximum span length, the material and number of spans (Figure 10).

In the presence of unfavourable conditions against seismic action, such as, for example, bridges with skewed or curved decks, single-column piers or with very uneven heights, significantly degraded bearings, the vulnerability based on the static scheme, maximum span length and material could be increased by one level.

		Statically determinate		Statically indeterminate	
		L ≤ 20 m	L ≥ 20 m	L ≤ 20 m	L ≥ 20 m
RC	Single -span	Medium	Medium -High	Low	Medium -Low
	Multi -span	Medium -High	High	Medium -Low	Medium
Prestressed RC	Single -span	Medium	Medium -High	-	-
	Multi -span	Medium -High	High	Medium -Low	Medium
Masonry	Single -span	-	-	Low	Medium -Low
	Multi -span	-	-	Medium -Low	Medium
Steel	Single -span	Medium -Low	Medium -Low	Low	Low
	Multi -span	Medium	Medium	Medium -Low	Medium -Low

Figure 10. Seismic vulnerability class as a function of static scheme, maximum length of spans, number of spans and material.

Additional parameters affecting the seismic vulnerability of the structures are related to the design criteria, which can be defined as seismic or non-seismic depending on the year and design standard adopted and the level of damages. The latter is assessed based on visual inspections conducted at Level 1 and is based on the judgment criteria adopted for structural and foundational damage level assessment, focusing on any defects in critical sections such as supports and pier ends or critical conditions such as ongoing kinematics or loss of support. The vulnerability class is determined by following a logical path that starts from the vulnerability associated with the structural scheme, the number of spans and material, and ends with the design criteria and damage level (obtained from on-site inspections), as shown in Figure 11.

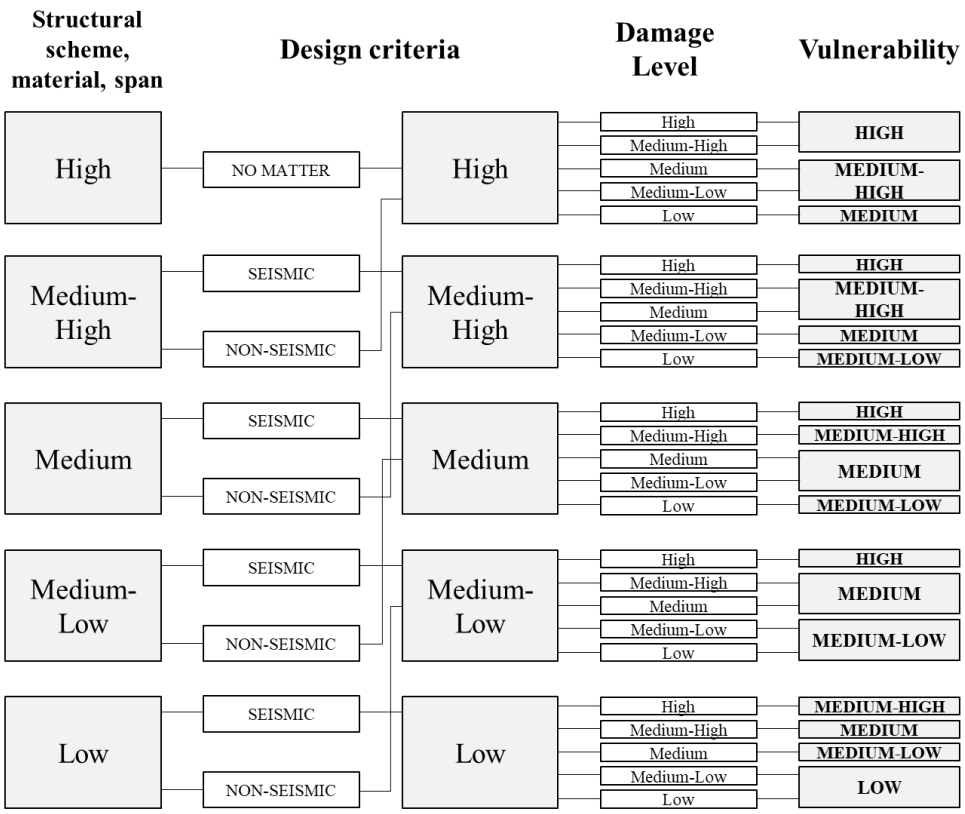

Figure 11. Vulnerability class of seismic class of attention.

The assessment of seismic exposure class starts from the exposure level related to the structural foundation attention class; specifically, the latter is increased if the bridge is defined as strategic in case of emergencies, or remains unchanged for non-strategic bridges (Figure 12).

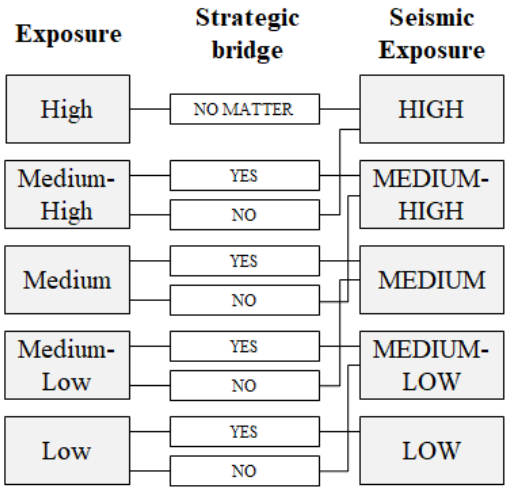

Figure 12. Seismic exposure class of seismic attention class.

The seismic attention class can be calculated by combining seismic hazard, seismic vulnerability and seismic exposure by adopting the same logical paths presented for structural and foundational attention class.

Similar to what has been seen for the determination of the structural/foundational and seismic attention class, it is possible to determine the hydraulic and landslide attention class. Once the separate evaluation of each attention class is completed, a multi-hazard analysis can be carried out by combining the various attention classes with logical operators and obtaining the overall attention class of the bridge (Figure 13). In the multi-hazard analysis, greater weight is given to the structural/foundational attention class since it is the one related to the normal operating conditions of the bridge.

High CoA Structural/foundations		**Hydraulic and landslides CoA**				
		High	Medium-High	Medium	Medium-Low	Low
Seismic CoA	High	High				
	Medium-High	High				
	Medium	High				
	Medium-Low	High				
	Low	High				

Medium-High CoA Structural/foundations		**Hydraulic and landslides CoA**				
		High	Medium-High	Medium	Medium-Low	Low
Seismic CoA	High	High		Medium-High		
	Medium-High	High	Medium-High			Medium
	Medium	Medium-High			Medium	
	Medium-Low	Medium-High		Medium		
	Low	Medium-High	Medium			

Medium CoA Structural/foundations		**Hydraulic and landslides CoA**				
		High	Medium-High	Medium	Medium-Low	Low
Seismic CoA	High	High	Medium-High		Medium	
	Medium-High	Medium-High		Medium		
	Medium	Medium-High	Medium			
	Medium-Low	Medium				Medium-Low
	Low	Medium			Medium-Low	

Medium-Low CoA Structural/foundations		**Hydraulic and landslides CoA**				
		High	Medium-High	Medium	Medium-Low	Low
Seismic CoA	High	Medium-High	Medium			
	Medium-High	Medium				Medium-Low
	Medium	Medium			Medium-Low	
	Medium-Low	Medium		Medium-Low		
	Low	Medium	Medium-Low			

Low CoA Structural/foundations		**Hydraulic and landslides CoA**				
		High	Medium-High	Medium	Medium-Low	Low
Seismic CoA	High	Medium			Medium-Low	
	Medium-High	Medium		Medium-Low		
	Medium	Medium	Medium-Low			
	Medium-Low	Medium-Low				Low
	Low	Medium-Low	Low			

Figure 13. Muti-risk combinations for the determination of the overall Class of Attention.

The guideline [26] provides different approaches depending on the overall Class of Attention (CoA) of the structure:

- **Low** or **Medium-Low CoA**

  The multi-hazard analysis shows no significant criticality for the bridge. In this case, only periodic inspections are required, with a minimum frequency that varies according to the CoA value, as shown in Table 1.

- **Medium CoA**

  In this case, besides the mandatory visual inspections, extraordinary inspections are also planned to investigate any criticality found during the multi-hazard analysis. For these works, it is compulsory to perform the simplified verifications at Level 3 to quickly assess the safety of the work. If the verification fails, the in-depth safety verifications must be carried out.

- **Medium-High CoA**

  The periodic and extraordinary inspections and the safety assessment of Level 3 are mandatory as for bridges with Medium CoA. In addition, it is obligatory to design and install a continuous structural health monitoring (SHM) system.

- **High CoA**

  Periodic inspections and installation of a continuous monitoring system of the major critical issues are required. For these bridges, an accurate Level 4 safety assessment is necessary.

The aim of the preliminary security assessment at Level 3 is to examine the issues found during Level 1 visual inspections more closely and to determine their potential causes. The assessment compares the demand on each structural element from the design loads and the demand from the current technical standards traffic loads. The ratio of these two demands gives a meaningful value of the structure's capacity, which indicates whether Level 4 accurate verifications are necessary or not.

Level 4 involves the accurate assessment of the safety of the structure, which must be conducted according to technical standards. The knowledge of the bridge assumes a fundamental role in safety verification; indeed, the geometry of the structural elements and their reinforcements, the evaluation of degradation phenomena and the confidence factors to be attributed to the loads acting on the structure and the mechanical characteristics of the materials depend on it. The safety verification must be carried out taking into account the following factors:

- The return time, T_{ref}, which represents the time span assumed during the analyses; in that time span, the safety verification is guaranteed.
- The damage conditions, which must be included in the analysis if they lead to a reduction in the capacity of the structure
- The traffic loads, which are those of the current technical standards, acting on the structure.

The safety verifications follow the limit states approach and use partial safety factors, according to the current standards [30]. Depending on the results, the bridge can be classified into one of these three categories:

- **Adequate bridge**: The bridge meets the current Italian technical code requirements. The bridge can be used normally without any interruptions or traffic restrictions.

- **Operative bridge**: The bridge meets the code requirements with reduced safety factors on loads and material strengths by using a lower return period equal to 30 years(T_{ref} = 30 years). The bridge can be used for the next 30 years, but the verifications need to be repeated after that.

- **Transitable bridge**: The bridge meets the code requirements only for a short time period (5 years). The bridge can be used with some load or traffic limitations for 5 years, but it needs to be restored, upgraded, or rebuilt after that.

Level 5 is not covered in the current version of the guidelines, but it will focus on conducting refined analyses of relevant works within the road network. The analyses will enable the evaluation of the road segment's resilience and the work's importance in terms of transport, as well as the assessment of the potential social and economic consequences of a possible interruption of the structure.

2 Main defects from visual inspections and critical elements of a bridge stock

As part of a major research project commissioned by the Ministry of Transport, the FABRE inter-university research consortium and the national road management agency (ANAS) studied the applicability of new guidelines for defining the overall class of attention, from census level 0 to level 2, on a sample of about 1,000 bridges distributed throughout the country. In the second phase, about 300 bridges that showed the most critical issues will be selected, and level 4 safety verifications will be conducted. The research unit of Marche Polytechnic University contributed to the project by applying the guidelines to a sample of 43 bridges shown in Figure 14, distributed in 5 different Italian regions:

- **Marche (20/43)**: the 20 assigned bridges of Marche region are divided into 18 prestressed concrete bridges and 2 reinforced concrete bridges. The prestressed concrete bridges are mostly supported girder bridges or, in 3 cases, continuous girders with drop-in hinged segment, while the two reinforced concrete bridges have, respectively, arch and frame structural schemes

- **Emilia Romagna (12/43)**: the samples from the Emilia Romagna region consist of 11 prestressed concrete bridges with simply supported beams and 1 curved masonry arch bridge

- **Sardegna (5/43)**: the samples from the Sardegna region consist of 3 prestressed concrete bridges with simply supported beams, 1 reinforced concrete frame bridge, and 1 continuous truss bridge

- **Calabria (7/43)**: the samples from the Calabria region consist of 2 prestressed concrete simply supported girder bridges, 1 bridge consisting of both prestressed concrete supported girder spans and continuous spans with reinforced concrete Gerber's scheme, 3 reinforced concrete supported girder bridges, and 1 masonry arch bridge

Figure 14. Distribution of the bridges on the Italian territory (ANAS-FABRE Project).

According to the Italian bridge guidelines, 23 out of 43 bridges are characterized by critical elements and require special inspection, in addition to ordinary visual inspection, to thoroughly investigate the state of

preservation of the critical elements. The 21 bridges belong to the category of prestressed concrete bridges and are made with the post-tensioning system. Therefore, the prestressing cables that are injected inside the metal ducts or the tensioning anchors are critical due to the possibility of defects.. For 7 of these bridges, in addition to the criticality related to the prestressing system, there is also the criticality related to the dapped-beam ends. The remaining two bridges are ordinary concrete bridges with the continuous Gerber's structural scheme and dapped-end beams.

Inspection activities were conducted during a two-year period and revealed a wide range of issues that can be observed on existing bridges, such as humidity, water infiltrations, materials decay, presence of cracks, juts to name a few. The inspection campaign was conducted according to new guidelines and it allowed to collect useful information to determine the state of conservation and to evaluate the attention class of the bridges; specific inspection sheets were prepared and a report containing a detailed recording of the defects of each structural element. On inspected bridges, possible causes of the defects were investigated as well as possible consequences on their stability and safety.

Particularly, structures affected by the presence of critical elements or situations such as ongoing kinematics or landslide and rockfall phenomena, required a deeper study given the criticalities of the bridges with regards to their stability.

With the aim to identify the main issues of existing bridges, level 2 evaluations of each bridge were evaluated and principal defects, encountered for each main bridge category, were studied. For each category, an overview

of main defects found is reported below, focusing the attention of possible causing mechanisms and the effects that such defects produce on the bridge stability.

Masonry arch bridges

Among the set of inspected bridges, there are two masonry arch bridges, characterized by a straight and curved path, respectively. Both bridges show minor defects such as presence of active and passive humidity and water traces coming from road pavement or from the road embankments at the abutments (Figure 15).

Figure 15. Photos of the two masonry arch bridges.

In one of these bridges, major defects are connected to materials decay that concerned both arch bricks and abutments and the concrete of the upper slab, particularly its material shelves.

The material decay of the arch and abutments involve bricks and cement mortar causing loss of sections and, in some spots, failure of a significant number of bricks, as shown in the left picture of Figure 16. The concrete cantilevered beams of the slab show and intense degradation of the material:

the cover spalling has exposed the reinforcement that appear corroded (right picture of Figure 16).

Figure 16. Material degradation on the arch (left) and cover spalling and reinforcement corrosion on the concrete slab (right).

An ongoing mechanism that is causing a portion of the masonry to overturn out of plane was detected in the second curved masonry arch bridge.. The out of plan failure mechanism, is visible from the road pavement, where it is possible to notice a deformation of accessory elements and pavement (Figure 17), and by inspecting both the arch and the abutments, where there are wide cracks along the masonry texture (Figure 18).

Figure 17. Out of plane failure mechanisem of the curved masonry arch bridge.

Figure 18. Cracks along the masonry texture on abutments and concrete arch.

Steel composite bridge

A sample of the set consists of a bridge made with 2 truss beams in Corten steel connected to each other through upper and lower horizontal crossbeams

(Figure 19). The deck is closed on the top by a reinforced concrete slab connected through Nelson studs. The structural scheme is that of a continuous beam on multiple supports.

Figure 19. Panoramic photo of the steel composite bridge.

On the bridge were not reported high severity defects, however, minor defects were reported such as presence of weather water, impact damages on the beams, presumably caused during the construction phases, and corrosion phenomena promoted by marine aerosol due to the proximity of the bridge to the sea and particular geomorphological conformation of the area. The water traces are visible mainly on abutments and slabs where the water can infiltrate through pavement joints or through damaged draining ducts, as it can be seen from the pictures taken from the photographic database of the inspection (Figure 20). Corten steel beams are excessively oxidized, especially along the side exposed to marine winds and they show impact damages in several points caused during the construction phases of the bridge (Figure 21). More minor effects are encountered on the piles such as small honeycombs or shrinkage cracking (Figure 22). Overall, the bridge is in a good state of conservation.

Figure 20. Water infiltrations on the concrete slab (left) and on the abutment (right).

Figure 21. Steel corrosion of the Corten steel (left) and impact damages on beams (right).

Figure 22. Concrete honeycombs on pier (left) and shrinkage cracks on concrete cap (right),

Reinforced concrete bridges without critical elements

In the set of bridges, there are 4 concrete bridges with different structural schemes that do not show critical elements: 1 frame bridge, 2 simply supported beam bridges, 1 arch bridge and 2 bridge with supported and arch beams.

The frame bridge is composed of two spans of 17 m width with a 1 m high slab cast in place (Figure 23).

Figure 23. Photo of the concrete frame bridge.

From a general point of view, the structure is in a mediocre state of conservation compatible with the age of construction of the structure and it doesn't show concerning degradation for the global stability. Although intense localized defects are present, the fundamental structural elements are still able to carry the loads overall. Extended cover spalling was identified which affected the shear stirrups and the reinforcements of the slab. The exposed reinforcements are completely oxidized and corroded (Figure 24). The bridge crosses a canal and the presence of water caused a capillary rise

of humidity and washing away of the concrete on piers and abutments. The level of defectiveness of the bridge, despite the presence of high severity defects such as reinforcements corrosion, was classified as Medium-Low.

Figure 24. Covert spalling and reinforcement corrosion.

Multi-span bridges with supported beams are made with concrete beams cast in place both with variable and constant section heights. On these bridges were found important defects that concerned critical sections such as the mid-span section or the supporting section of the beams. The majority of the defects is caused by concrete decay due to the presence of water in the road pavement and to exceptional flood events of the rivers. The reinforcements are very corroded, as it is shown in the pictures taken during the inspections, and some points, such as to cause the breakage of the shear stirrups (Figure 25).

Figure 25. Reinforcement corrosion and stirrups failure in the mid-span section of RC beam.

The reinforcement corrosion and cover spalling on the beams concerned sections critical to structural stability such as supporting sections and mid-span sections of the beams where the bending moment is maximum (Figure 26).

Figure 26. Corrosion and stirrup failure on the support section (upper) and on mid-span section (lower)

The piers were, also, affected by corrosion phenomena and concrete cover detachment causing the failure of several shear stirrups in areas where, in the event of seismic activities, the shear stress is maximum and thus exposing the elements to brittle and non-ductile failures (Figure 27).

Figure 27. Concrete cover detachment and stirrup failures on concrete pier.

The beams show signs of the shear-resistant mechanism of the Ritter's and Mörsch's truss model. On the concrete beams were, also, found 45 degrees inclined cracks in the support areas that extend from the lower edge to the upper one of the beam and are repeated with constant spacing along the beam development. On almost all the beams, with an accurate inspection, it is possible to detect several diagonal cracks on the support zones as shown in Figure 28.

Figure 28. Diagonal cracks on the support zones of the RC beams.

The multi-span arch bridge has 4 semicircular arches with a radius of 5.5 m and 1 arch of 5.8 m that overpasses the river. The bridge has an exterior stone facing on the piers and abutments (Figure 29).

Figure 29. Photo of the concrete arch bridge.

Major defects are localized on the concrete arches that show extended transversal cracks of medium intensity, but not so much to undermine the static of the bridge (Figure 30); in addition, on these elements are present wide humidity stains and material degradation connected to the water presence. Additional defects are encountered on the lateral curbs of the concrete slab; on these elements, the concrete cover detachments and oxidized and corroded reinforcements, are present.

Figure 30. Transversal cracks on concrete arches (upper) and concrete degradation and humidity (lower).

The concrete bridge with variable cross-sections are two: one with arched beams consists of 4 spans of beams placed on girders piers and a central span composed of two arched beams of variable section and the other with 4 simply supported beams (Figure 31).

Figure 31. Concrete bridges with variable beam cross-sections.

On the beams, two types of vertical cracks were found: some related to corrosion of the underlying stirrup reinforcements which is causing the ejection of the concrete cover (Figure 32) and others related to the cracking due to the bending moment acting on the beams, as shown in Figure 33 (cracks that tend to tilt as one gradually moves away from the mid-span cross-section).

Figure 32. Vertical cracks in correspondence of the stirrups.

Figure 33. Bending cracks of the external concrete beam near to the support.

The bridge, also, shows very pronounced defects related to humidity and water presence that can infiltrate through the road pavement and the concrete slab causing wide portions of degraded concrete. On vast portions of the slab, it is possible to notice active and passive humidity stains in the form of white calcium carbonate efflorescences. In some cases, white efflorescences turn to orange suggesting iron oxides presence coming from the reinforcements. The intensity of this phenomenon is such that it is possible to notice stalactites and flowstone formations on the beams and slabs (Figure 34); the origin of the phenomenon is, presumably, due to the intense use of road salts on the pavement.

Figure 34. Efflorescences and stalactites on concrete slabs.

Prestressed RC bridges

Prestressed bridges with pre-tensioned beams consist of beams, usually I-shape, V-shape, or Omega-shape cross-section, with prestressing cables stretched before the concrete pouring phase: when the concrete is ready, the cables are cut and the prestressing force is transmitted to the beam. In the set of analyzed bridges, about 1/3 are representative of this structural type (Figure 35).

Figure 35. Some photos of the Prestressed RC bridges from the set.

In general, precast beams may be recognized by analyzing the beams ends and by noting the absence of the concrete pad typical of the post-tensioned type; sometimes, it is possible to notice, on the sole of the beam bulb, the presence of the metal diverters used to divert the path of the cables within the beam.

Therefore, the beams are built in a facility and installed on the bridge through lifting. The slab, for all inspected bridges types, is made in concrete and it can be of two kinds: with predalles or cast in place. Piers, depending on the roadway width, may have 2-core or multi-core box section or full sections. The bearing devices, that are commonly found, are metal hinge or carriage devices, reinforced rubber bearings or newer seismic isolators.

The concrete slabs often show defects related to water presence that infiltrate from the road pavement and flow through damaged draining systems. The portions of the slab most affected by material degradation and presence of moisture, are the outer portions most exposed to weathering. In areas with intense water presence and with a highly degraded concrete, is often noticed the concrete cover expulsion and the corrosion of the reinforcement bars (Figure 36).

Figure 36. Photos of moisture, concrete spalling and steel corrosion in the concrete slabs.

The piers did not show structural defects, on the contrary, they show defects related only to water presence, as previously mentioned in the slab case.

These elements, as well, have more defects especially in the outer lateral faces and near the caps, where, often, water infiltrates from the road joint and stagnates on the top of the cap (Figure 37). An additional defect, that is associated with the pier element but relates to the bearings, are the defects found on the concrete pedestals of the supports that have the function of adjusting the elevation course of the bridge and transmitting loads to the pier cap. In many cases, these elements are made with a mixture of poor class concrete and show material degradation and compression cracks; such defects, if too significant, may compromise the statics of the supported beam (Figure 38).

Figure 37. Concrete spalling and reinforcement corrosion on pier caps and water infiltrations and stagnations on the top of the cap.

Figure 38. Cracks and concrete degradation on the support pedestals.

Supporting devices exhibit defects due to aging and weathering exposure, specially the ones with metal components which are subjected to oxidation and corrosion due to water infiltrations. The rubber bearings show aging of the rubber and, in some cases, crushing phenomena; in case of reinforced rubber devices, evidences of oxidation of the steel plates embedded in the rubber can be detected. Other characteristic defects are the presence of debris that can compromise the regular operativity of the devices and the incorrect installation. Some of the above mentioned defects are shown in Figure 39 below.

Figure 39. Oxidation and corrosion of metal support devices and crushing phenomena on reinforced rubber bearings.

The abutments are often affected by widespread phenomena of rainwater leakages due to the non-sealing of the pavement joint and/or the infiltration of water from the road embankment, which causing phenomena of concrete degradation and corrosion of the reinforcement bars. These defects on gravity abutments are not critical for the structure stability, as they are designed to resist the horizontal forces of the ground with their self dead weight, instead, they are characterized by large geometric sections with a large amount of reinforcements. Some pictures taken during inspections of three different bridges all with the same defect of drainage traces from the road embankment are shown in Figure 40: water infiltration and biological biofilms are visible on large portions of the concrete.

Figure 40. Photos of abutments affected by water infiltration from road embankment and pavement.

The most recurring defect on all beams, besides minor damages related to water and humidity presence, is to uncovered and oxidized stirrups which occurs locally in the slab bulb of the beams in the support area and diffusely on the lower flanges; such defect is, presumably, due to a poor concrete cover depth which, in some cases, is almost absent. On the external girders, more exposed to weather conditions, detachments of concrete cover were detected on the edges of the lower bulb, exposing reinforcements and prestressing cables that were oxidized and corroded (Figure 41).

Figure 41. Concrete spalling and steel corrosion on Prestressed RC beams.

In two bridges, where roads are overpassed, impact damages, which caused cover spalling and prestressing cables exposure, were detected, as it can be seen in the two pictures in Figure 42. On one of the two cases, the impact caused cables rupture that led to a significant resistance loss of the beam which show extended and intense bending and shear cracks; such element is no longer suitable to carry normal operating loads and the owner of the bridge proceeded to reduce the traffic lane.

Figure 42. Impact damages on the bottom flanges of the beams and crack patterns on concrete.

Additional defects can be found on the beams ends which can lead, if particularly significant and extended, to compromise the tensional state of the beam on the support cross-sections. Major defects detected are related to water presence coming from the road pavement that infiltrate through pavement joints placed on piers and abutments; the presence of water increase the concrete degradation and reinforcement corrosion with a consequent cover expulsion, as shown in Figure 43.

Figure 43. Concrete spalling and corrosion on the beam ends.

RC bridges with dapped-end beams

Among concrete bridges, two are made with a continuous scheme by adopting a symmetrical constraint scheme made isostatic with the use of drop-in dapped-end beams. In both cases, the deck is composed of three beams of variable heights. In accordance with bridges guidelines, the presence of dapped-end beams represent a critical element of the bridge; indeed, the presence of significant defects on the elements can weaken the ultimate capacity of the element and anticipate the fragile failure mechanisms, therefore, becoming a potential danger for the global stability of the bridge.

In detail, on the inspected bridges, common defects that were found are related to the presence of water infiltrations from the road pavement, in particular, at the road joints on the dapped-end beams. The water presence, especially on one of the inspected bridges, promoted concrete degradation and reinforcements corrosion which caused the expulsion of a portion of the concrete cover below the support section (Figure 44). The element geometry

makes visual inspection difficult and thus, the evaluation of the defectiveness level of the element; subsequent evaluation can be made once special inspections are planned and completed on such critical elements in accordance with bridges guidelines [26].

Figure 44. Concrete degradation, cover spalling and steel corrosion on dapped-beam ends.

On the other bridge, despite the clear evidence of water presence from road pavement, the concrete did not look excessively degraded and only few reinforcements were exposed and corroded. On this bridge, a significant structural failure of central piers, placed inside the riverbed, was observed, caused by a scour phenomenon. Pier foundations, affected by the abovementioned phenomenon, show diagonal cracks compatible with the failure and on-going kinematism (Figure 45). The displacement of the central piers caused a consequent deflection of the central spans which led to concrete crushing phenomena on the dapped ends (Figure 46).

Figure 45. Central pier scour (left) and diagonal cracks on the pier foundation (right).

Figure 46. Compression cracks and water traces on the dapped-beam ends.

Post-tensioned RC bridges with dapped-end beams

From the set of inspected bridges, 21 out of 43 is represented by prestressed concrete bridges with post-tensioned cables and out of these, 6 bridges are

characterized by dapped-ends beams. The presence of post-tensioned cables represents, in accordance with guidelines [26], a critical element that needs to be thoroughly investigated, even through special inspections, where the state of conservation of the prestressing system, in its entirety, is evaluated through destructive and semi-destructive in-situ tests. The criticality of such elements lie in the impossibility, from the outside, to evaluate the cables conservation state and possible defects inside the metallic ducts that are cast inside the concrete. The injection mortar inside the cables play a fundamental role in post-tension systems; to restore the section and to protect the cables inside from corrosion. The presence of empty spots inside the mortar can promote water entrance causing the corrosion of the high-tensile steel of the cables which, by working at high tensions, can instantly break and cause the bridge collapse. Anchorages, placed on the beams ends, and, often, in the slab in correspondence with support sections, are also subjected to material degradation caused by weather water infiltration phenomena; the condition of anchorages is important because their degradation can lead to tension loss on crucial sections of the beam like support sections.

The majority of bridges with post-tensioning cables without dapped-end beams display I-shaped beam sections which turn into a rectangular section at the supporting areas in order to hold anchorages in the beams ends. The other category of inspected post-tensed beam consists of 4-webs concrete box girder with Omega-shaped section. Usually, beams show the typical defects, easily encountered in other structural elements as well, such as humidity, degraded concrete, concrete cover detachments and damages along the stirrups.

In the case of post-tensioned girders, cracks presence is unusual and often related to prestressing tensions acting on the concrete which, according to Poisson's effect, cause the opening of cracks that develop along the cables pathway; both in the I-shaped beams and in the Omega-shaped, were detected the abovementioned cracks, especially on the lower face of the beam where the cables almost reach the concrete cover and near the cables anchorage areas. In Figure 47, some images displaying the defects abovementioned.

Figure 47. Humidity traces, concrete degradation and steel corrosion on box girders (upper) and cracks along the post-tensioning cable paths (lower).

Other structural elements such as piers, abutments, slabs, bearings and crossbeams show the defects previously illustrated for reinforced concrete bridges without critical elements.

Post-stressed bridges with dapped-end beams are characterized, as well, by I-section or omega box girders. The major defects found on I-shaped beams are related to water infiltrations from the roadway pavement at the anchorage end of the cable in the slab. The water by infiltrating from the slab caused severe degradation phenomena of the concrete and wide humidity areas where efflorescences and flowstones in variable colors going from white to orange for the presence of corroding products due to reinforcement bars corrosion, can be seen (Figure 48).

Figure 48. Damages on RC beams due to water infiltration: calthemite flowstone, reinforcement corrosion and concrete spalling.

The areas most affected by degradation are localized, often, near the bearings where the water can infiltrate more easily either through the anchor pockets

of the cables in the slab or through the road pavement joint. In some cases, dapped-beams ends show very extended cover detachments and both vertical and horizontal corroded reinforcements bars with significant loss of resistance area section; the defects are such to compromise the ultimate capacity of the element (Figure 49).

Figure 49. Damages on dapped-end beams due to water infiltration.

In addition, these bridges have dapped ends on the caps of the piers, which are also often very degraded, especially along the side faces that are more

exposed to weather agents. On the lateral faces, diagonal cracks, typical of the resistant strut-and-tie mechanism of dapped ends, are shown, suggesting a possible beginning of a failure mechanism (Figure 50).

Figure 50. Diagonal cracks on the dapped end of the pier caps.

The inspection of box girders is more complex because it requires entering the interior of the box to state the condition of the internal webs. The box decks inspected were found to have limited access to the inside of the box due

to a small opening on the end or none at all. Therefore, the inspection was only concerned with the external parts of the box. The defects found are the same as those found on the post-tensioned I-beams. These are typical defects of post-tensioned beams such as cracks along the cable path, cracks in the cable anchorage areas, and defects related to water infiltration.

In the box girders, large portions of the beam bottom face were found to be affected by white efflorescence and stalactites. This indicates that the caisson fills with water during heavy and prolonged rainfall. The presence of stagnant water inside the caisson is an alarming signal that necessitates more in-depth investigations, for example, by adopting endoscopic techniques. Some photos of the described defects are shown below (Figure 51)

Figure 51. Crack along the prestressed cable paths in the beam ends (left) and water stagnations inside the box girder (right).

Additionally, the three bridges with the Gerber's scheme exhibit significant deflection of the suspended beam between the two cantilevered girders. The deflection of the suspended spans could be attributed to excessive viscous effects of the concrete, indicating a low concrete class, significant prestressing losses, or a combination of both effects (Figure 52).

Figure 52. Permanent deflection of the suspended spans.

The dapped-beam ends of these bridges have complex geometry and are challenging to inspect from the inside. The supports are located inside the dapped ends and they are barely visible from the outside. The dapped ends are affected by widespread deterioration of both the concrete and the reinforcement bars. These bars are exposed to the weather and are severely corroded due to the detachment of large portions of the concrete cover (Figure 53).

Figure 53. Damages on box dapped-end beams due to water infiltration.

According to the bridge guidelines, high severity defects on critical elements such as prestressing cables or dapped ends elevate the vulnerability of the

structure to a High level of vulnerability. Consequently, the overall attention class is High. On two bridges in particular, a potential alarm bell was identified, namely the presence of moisture along the paths of the cables. This defect is alarming and necessitates further investigation to verify the actual presence of defects within the cable ducts. In detail, as shown by the photos taken during the inspection and superimposing the available technical drawings (Figure 54), traces of moisture in one case and traces of white efflorescence at the cables of the beams can be seen.

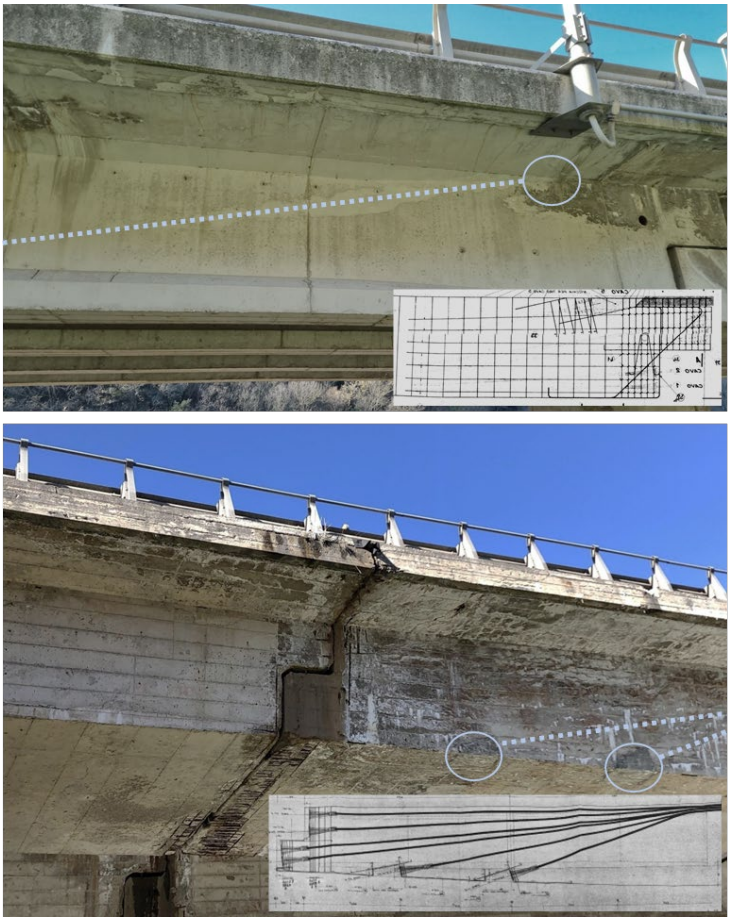

Figure 54. Water infiltration on grouted ducts of prestressing system.

Finally, on the two bridges with box girders possible cracking patterns are found, consistent with well-known failure mechanisms reported in technical literature. As shown in Figure 55a, in the nib region characterized by a rather widespread cracking pattern, a longitudinal crack is located along the path of the longitudinal bars approaching the nib inner corner. In the second case shown in Figure 55b, the resistant mechanism led to the opening of diagonal cracks starting from the lower corner of the nib full-depth interface.

Figure 55. Potential failure mechanism of the box dapped-end beams.

The inspection campaign carried out as part of the ANAS-FABRE project highlight the major critical issues concerning the existing bridges, especially, those characterized by pre-tensioning systems and half-joint connections. The major defects found are related to water infiltrations that should be prevented as much as possible. Pre-stressed girders, in particular those with post-tensioning system and dapped ends, present critical aspects that need an in-depth investigations to determine their state of preservation. The safety of these bridges is strictly connected to the local safety assessment of these elements, which turns out not to be a simple task.

So in the following chapters, the current state of the art on ultimate capacity assessment of saddles will be presented, focusing on the use of strut-and-tie models for capacity assessment and the experimental campaigns conducted to study the failure behavior of these elements. Next, two experimental campaigns will be presented, one in the laboratory and the other in situ on an existing bridge.

3 Dapped-end beams: State of the Art

The first use of dapped-end beams in bridge construction dates back to the second half of the 1800 by the German engineer Heinrich Gerber. The dapped-end beams, also referred to as half-joint beams, are frequently used in construction, particularly in precast concrete structures and cantilevered bridges. These beams feature a protruding nib at one or both ends, depending on the structural design. The nib is typically created by reducing the height of the beam current section while maintaining the same width. Generally, the ratio of the nib height to the full-depth section is larger than 0.45.

The dapped-end beams are a common choice in many countries because they offer several benefits, such as (i) making it easier to join elements, especially those that are precast, (ii) reducing the total height of elements with large cross-sections height to simplify their installation, and (iii) enhancing the lateral stability. These dapped ends have been extensively investigated by both numerical and experimental methods over the years. Here below are presented the main studies and recommendations that have emerged since the first technical guidelines were issued around the 1970s.

1971: PCI Design Hanbook [32]

The first normative recommendations for the design of dapped-end beams are included in the design book of the Precast and Prestressed Institute, where the geometric ratios between horizontal and vertical reinforcements and the geometry of the element are given (Figure 56).

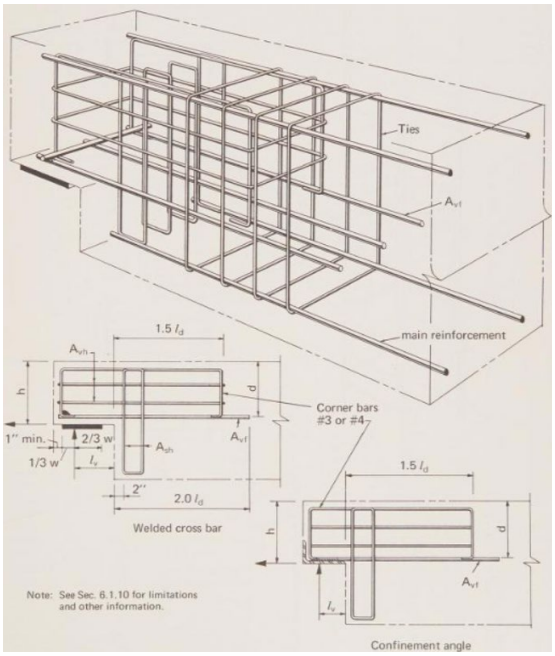

Figure 56. Reinforcement for dapped-end beam from the PCI Design Handbook 1971.

At that time, there were no specific standards for the shear design of half-joints; in fact, the level of shear stress for the first concrete cracking started from the inner corner of the nib and the shear strength contribution of the concrete were not known.

1973: Werner e Dilger [22]

Werner and Dilger investigated the shear force related to first concrete cracking through analytical FE models and studied the strength contribution of the concrete with an experimental campaign of five pretensioned dapped-end beams, which were led to failure with a 4-point tests.

1974: Leonhardt and Monning [33]

In Europe, the first guidance on the design and verification of half-joints is presented by Leonhardt and Monning in the first German language edition of the 1973 Handbook of Concrete Construction; The first Italian edition of the book dates back to 1977 [34]. The dapped-end beam design is based on strut and tie models that vary according to the chosen reinforcement configuration. Generally, there are 3 common reinforcement configurations for designing dapped-beam ends:

- Vertical and horizontal reinforcements: the resistant mechanism involves the vertical reinforcements in enough quantity to withstand all the design shear at the bearing and the horizontal reinforcements, which must resist the tensile stresses generated by the inclined strut in the support section.

- Diagonal reinforcements: the resistance mechanism involves the diagonal reinforcement that carries the shear forces to the support section, where a compressed strut forms and transfers the load to the support.

- The resistant mechanism relies on the combination of both reinforcement configurations

The resistance mechanisms are presented as strut-and-tie models, where both geometric limitations of the elements and prohibited construction details, such as insufficient bar anchorage lengths or incorrect bends, are shown in

Figure 57. The verification and sizing of the reinforcement are done by solving the equilibrium of the internal nodes of the strut-and-tie models.

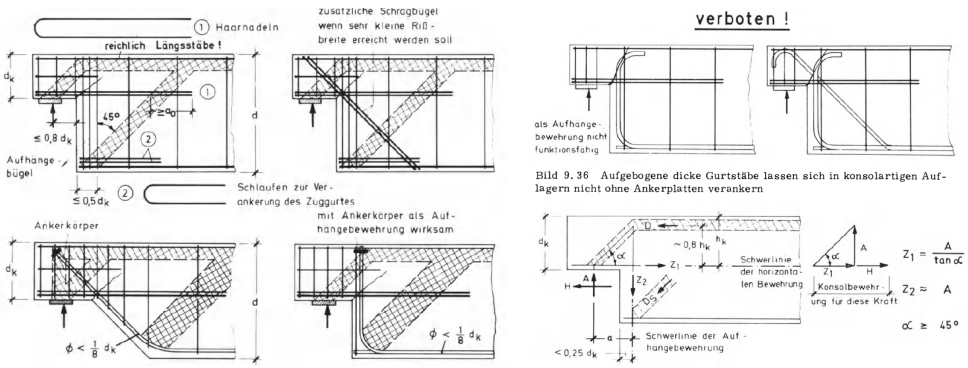

Figure 57. Strut-and-tie models for dapped-end beams from the Handbook of Concrete Construction [33].

1979: Mattock and Chan [4]

Contrary to corbels, where inclined compression strength is balanced by column compression [35], the dapped-beam ends must have a specific vertical or diagonal reinforcement positioned near the internal face of the nib. Mattock and Chan start from the results of the Werner and Dilger experimental campaign [22] to study the behavior of dapped-beam ends. They conducted experimental tests four specimens subjected to both shear and axial forces and four specimens only shear forces, for a total of 16 dapped-beam ends to test. They performed three-point asymmetric bending tests to test the specimen end at a time without damaging the other. The samples have a reinforcement layout with vertical and horizontal bars. The authors identify two possible failure mechanisms for this rebar configuration (see Figure 58): the first one involves the formation of a diagonal crack which starts from the inner corner A of the nib and develops at a 45-degree angle until it reaches the top face of

the beam in correspondence with the ideal rotation point Y; the second one involves the formation of a diagonal crack with the same angle that starts from the bottom corner of the full-depth section and reaches the ideal rotation point Z. They applied the load at the Y point in six specimens and at the Z point in two specimens.

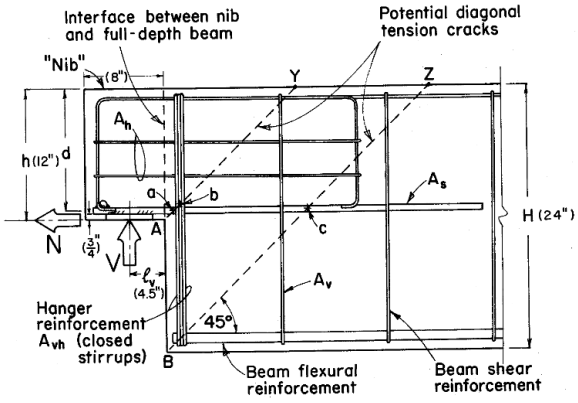

Figure 58. Dapped-end reinforcement and potential diagonal cracks by Mattock and Chan [4].

The test results show a similar fracture process for all specimens, which effectively confirms the hypothesized failure mechanisms. The first cracks on the inner corner of the nib start at an applied load of 20 per cent of the ultimate load, which is reached only after the main reinforcements of the dapped-beam end have yielded.

1983: Liem [5]

Liem conducted an experimental campaign on six corbels and four dapped-end beams with a reinforcement layout composed of diagonal bars and horizontal bars to study their ultimate capacity and their fracture behavior, which was compared with that obtained by the Mattock's group for the dapped-end beams with vertical and horizontal reinforcements. The four

dapped-end beams were made from the same resistant class of concrete by varying the diagonal bar diameter and dapped-beam end geometry; the test was performed on three points with an asymmetrical configuration, similar to those of Mattock and Chan (Figure 59). The results showed that:

- the standards of the time were inadequate to estimate the shear strength in the case of inclined reinforcement;
- the dapped-beam end strength was governed by the weakest element between steel and concrete;
- to prevent brittle fracture, the strength of the steel had to be limited;
- the solution with inclined reinforcement was more economical than the one with vertical and horizontal reinforcements.

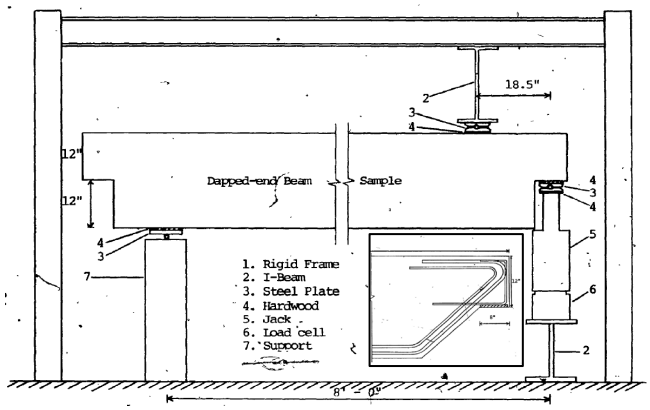

Figure 59. Testing set-up and detail of reinforcement layout of the dapped-beam ends by Liem [8].

1987: Schaich et al. [36]

An important step forward in the use of strut-and-tie models in the design of structures is made with the study of Schaich et al., which present a generalized approach for the use of strut-and-tie models for the evaluation of the service

limit state and ultimate limit state in the cracked condition. The proposed procedure also demonstrates that the behavior of reinforced and prestressed concrete elements is the same under acting loads. presented it as a general model to determine load paths within the structures. The proposed generalized procedure for analyzing a complex structure is based on identifying and subdividing the structure into its 'Bernoulli' and 'Disturbed' regions (Figure 60): the former represents the portions of the structure where the Bernoulli's assumptions are complied and their internal stress state can be derived from the sectional forces, the latter represents the disturbed regions where the strain distribution is significantly nonlinear due to, for example, concentrated loads, geometric discontinuities like openings or corner, and the Bernoulli's assumptions are no longer valid.

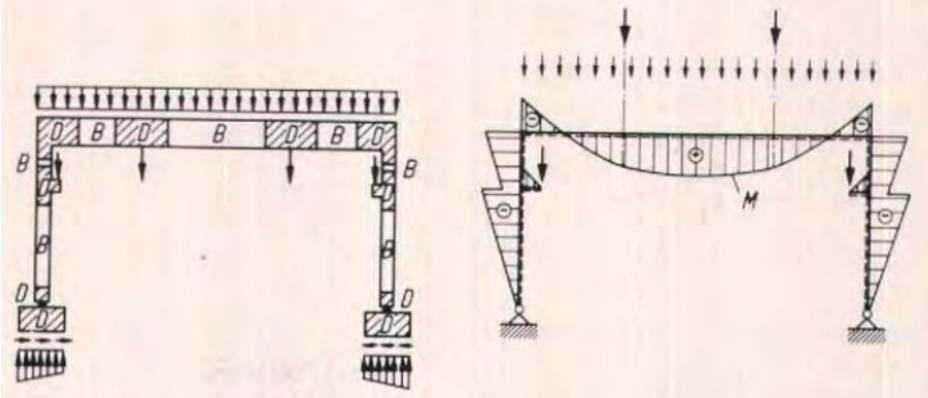

Figure 60. D-regions and B-regions of a frame structure by Schaich et al. [9].

B-regions can be sized using the standard models adopted in the technical standards, while D-regions can be designed using the standard methods if the tensile stresses do not cause the concrete to crack, or with strut-and-tie models if the tensile strength of the concrete is exceeded. In the latter case, the D-

region design can proceed by developing a strut-and-tie model that can represent the true path of the loads, calculating the forces acting on struts and ties such that equilibrium is satisfied, and sizing the struts, ties and nodes. This method is limited to structures designed in accordance with the lower bound theorem of plasticity, so the internal forces that satisfy the internal equilibrium should be chosen such that the limit rotation capacity is not exceeded at any point before plasticity is reached in the rest of the structure (small deformations).

1990: Mader [23]

Mader investigated three methods from the literature for the design of prestressed dapped-end beams (PCI design– Menon/Furlong– strut-and-tie), focusing on the prestressing force contribution in the design procedure. The methods were validated with laboratory tests in order to examine the effect of prestressing forces on the load path; four different constructive details were used for each end of two prestressed dapped-end beams. The results showed that in all cases, the specimens had about 15-20% higher ultimate capacity than predicted, except for the specimen designed according to PCI, which had lower ultimate capacity due to poor construction details. In all cases, the first cracking started on the inner corner of the nib, and in the specimen based on the strut-and-tie model, the cracks propagated more across the full-depth beam. The strut-and-tie model estimate of the ultimate capacity was lower than the experimental one, confirming that this solution is conservative and represents the lower bound of plasticity.

1991: Mitchell and Cook [37]

Mitchell and Cook presented the Canadian standards design procedure for disturbed zones, and they presented an application example on a beam with dapped ends using both strut-and-tie model and nonlinear analysis (stress fields). The strut-and-tie models, under strain compatibility conditions, proved to be valuable for studying disturbed zones, but the nonlinear analysis with stress fields was revealed to be a more sophisticated tool for the verification of serviceability and ultimate limit states.

1992: C.N.R 10037-86 [38]

In 1992, the first Italian normative prescriptions on the design and verification of dapped-beam ends with vertical and horizontal reinforcements or diagonal reinforcements based on strut-and-tie models were published by the National Research Council (C.N.R.) in the bulletin 10037/86. The resisting mechanisms considered at the ultimate limit state correspond to these two mechanisms identified by Mattock's group, as shown in Figure 61.

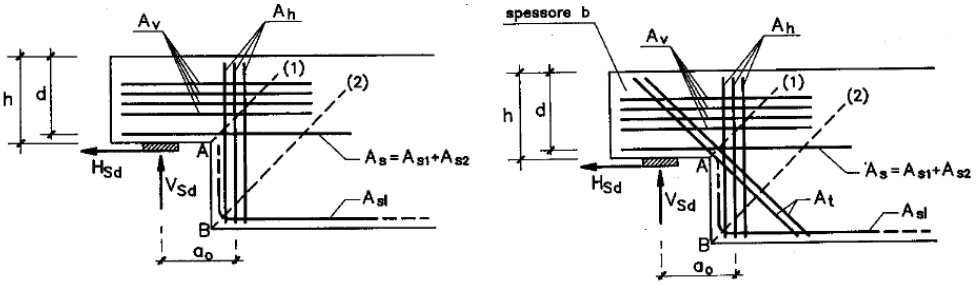

Figure 61. Failure mechanisms from the C.N.R. 10037/86 [10].

The ultimate capacity of the dapped-beam end is calculated by considering the resistant mechanisms offered by the concrete section of the nib, the

vertical reinforcements or vertical and diagonal reinforcements and the horizontal reinforcement across the nib.

1996: Muttoni et al. [39]

The authors investigated the behavior and strength of simple reinforced concrete or prestressed concrete structures by adopting the stress fields method. The earliest applications of this method date back to Ritter and Morsch and were later extended to plasticity theory by Drucker and studied by numerous authors such as Thürlimann, Nielsen, Müller, Collins and Mitchell, to name a few. Stress field theory considers three-dimensional structural elements as two-dimensional elements, assuming that the plane stress conditions found do not vary along the thickness of the element. Two-dimensional elements are statically indeterminate and therefore admit an infinite number of stress states that satisfy equilibrium. By adopting the lower bound theorem of plasticity theory, it is possible to find an admissible stress field or combination of fields that solves the indeterminate problem. The stress fields have also been adopted to evaluate the capacity of beams with dapped ends and openings.

2002: Chen et al. [6]

The authors verified the reliability of strut-and-tie models for dapped-end beams with an opening near the inner nib corner by testing four small-scale specimens with different reinforcement layouts and characterized by a geometrical ratio between length and height of the nib equals to 1.5. The strut-and-tie models also proved to be conservative for dapped-end beams with an opening.

2002: Nanni and Huang [24]

Nanni and Huang designed two prestressed dapped-end beams according to PCI standards and performed three-point asymmetrical tests to measure the shear capacity of the specimens, using a shear span to full-depth ratio of 3.44 for the first specimen and 2.14 for the second specimen. In both tests, cracks formed on the re-entrant corner of the nib, but the shear-flexure failure on the full-depth portion of the beams anticipated the shear failure of the dapped ends.

2003: Lin et al. [7]

The authors investigated the influence of the dapped end geometry by carrying out a laboratory experimental campaign on 24 beams, varying the nominal shear span (distance between support and vertical reinforcements) to nib depth ratio and reinforcement layout. Tests were performed on three points to test one end of the beam at a time. The tests showed that the shear strength increased as the nominal shear span-to-depth ratio decreased and the quantity of main reinforcement or the concrete compressive strength increased. A simplified strut-and-tie model called Softened strut-and-tie model was proposed and validated through the collected experimental data.

2003: Lu et al. [8]

The authors have conducted an experimental campaign on 12 dapped-end beams, varying the nominal shear span-to- depth ratio, each with a cross-section of 300x600 mm and a length of 3000 mm, made of high-strength concrete. The aim was to verify the adequacy of the existing PCI and Mattock and Chan design methods. The tests were carried out with a 3-points bending procedure, similar to those of Mattock and Chan, with a load point placed at

650 mm (shear span equal to 1.08). The force applied at failure varied from a minimum of 378 kN to a maximum of 893 kN. The results showed that the models in the standards underestimate the strength of the dapped ends. Furthermore, it was observed that the shear strength increases as the reinforcement increases and the nominal shear span-to-depth ratio decreases.

2005: Wang et al. [9]

An experimental campaign was conducted on 24 dapped-end beams to study the influence of parameters such as the nib depth, the stirrup spacing and the anchorage length of the longitudinal bars on the ultimate shear capacity of the dapped-beam ends. The conclusions drawn were as follows: the depth of the nib should be greater than 0.45H (H, full-depth of the beam), the shear reinforcement should be positioned as close as possible to the nib full-depth interface, and should extend for at least 0.5 times the half-depth of the nib.

2012: Lu et al. [10]

Experiments were conducted on 24 dapped-end beams to investigate the impact of concrete strength, the nominal shear span-to-depth ratio a/d, and the horizontal loads on the ultimate capacity. The results revealed that the capacity increases with the increasing of the concrete strength and with the decreasing of the *a/d* ratio and decreases with an increase in the horizontal bearing load.

2014: Moreno-Martinez et al. [25]

Four distinct tests were conducted on dapped-end beams, each with unique construction details:

- E1: Constructed using standard construction details.

- E2: Built similarly to E1, but with the addition of prestressing in the lower part of the dapped ends (147kN).
- E3: Half of the vertical stirrups were replaced with diagonal rebars.
- E4: Constructed with the same details as E3, but with the addition of prestressing, although lower than E2.

The results indicated that diagonal bars proved to be more effective than vertical ones. Furthermore, the introduction of prestressing enhanced the capacity of the dapped ends in terms of both crack opening and ultimate load.

2015: Aswin et al. [11]

Tests on 4 beams by varying the reinforcement detail and quantity. The results were compared with a FE model and S&T models available in the codes (ACI code, FIP, Eurocode 2 and Canadian code).

2015: Lu et al. [12]

The authors have revisited the experiments conducted in 2003 and 2012, but this time, they used an *a/d* ratio greater than unity, with the aim of validating their Softened Strut and Tie Model (SST). It's important to note that all these dapped-end beams collapse with a bending failure. For enhanced ductility, the authors recommend using a minimal amount of bending reinforcement.

2016: Desnerck et al. [13]

The authors conducted a study on different reinforcement layouts and compared the final results. In total, four dapped-end beams were constructed. The results revealed that the strut and tie models were too conservative for predicting the ultimate capacity. In all specimens, the first cracking occurred in the re-entrant corner of the nib at 20-30% of the ultimate load. The most

significant impact on the ultimate load was due to the presence or absence of the diagonal bars, which resulted in a 40% change. Conversely, a reduction in the stirrups led to a 10% decrease in the ultimate load.

2016: Oviedo et al. [14]

The authors reproduced 4 dapped-end beams based on the Chen's group specimens and 5 beams corresponding based on the design models presented by Herranz et al. (2012). The estimates made of the ultimate capacity were conservative for all cases.

2017: Desnerck et al. [15]

The authors conducted an in-depth investigation into the effects of various factors on the ultimate capacity of the dapped-beam ends. These factors included corrosion, cracking along the longitudinal tension bars, a limited quantity of stirrups, and insufficient construction details such as poor anchorage length. From the specimens studied, it was observed that the decrease in the concrete's compressive strength had a negligible impact. Instead, the failure was primarily governed by the yielding of the bars. A significant 35% decrease in capacity was noted when there was a 50% reduction in the main reinforcement of the dapped end, which included both diagonal and vertical reinforcements. Insufficient construction details contributed to a 10% reduction in capacity. Interestingly, the effects were more pronounced when defects were combined. For instance, cracking along the longitudinal bars coupled with poor construction details led to a 40% reduction in capacity. Furthermore, even the addition of a small amount of reinforcement resulted in a substantial 60% reduction in capacity. As a note from the authors, during inspections, greater attention should be paid to the

load path. The possibility of combined effects should also be carefully evaluated.

2018: Desnerck et al. [16]

The authors conducted an investigation into the potential degradation effects on 12 dapped-end beams. These effects included cracking, local reduction of reinforcement, detachment of cover, anchorages, and reduced concrete strength. The experimental data were then compared with the expected ultimate strength derived from strut-and-tie models; the ratio between the two ultimate capacity was observed to vary within a range of 1.25 and 2.5. The results indicated that if cracks are present, the authors suggest reducing the confinement by a factor ranging from 0.85 to 0.3. In some cases, even the absence of confinement could be considered. For the S&T models, the most severe condition appears to be poor anchorage of the ties. A lack of anchorage of the diagonal bars leads to a significant reduction in ultimate capacity. However, this finding was not confirmed by the experimental results.

2019: Mata-Falcón et al. [17]

The authors have proposed a procedure to define strut-and-tie models, taking into account the effect of the expulsion of the cover in the CCT node above the main vertical reinforcements of the dapped ends in the failure mechanism. They constructed 28 dapped-end beams, using 15 different reinforcement configurations. The results indicated that the failure of the CCT node leads to a reduction in the ultimate capacity of the dapped ends. Verification of the node with the standards resulted in non-conservative outcomes when the contribution of the concrete cover was not neglected.

2022: Asso et al. [40]

The authors provide a comprehensive review of the state of the art on dapped-beam ends, with a particular focus on the Desnerck's research group. They highlight the fundamental parameters governing the problem and detail the setup of the tests performed. In an effort to replicate Desnerck's experiments, they utilized FE models to simulate the experimental test. The modelling was specifically focused on the area in the vicinity of the dapped end, with the carriage positioned at the opposite end.

2022: Rajapakse et al. [19]

The authors conducted an investigation into the bending and shear failure mechanisms of the dapped-end beams. They created 8 specimens with varying configurations of vertical and horizontal reinforcements. The fracture tests were performed using three-point asymmetrical bending tests, adopting a shear span-to-depth ratio of 1.75. The results indicated that by doubling the amount of vertical reinforcement, the ultimate capacity of the dapped end increased by approximately 15%. Furthermore, the contribution of horizontal reinforcement in limiting the opening of cracks under working loads increased as the amount of reinforcement increased, but this effect was limited; greater control of cracking could be achieved by inserting diagonal reinforcements.

2022: Rosso et al. [41]

The authors conducted numerical analyses to assess the impact of corrosion on the ultimate capacity of dapped-end beams. These analyses were performed on two case studies: the specimen tested by the Desnerck's group and the dapped-beam end of an existing bridge. Corrosion levels ranging from

5% to 50%, in increments of 5%, were tested. This was done by reducing both the section and ductility of the reinforcement subject to corrosion. The Desnerck's specimen demonstrated a progressive reduction in the ultimate capacity of the element. However, the dapped end based on the existing bridge did not exhibit a significant reduction in capacity.

2023: Aksoylu et al. [20]

An experimental campaign was conducted on 6 dapped-end beams to explore the influence of the ratios of nominal shear span to depth and shear span to depth (relative distance between support and point of load application). These experimental tests were complemented by numerical simulations to assess their accuracy. The results indicated that an increase in the shear span-to-depth ratio leads to a shift in the failure of the element from shear failure to flexural failure. Additionally, a lower nominal shear span-depth ratio ensures a higher ultimate capacity of the element.

2023: Di Carlo et al. [21]

The authors conducted an investigation into the impact of corrosion on the ultimate capacity of beams with dapped ends. They constructed 2 specimens, designed with strut-and-tie models, each with different quantities of reinforcement. These specimens were subjected to induced corrosion, resulting in a 15% mass loss. The results revealed a significant reduction in ultimate capacity of up to 40%. It was also observed that pitting phenomena can alter the failure mechanism.

As the above mentioned technical literature has shown, the dapped-end beams studies are extensive, encompassing both theoretical and experimental investigations, but many aspects remain unexplored. This is particularly true

when it comes to assessing the safety of dapped-end beams on existing bridges. The catastrophic collapses of the Concorde overpass in 2006 [1], and the more recent collapses of the Annone [2] and Morandi bridges in 2016 and 2018 respectively, have led to a dramatic increase in experimental and numerical studies. These studies aim to deepen our understanding of dapped ends, particularly the prestressed dapped-beam ends, in order to provide a more accurate safety assessment of existing structures.

The potential impact of the level of prestressing on the ultimate capacity and the element's failure mechanism remains largely unexplored. Furthermore, the validity of simplified strut-and-tie models, which have been modified to include the contribution of prestressing, has not been fully validated experimentally. To further investigate this subject, the subsequent chapters will present a comprehensive experimental campaign. This campaign will encompass both laboratory tests and in-situ tests conducted on an existing bridge girder. The laboratory tests aim to study the influence of varying levels of prestressing on the resistance mechanisms of dapped ends. This will be achieved by testing six laboratory specimens, each based on the beam of an existing bridge and characterized by different levels of prestressing. The design of the samples and the experimental campaign will be integrated by a numerical investigation. This investigation will utilize refined finite element models to predict the ultimate capacity of the saddle and to evaluate the effectiveness of these elements for a potential safety verification of the dapped-end beams. The comprehensive in-situ experimental campaign will enable the evaluation of the actual capacity of an existing bridge girder. It will also assess the reliability of non-destructive and semi-destructive tests, with

the aim of conducting a special inspection on a prestressed girder with dapped ends.

4 Laboratory experimental campaign on dapped end beams

As previously stated, while numerous studies in the literature present experimental investigations on the shear behaviour and ultimate capacity of dapped-beam ends, only a few focus on prestressed dapped end beams. To gain a deeper understanding of the contribution made by prestressing tendons to the shear resistance mechanism, an extensive experimental campaign has been developed. This campaign includes tests on a real bridge's dapped-end beam and laboratory-scale specimens.

Test set up

In order to study the potential resistance mechanisms of an existing prestressed dapped ends, with a focus on how the residual prestressing level affects the ultimate shear capacity, the reinforcement layout of a real bridge girder has been adopted for the design of laboratory scale specimens.

As well-known in literature since the Galileo's publication of "Dialogues Concerning Two New Sciences", numerous studies have been done about the scaling to identify independent and size-dependent physical quantities, first of all, the notorious theorem proposed by Buckingham in 1914 [42]. In the experimental practise of civil engineering the most common similitude laws are the mass-based, the time-based and acceleration-based, whose choice depends on the phenomena which are simulated [43]; in detail, since the quasistatic loading method will be used and the time and inertial forced

effects can be neglected, the mass-based similitude law is adopted to define the geometry and reinforcement layout of the specimens.

The specimens are designed as laboratory-scaled models, with the same geometric and reinforcement quantity ratios of the existing bridge girder.

The experimental program consists of testing six dapped end beams to evaluate their ultimate capacity, adopting the three-point non-symmetric bending method which allows to test each beam half-joints, for a total of twelve specimens. Starting from zero, three different levels of pretension are considered, 760 MPa – 640 MPa and 0 MPa, which represent, respectively, the pretension after a 20%, ~30% and 100% long term losses and applied to five of six beams with same layout and amount of reinforcements. For the highest pretension value, in order to investigate more deeply the pretension contribution, two typical defects are introduced, in detail: the corrosion of vertical and horizontal main reinforcements of the nib and the insufficient amount of stirrups in the beam support region. Finally an ordinary reinforcement concrete dapped end beam is built with same reinforcement layout of the undamaged specimens.

Dapped end beam design

The design of the half-joints is based on an existing RC prestressed bridge girder, which represents a common solution for mid-span bridges during the ‘70s and ‘80s and widely spread in the Italian territory. The description of this existing bridge design is reported hereafter.

The bridge was built in the early of the '80s and consists of 8 simply supported spans approximately 35 m long, for a total length of 280 m . The deck is

composed of four 1.8 m high I-shaped pre-stressed RC beams, connected by means of 4 pre-stressed RC transverse beams per span and by a 0.32 m thick RC slab. All the supports are made by rectangular neoprene pad with dimensions of 0.6 x 0.4 m and 38 mm thick. The lateral view of the girder is reported below (Figure 62a).

The design prestressed level is reached through a post-tensioning system composed of 5 high-tensile steel tendons, each consisting of 32 wires of 7 mm diameter, with an optimized curved profile. Four of five tendons extend up to the half-joint, in which the anchorages are placed (Figure 62b): two of them are anchored at an 8 degree angle in the nib, the other are anchored horizontally in the interface of nib and full-depth beam.

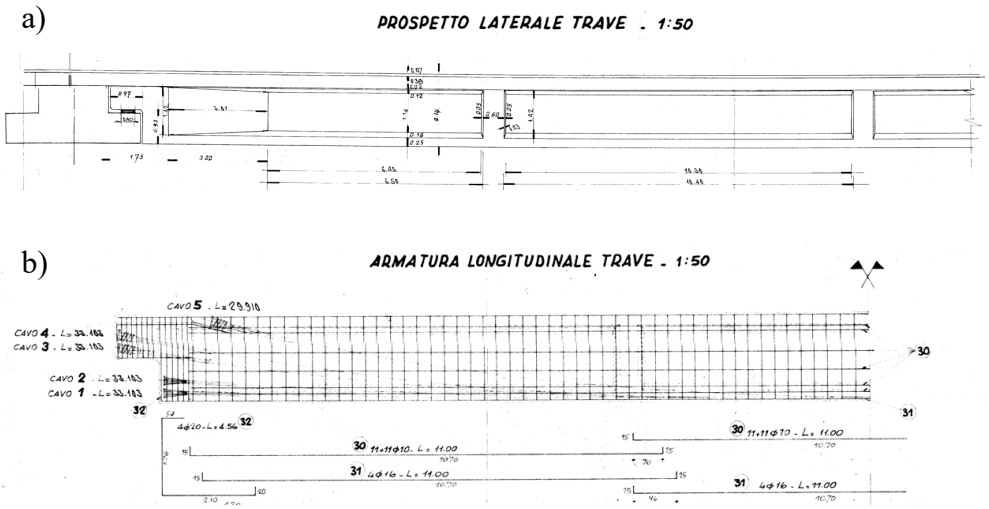

Figure 62. Lateral view of I-shaped RC beam (a) and post-tensioning system layout (b).

The half-joint is constituted of 0.85 m nib height, which extends over a length of 0.97 m, and a full-depth section of 1.79 m height and 0.65 m width (Figure 63a). The geometry of the half-joint can be express according to the literature

through two dimensional ratios equal to: the nib height h_n over the full-depth section h and the length nib l_n over the nib height h_n [13]. The obtained ratio are respectively 0.47 and 1.14. The contribution of both vertical and diagonal bars and refined shear reinforcements are used in the reinforcement layout (Figure 63b).

a)

b)

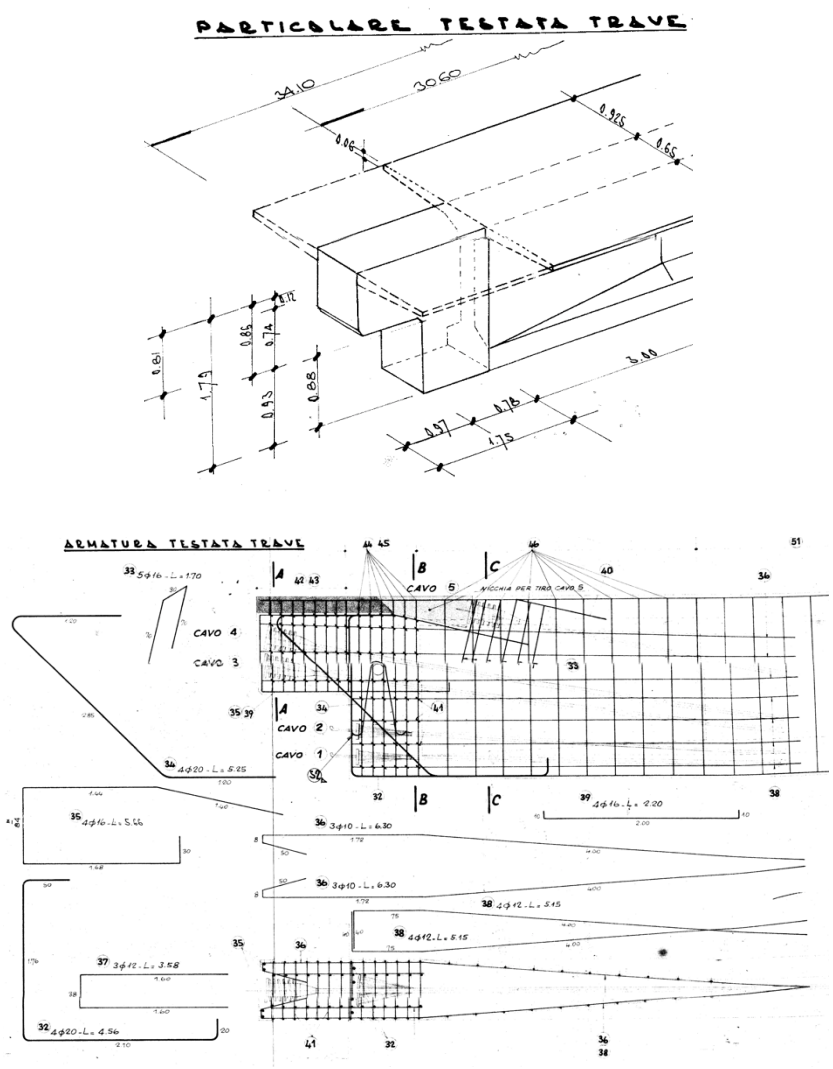

Figure 63. Geometry details (a) and reinforcement layout (b) of the half-joint.

The specimens are designed as dapped-end beams adopting the half-joint dimensional ratios, h_n/h and l_n/h_n, equal to 0.5 and 1.0, which are widely common in the technical literature [8–10,37,44]. The beams have a rectangular full-depth section of 0.6 m height and 0.22 m wide, for a total length of 3.5 m and they present, on both their ends, two nibs with height of 0.3 m and length of 0.3 m. The nib height and length ratios between the real design geometry and the specimens are, respectively, equal to 2.83 and 3.23. In the full-depth section of the beams, the width and height ratios of the section between the real beam geometry and the specimens are 2.95 and 3.

The concrete material is made with a mix design conforming to the European standard to achieve the strength class of C40/50 and the S5 workability class [45]. The concrete casting will be executed at the precast manufacturer and the concrete curing time will be 28 days. The developed compressive strength and the modulus of elasticity of the concrete will be measured by testing cubes and cylinders. The reinforcement bars are made by thermomechanically rolled steel B450C designed for reinforced concrete structures and complying with both the European and Italian standards [45]: the main mechanical properties yield strength, f_y, and tensile strength, f_u, are respectively 450 MPa and 540 MPa. Samples of rebars for each adopted diameters will be tested to confirm the expected values.

Based on the reinforcement layout of the existing bridge girder, which was scaled with a scale factor of 1:3, in order to respect the dimensional ratio of the concrete and reinforcement area, the reinforcement layout A (RL-A) is developed and used in four specimens; in details, the main half-joint reinforcement is composed by both vertical (2ϕ8+2ϕ6) and horizontal

(2ϕ8+2ϕ6) bars, at the distance of 15 mm, respectively, from the nib and full-depth interface and from the lower nib face and four diagonal bar (2ϕ8+2ϕ6) with a 45˚ angle. The D-region is strengthened with the four-legged stirrups (4ϕ8/5") in the nib and the two-legged stirrups (2ϕ8/6.5") in the full-depth section, respectively, with a minimum spacing of 50 mm and 65 mm. The design prestressing levels are obtain through the post-tensioning system constituted of two WR18 Dywidag Threadbars, with 17.5 mm nominal diameter, placed inside the metallic duct and injected with cementitious grout once the prestressing level is reached. It is worth noting that although cables are used in the real beam, threaded bars are adopted in the specimens to facilitate tensioning procedures in the laboratory facility. The upper bar has a curvilinear path obtained by cold-bending, with a radius of curvature of 8 m, which is greater than the minimum bending radius of 3.5 m according to the ETA-05/0123 standards, and is anchored into the nib with an inclination of 8 degrees. The lower bar is anchored at the nib full-depth interface with a straight path. In order to prevent the bending failure of the beams and the shear failure outside the D-Region, additional bending bars (3ϕ18) and stirrups (2ϕ8/25") are inserted; in detail, these reinforcements are opportunely designed of the expected ultimate applied load during the test by simulating the failure tests with progressively more refined models, starting with simplified strut-and-tie models and then two-dimensional and three-dimensional finite element models. Finally, horizontal bars (2ϕ6) are used on the whole beam with a 15 cm spacing. A detailed scheme of the reinforcement layout A is reported below in Figure 64a.

To highlight the contribution of shear reinforcements on the ultimate shear capacity, the reinforcement layout B is adopted on one specimen, which is

characterized by a prestressing level of 760 MPa and a 50% reduction of the stirrups in the D-Region with respect to the layout A: four-legged stirrups with 10 cm spacing in the nib (4ϕ8/10”) and two-legged 13 cm spaced stirrups (2ϕ8/13”) in the full-depth section (Figure 64b).

The last reinforcement configuration C used in the last specimen is the equivalent of the layout A without the prestressing system (Figure 64c).

The total number of specimens with relative nomenclature is shown below:

- **RL-A1**: specimen with the reinforcement layout A and the first level of prestressing equals to 760 MPa foreach high-tensile bar.
- **RL-A2**: specimen with the reinforcement layout A and the second level of prestressing equals to 640 MPa foreach high-tensile bar.
- **RL-A3**: specimen with the reinforcement layout A without the prestressing level.
- **RL-A1D**: specimen with the reinforcement layout A and the first level of prestressing equals to 760 MPa foreach high-tensile bar. In this case, a 20% area loss of the main half-joint rebars is induced by accelerated corrosion.
- **RL-B1**: specimen with the reinforcement layout B and the first level of prestressing equals to 760 MPa foreach high-tensile bar.
- **RL-C**: specimen with the reinforcement layout C.

The main characteristics of the specimens are summarized in Table 2.

Table 2. Main characteristics and reinforcement layout of the specimens.

Spec.	Prestressing	Vertical	Horizontal	Diagonal	Stirrups
[-]	[MPa]	[-]	[-]	[-]	[-]
RL-A1	760	2ϕ8+2ϕ6	2ϕ8+2ϕ6	2ϕ8+2ϕ6	4ϕ8/5”
RL-A2	640	2ϕ8+2ϕ6	2ϕ8+2ϕ6	2ϕ8+2ϕ6	4ϕ8/5”
RL-A3	0	2ϕ8+2ϕ6	2ϕ8+2ϕ6	2ϕ8+2ϕ6	4ϕ8/5”
RL-A1D	760	2ϕ8+2ϕ6	2ϕ8+2ϕ6	2ϕ8+2ϕ6	4ϕ8/5”
RL-B1	760	2ϕ8+2ϕ6	2ϕ8+2ϕ6	2ϕ8+2ϕ6	4ϕ8/10”
RL-C	No Prestressing	2ϕ8+2ϕ6	2ϕ8+2ϕ6	2ϕ8+2ϕ6	4ϕ8/5”

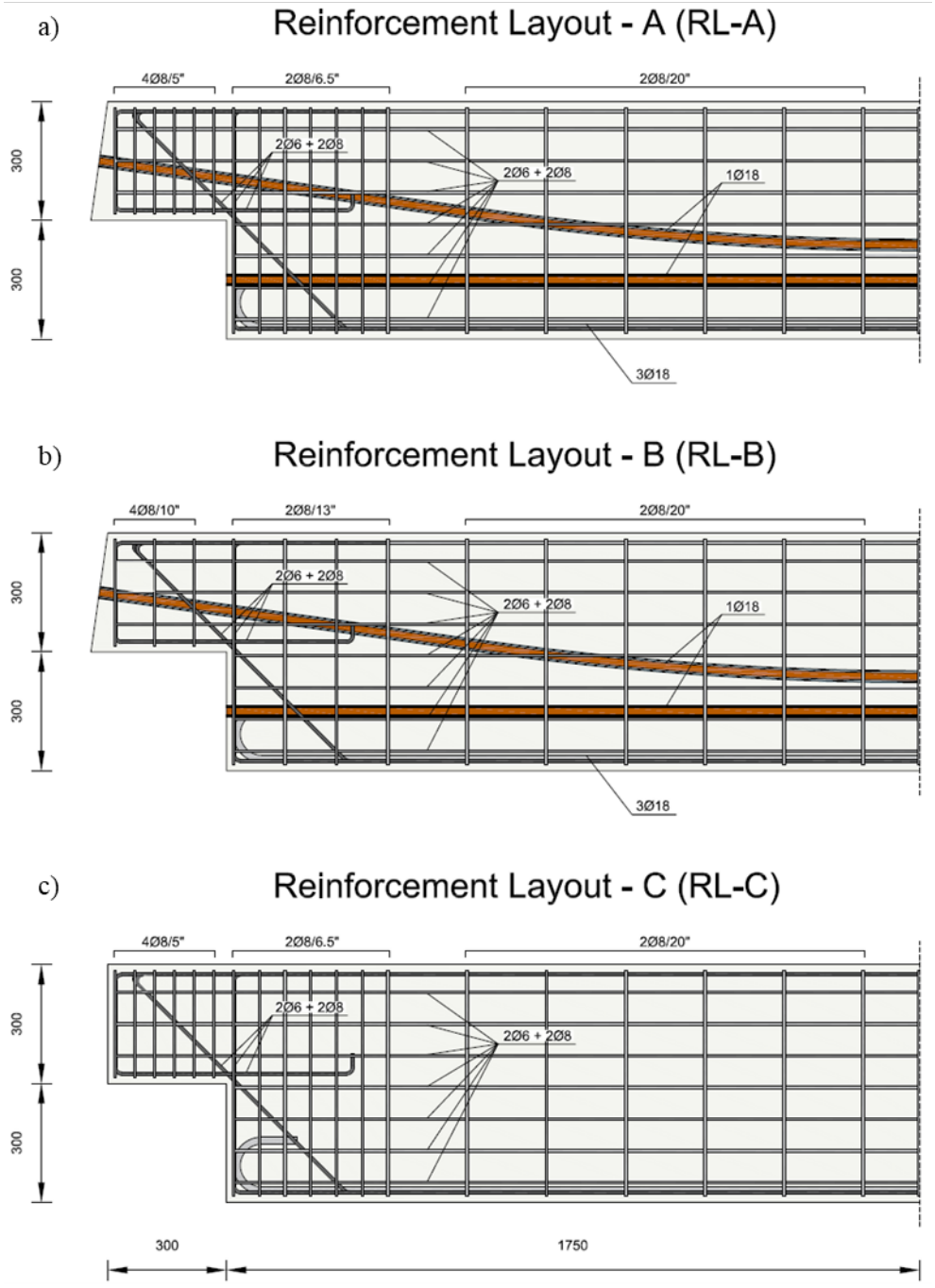

Figure 64. Geometry and different reinforcement layouts of the specimens.

Test configuration

In order to test the half-joints on both sides of the dapped-end beams and avoid unexpected interference during the loading phase on the untested half-joint e.g. crack formation in bending zone or support region, the common procedure is the unsymmetrical three point bending test as reported in several studies [4,23,24,7,8,10–12,19,21]. The set-up of specimens is the statically determinate system constituted of a cylindrical roller bearing installed on the nib lower face, in order to eliminate the horizontal support reaction in the half-joint section, and a pinned steel support installed on the nib and full-depth interface in opposite side of the beam. The total distance between the barycentric axes of the two supports is 3580 mm. The quasi-static load is applied with a hydraulic jack with a capacity of at least 500 kN and spread on the beam by a 30 mm steel plate thick placed 800 mm away from the half-joint support. A summary outline of the test configuration is shown below (Figure 65).

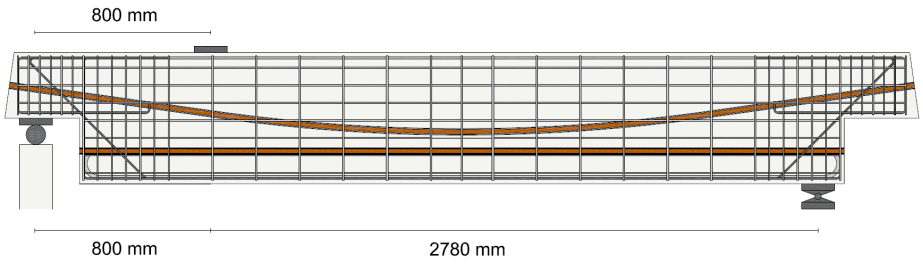

Figure 65. Summary representation of the unsymmetrical three point bending test applied to dapped-end beams.

The reactions of the supports and maximum beam deflection in correspondence of the loading section are recorded, respectively, with two load cells placed under each support and with a linear variable differential

transformer, better known by the acronym LVDT. The internal stress distribution in the D-region is monitored through strain gauges installed on the half-joint reinforcements, stirrups included, and the prestressing bars, for a total of 14 sensors foreach half-joint. All the sensors are pre-wired linear strain gauges with a nominal resistance of 120 Ω and maximum deformation of 50000 μm/m and with a measuring grid which depends on the bar diameter: a measuring grid of 3x1.7 mm is used for bars with 6 or 8 mm diameter and a grid of 10x2.5 mm for the prestressing bars. In detail, two four-legged stirrups of both the nib and the full-depth section on the external legs, the external diagonal and horizontal bars of the nib cross-section and the two prestressing bars, are instrumented, as shown in Figure 66. In order to take into account the temperature effects on strain gauges, the half bridge form of the Wheatstone bridge circuit is used, in which one strain gauge is mounted on the strained material and the other on a passive component of the same material. Foreach specimens, the concrete temperature during the test is monitored with thermocouples in order to record the global specimen temperature. Finally, the piezometric accelerometers are installed in order to track the fundamental frequencies of the beam and their possible variations induced by cracking and fracture phenomena during the quasi-static loading test.

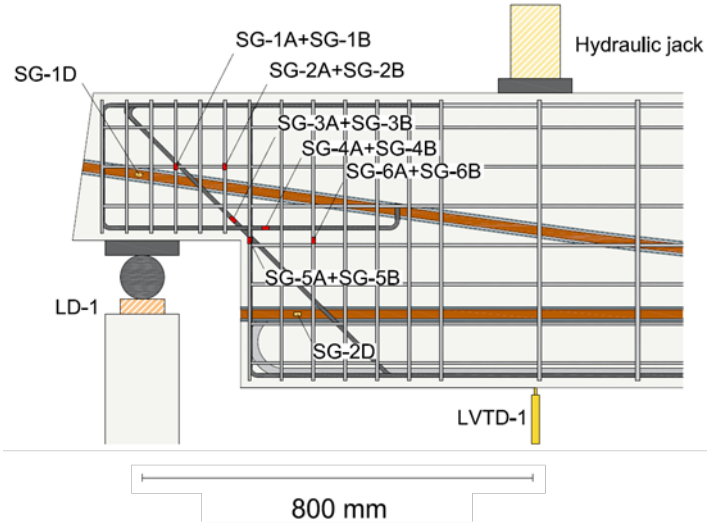

Figure 66. Test configuration and instrumentations installed on the half-joints.

Numerical investigation

The ultimate capacity of the half-joints of the specimens is calculated using strut-and-tie models and more refined finite element models. As mentioned before, the simulations are also necessary for the designs of the tests and the specimens; in fact, the determination of the expected ultimate load reached during the test make it possible to evaluate the required bending reinforcements and shear reinforcements of the beam Bernoulli-region and the well-suited test configuration to prevent the bending and shear failure of the beam instead of the shear failure of the tested half-joint.

This chapter deals with the application to the specimens of strut-and-tie models based on the literature review [4,16,46–48] and on the recent operational document presented by the FABRE consortium concerning the verification of RC half-joints [28] and with a more refined modelling solution adopting solid finite element models developed in ANSYS environment. An in-depth study of the influence of shear span and concrete fracture energy on the collapse mechanism and ultimate capacity of the half-joints will be presented. Finally, the non-linear analyses will be performed to simulate the tests that will be conducted on the specimens and the results will be discussed in detail.

Materials

To design the three point bending test and the reinforcement specimens, the strut-and-tie and fem analyses are performed taking into account the expected strength of materials by adopting, amplifying coefficients as reported by Priestly [49] for the concrete compression strength and for the steel yielding stress and the characteristic upper-bond value for concrete tensile stress as

mention in CEB-fib Model Code 2010 [50], in order to maximize the expected half-joint ultimate capacity and thus achieve an overstrength level against the bending and shear failure mechanisms, which might occur during the tests. The adopted concrete is class C40/50 with a maximum aggregate size compatible with the concrete cover of 25 mm. The reinforcement steel is hot-formed class B450C, according to the Italian code, which is characterized by a characteristic yield strength, f_{yk}, and ultimate strength, f_{tk}, greater than, respectively, 450 MPa and 540 MPa, while the high-tensile steel of the post-tensioning bars is a Y1050 class with yield and ultimate strength of 950 MPa and 1050 MPa. The mechanical properties of concrete, in Table 3, and steel, in Table 4, including those of high-tensile steel taken from the ETA-05/0123. product standard are summarized below.

Table 3. Concrete strength values (Priestly 2007) and tangent modulus of elasticity (fib Model Code 2010) of normal weight concrete.

Concrete grade	**C40/50**
f_{ce} [MPa]	52
$f_{ctk,max}$ [MPa]	4.8
E_c [MPa]	36300

Table 4. Steel strength values of reinforcement bars and mechanical properties of the high tensile steel of the prestressing bars.

Steel grade	**B450C**	**Y1050 ST 950/1050**
f_{ye} [MPa]	495	-
f_{te} [MPa]	594	-
$f_{p0.1}$ [MPa]	-	950
f_{pk} [MPa]	-	1050
E_s [GPa]	210	206

Strut-and-tie models

The preliminary verification of the half-joints are carried out according to the FABRE guidelines [28], which are based on well-known strut-and-tie models from the literature [4,13,36,37]. As reported in the operative instructions, in case of half-joints characterized by both the two resistant mechanisms offered by the vertical and horizontal reinforcements (Figure 67A) and the diagonal reinforcements (Figure 67B), the ultimate shear capacity of the element can be evaluated by summing the partial strut-and-tie model, A and B, or by adopting the complete model C (Figure 67C), which includes both the resistant mechanism. In case of prestressed elements, RL-A and RL-B, the type C strut-and-tie model is modified in order to take into account the post-tensioned contributions.

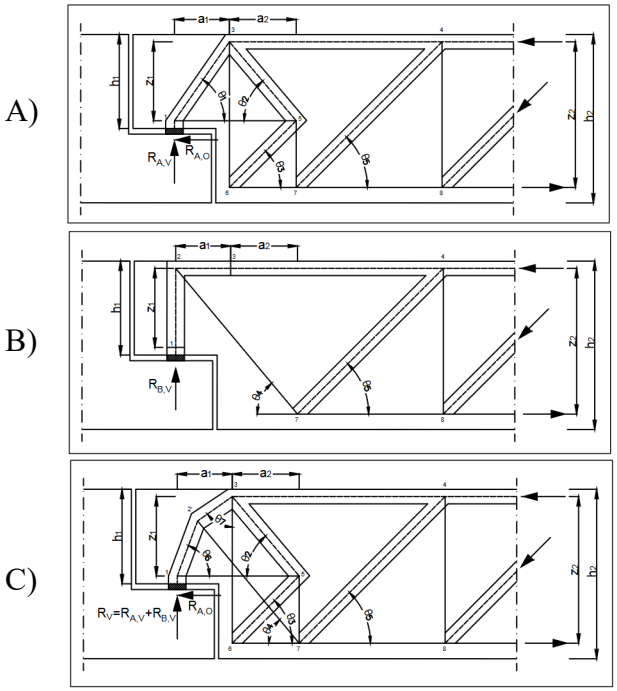

Figure 67. Strut-and-tie model from FABRE technical document.

In all these cases, the solutions obtained based on the strut-and-tie models represent a statically admissible stress field distributions of the disturbed regions and, as well-known, a lower-bound of the ultimate capacity.

Specimens RL-A and RL-B

For the specimens RL-A1, RL-A2, RL-A1D and RL-B, the prestressing forces P_1 and P_2 are inserted in the scheme C and three additional internal nodes are located: the nodes 10 and 11 in correspondence of the post-tensioning anchorages and node 2 which allows to distribute a part of the external force P_1 into the beam section. The external load is shown in the strut-tie model as the constraint reaction R_C which is applied vertically to node 1. The scheme C extends from the nib full-depth interface for a 600 mm length. The strut-and-tie mechanism C is statically indeterminate and require additional assumptions to be solve; indeed, by applying the plastic truss method, the resistant mechanism can be divided in two statically determinate sequential stages.

The first stage is based on the hypothesis that both vertical and diagonal ties, $T_{3\text{-}6}$ (2ϕ8+6ϕ6) and $T_{2'\text{-}7}$ (2ϕ8+2ϕ6), reach the plasticity status. At this point, thanks to the contribution of the prestressing force P1, the tendon $T_{1\text{-}5}$ is compressed and the strut $C_{1\text{-}2'}$ has reached its limiting compressive force imposed by the equilibrium of node 2' (Figure 68). In order to yield the $T_{1\text{-}5}$ tie (2ϕ8+2ϕ6), it is necessary to assume that the mechanism can evolve and the force R_C find a new stress path to grow. The second stage involves the additional strut $C_{1\text{-}4}$ which, by bypassing the saturated stress path represented by $C_{1\text{-}2'}$ and $C_{2'\text{-}3}$, allows the transfer of the constraining reaction up to the Bernoulli region, causing the tension force on the $T_{1\text{-}5}$ tie to increase (Figure

69). At the end of the second stage, it is possible to statically determine the ultimate capacity R_C which corresponds to the plasticity condition of the main half-joint reinforcements.

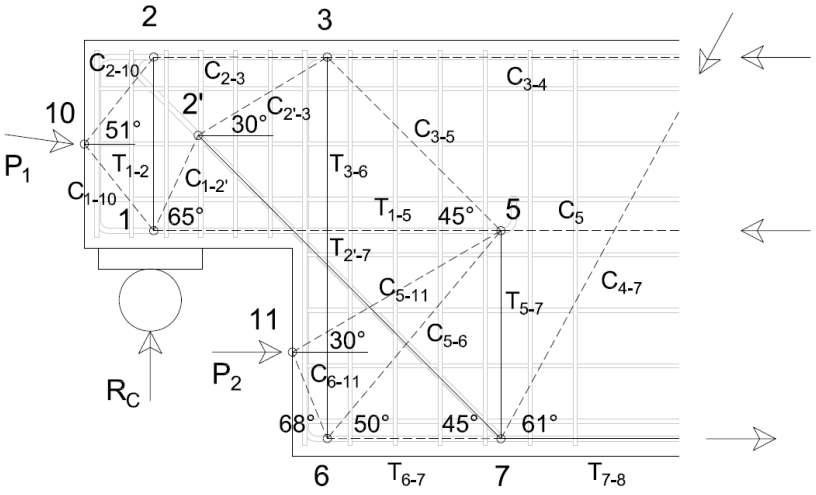

Figure 68. Stage 1 of the stut-and-tie model C.

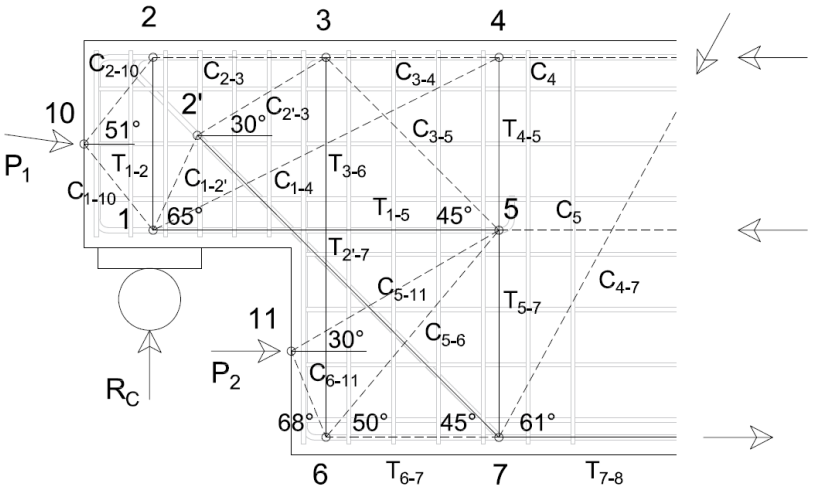

Figure 69. Stage 2 of the stut-and-tie model C.

According to the American standard [51] and the technical literature [39], the inclination of the struts is in the range of 25 to 65 degrees; in the scheme C, only the $C_{5\text{-}11}$ strut shows an angle greater than 65 degrees due to a rapid compressive stress distribution, which is facilitated by the presence of a 30 mm thick anchor plate.

The stage 1 can be solved by writing the translational equilibrium equations of the internal nodes, as shown in Table 5.

Table 5. Equilibrium equations of the model C stage 1.

Node	Equilibrium equations
10	$-C_{2-10}\cos(51^{\circ}) - C_{1-10}\cos(51^{\circ}) - P_2\cos(8^{\circ}) = 0$
	$C_{2-10}\sin(51^{\circ}) - C_{1-10}\sin(51^{\circ}) - P_2\sin(8^{\circ}) = 0$
1	$C_{1-10}\cos(51^{\circ}) - C_{1-2'}\cos(65^{\circ}) + T_{1-5} = 0$
	$-C_{1-10}\sin(51^{\circ}) - C_{1-2'}\sin(65^{\circ}) + T_{1-2} + R_C = 0$
2	$C_{2-10}\cos(51^{\circ}) - C_{2-3} = 0$
	$C_{2-10}\sin(51^{\circ}) - T_{1-2} = 0$
2’	$C_{1-2'}\cos(51^{\circ}) - C_{2'-3}\cos(30^{\circ}) + T_{2'-7}\cos(45^{\circ}) = 0$
	$C_{1-2'}\sin(51^{\circ}) - C_{2'-3}\cos(30^{\circ}) - T_{2'-7}\cos(45^{\circ}) = 0$
3	$C_{2-3} + C_{2'-3}\cos(30^{\circ}) - C_{3-4} - C_{3-5}\cos(45^{\circ})=0$
	$C_{2'-3}\sin(30^{\circ}) + C_{3-5}\sin(45^{\circ}) - T_{3-6}=0$
5	$-T_{1-5} + C_{5-11}\cos(30^{\circ}) + C_{3-5}\cos(45^{\circ}) + C_{5-6}\cos(50^{\circ}) - C_5=0$
	$C_{5-11}\sin(30^{\circ}) - C_{3-5}\sin(45^{\circ}) + C_{5-6}\sin(50^{\circ}) - T_{7-8} = 0$
11	$-C_{6-11}\cos(68^{\circ}) - C_{5-11}\cos(30^{\circ}) + P_1 = 0$
	$C_{6-11}\sin(68^{\circ}) - C_{5-11}\sin(30^{\circ}) = 0$
6	$C_{6-11}\cos(68^{\circ}) + T_{6-7} - C_{5-6}\cos(50^{\circ}) = 0$
	$-C_{6-11}\sin(68^{\circ}) + T_{3-6} - C_{5-6}\sin(50^{\circ}) = 0$
7	$-T_{2'-7}\cos(45^{\circ}) - T_{6-7} + T_{7-8} - C_{4-7}\cos(61^{\circ})$
	$T_{2'-7}\sin(45^{\circ}) + T_{5-7} - C_{4-7}\sin(61^{\circ})$

The stage 2 can be solve by adjusting the equilibrium equations for the nodes 1 and 5 and by introducing the new translational equations of node 4, as shown in Table 6.

Table 6. Equilibrium equations of the model C stage 2.

Node	Equilibrium equations
1	$C_{1-10}\cos(51^{\circ}) - C_{1-2'}\cos(65^{\circ}) + T_{1-5} - C_{1-4}\cos(27^{\circ}) = 0$
	$-C_{1-10}\sin(51^{\circ}) - C_{1-2'}\sin(65^{\circ}) + T_{1-2} + R_C - C_{1-4}\sin(27^{\circ}) = 0$
5	$-T_{1-5} + C_{5-11}\cos(30^{\circ}) + C_{3-5}\cos(45^{\circ}) + C_{5-6}\cos(50^{\circ}) - C_5 = 0$
	$C_{5-11}\sin(30^{\circ}) - C_{3-5}\sin(45^{\circ}) + C_{5-6}\sin(50^{\circ}) - T_{8-7} + T_{4-5} = 0$
4	$C_{3-4} - C_4 + C_{1-4}\cos(27^{\circ}) = 0$
	$C_{1-4}\sin(27^{\circ}) - T_{4-5} = 0$

Below the solutions of the equilibrium equations and the internal distribution of forces for the first and second stage of the strut-and-tie models are reported for the specimen RL-A1 (Figure 70-Figure 71), RL-A2 (Figure 72-Figure 73), RL-B1 (Figure 74-Figure 75) and RL-A1D (Figure 76-Figure 77).

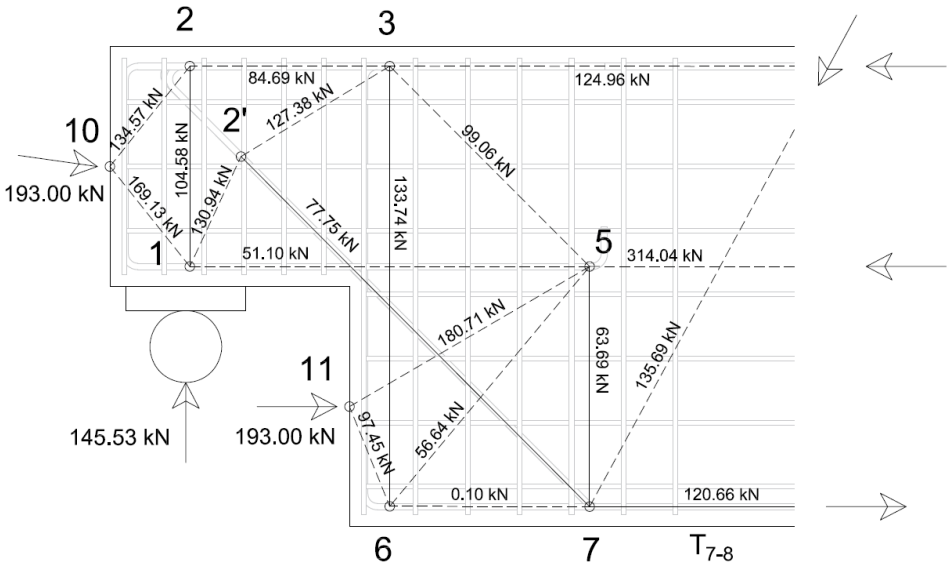

Figure 70. Internal forces distribution in struts and ties for the RL-A1 stage 1.

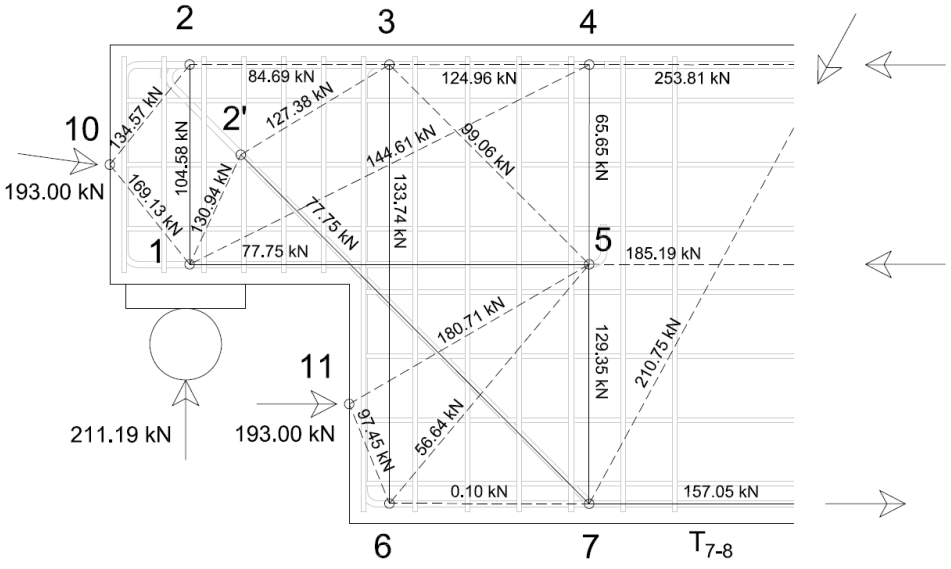

Figure 71. Internal forces distribution in struts and ties for the RL-A1 stage 2.

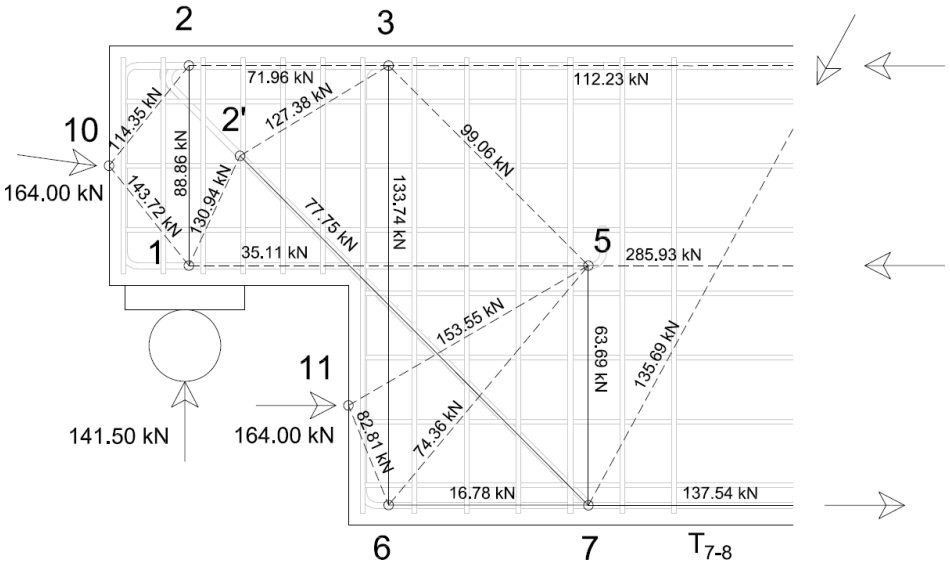

Figure 72. Internal forces distribution in struts and ties for the RL-A2 stage 1.

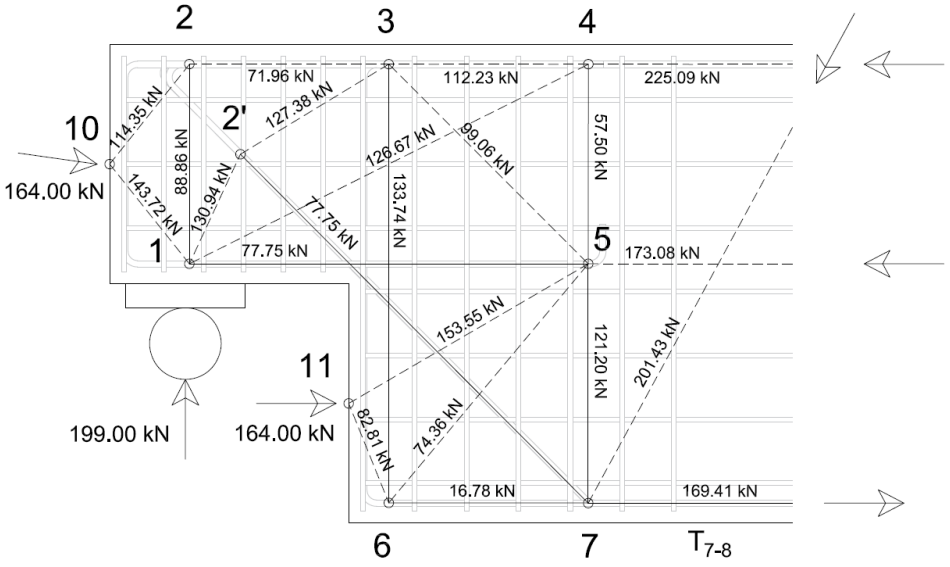

Figure 73. Internal forces distribution in struts and ties for the RL-A2 stage 2.

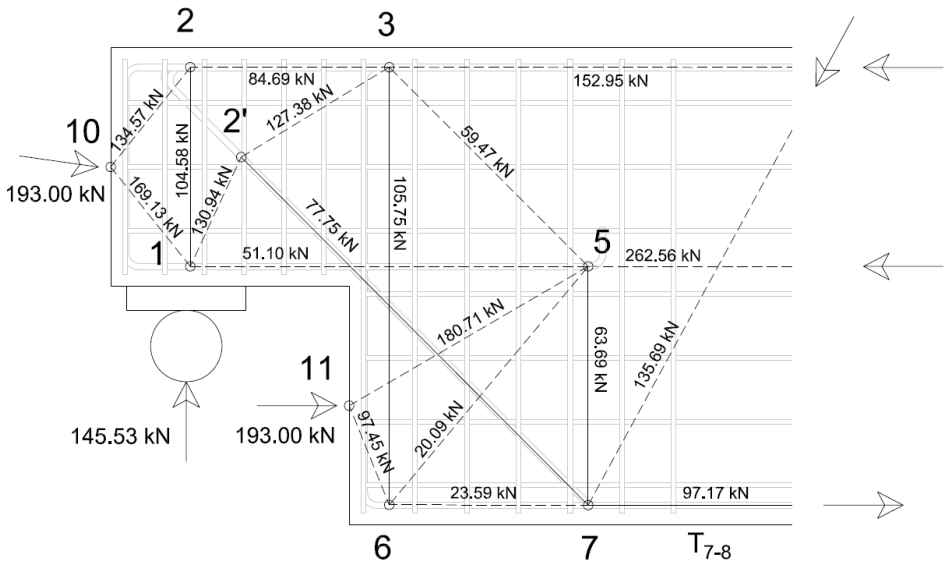

Figure 74. Internal forces distribution in struts and ties for the RL-B1 stage 1.

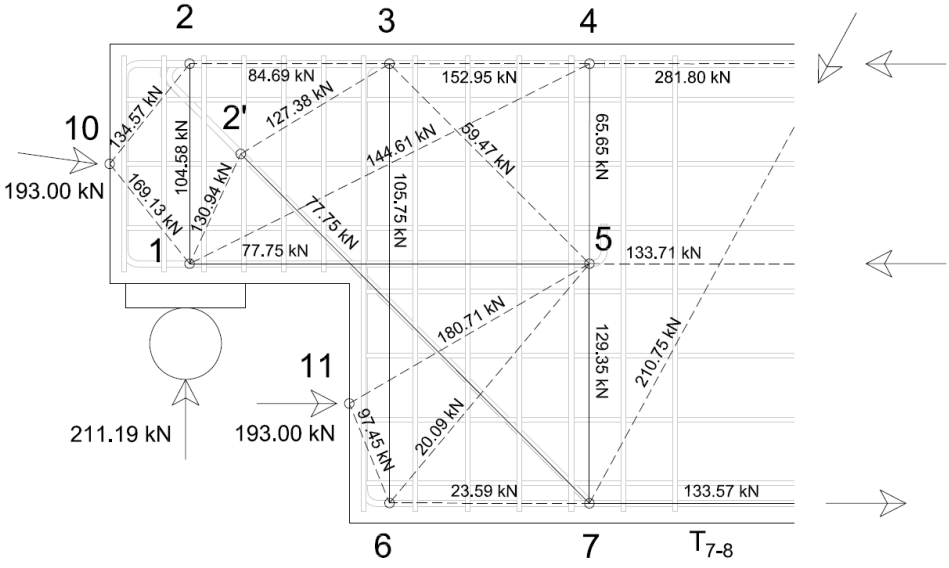

Figure 75. Internal forces distribution in struts and ties for the RL-B1 stage 2.

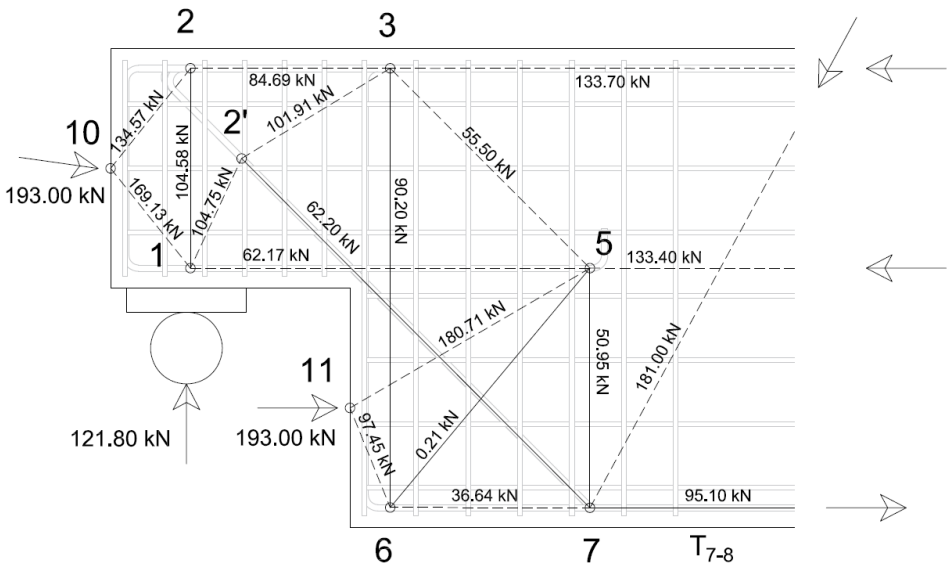

Figure 76. Internal forces distribution in struts and ties for the RL-A1D stage 1.

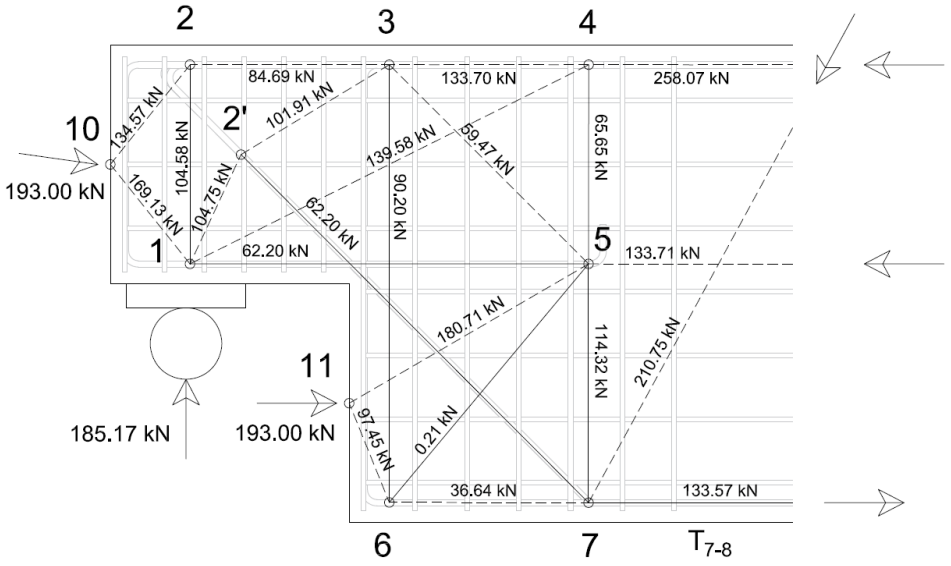

Figure 77. Internal forces distribution in struts and ties for the RL-A1D stage 2.

Specimen RL-C

The resistant mechanism of the RL-C reinforcement layout is evaluated with the combine strut-and-tie models, A and B, and with the scheme C adopted for the RL-A and RL-B, opportunely modified to exclude the prestressing contribution.

Starting from the combine strut-and-tie model, the type A is based on the resisting mechanism provided by two main ties, $T_{1\text{-}5}$ and $T_{3\text{-}6}$, which are composed, respectively, of horizontal reinforcements (2ϕ8+2ϕ6) and coupled bent reinforcements and two two-legged stirrups (2ϕ8+6ϕ6); the width of the compressed struts, $C_{5\text{-}6}$ and $C_{4\text{-}7}$, is sufficient to involve at least two orders of stirrups in the resisting mechanism (Figure 78).

The scheme A can be solved by applying the translational static equilibrium of the internal nodes and the rotational equilibrium in node 7. The equations are summarized in Table 7.

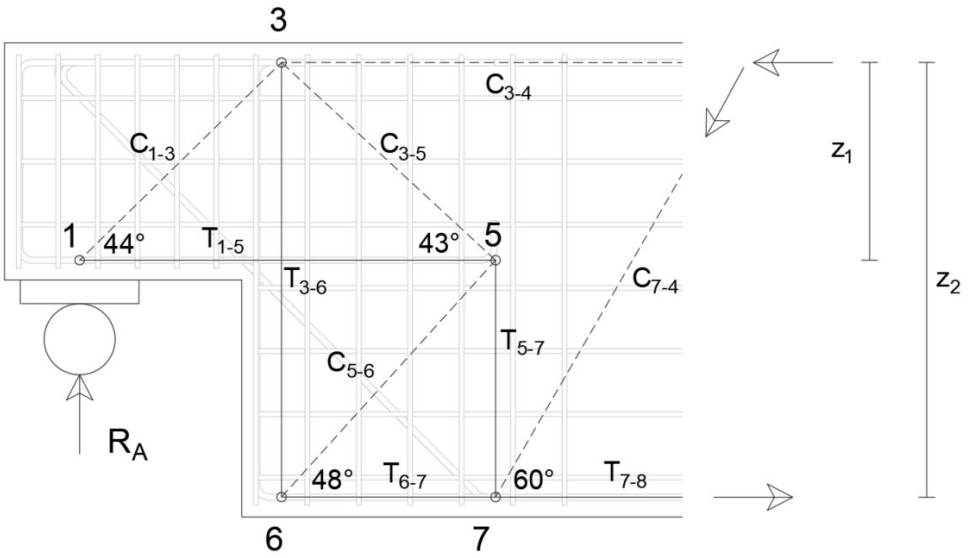

Figure 78. Strut and tie model: type A resisting mechanism.

Table 7. Equilibrium equations the strut-and-tie model A.

Node	Equilibrium equations
1	$R_A - C_{1-3}\sin 44^\circ = 0$
	$T_{1-5} - C_{1-3}\cos 44^\circ = 0$
3	$C_{1-3}\cos 44 - C_{3-5}\cos(43^\circ) - C_{3-4} = 0$
	$C_{1-3}\sin 44^\circ + C_{3-5}\sin(43^\circ) - T_{3-6} = 0$
5	$C_{5-6}\sin 48^\circ - T_{5-7} - C_{3-5}\sin(43^\circ) = 0$
	$C_{5-6}\cos 48^\circ - T_{3-6} + C_{3-5}\cos(43^\circ) = 0$
6	$T_{3-6} - C_{5-6}\sin 48^\circ = 0$
	$T_{6-7} - C_{5-6}\cos 48^\circ = 0$
7	$T_{7-8} - T_{8-9} - C_{7-4}\cos(60^\circ) = 0$
	$T_{5-7} - C_{7-4}\sin(60^\circ) = 0$
	$R_A(z_1\cot(44^\circ) + z_1\cot(43^\circ)) - C_{3-4}z_2 = 0$

The solutions of linear system allows to calculate the internal forces of the strut-and-tie model and to determine the maximum capacity of the mechanism

A, which is calculated as the maximum support reaction R_A that causes the yield of the T_{1-5} tie, which reaches the yielding force of 77.75 kN for a shear force of 75.09 kN. For the sake of completeness, all the forces of the strut-and-tie model are reported in Figure 79.

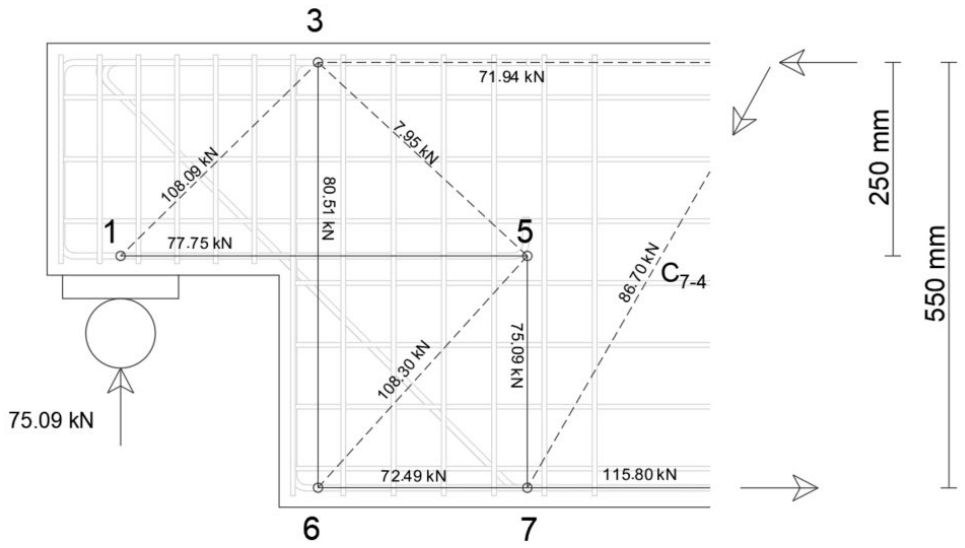

Figure 79. Internal forces distribution in struts and ties for the scheme A.

The resistant mechanism B is based on the resistant contribution of the diagonal tie T_{1-5}, composed of two 8 mm diameter and two 6 mm diameter bars (2ϕ8+2ϕ6). Also in this case, the strut-and-tie model can be solved by imposing the static translation equilibrium of the internal nodes, as reported in Table 8.

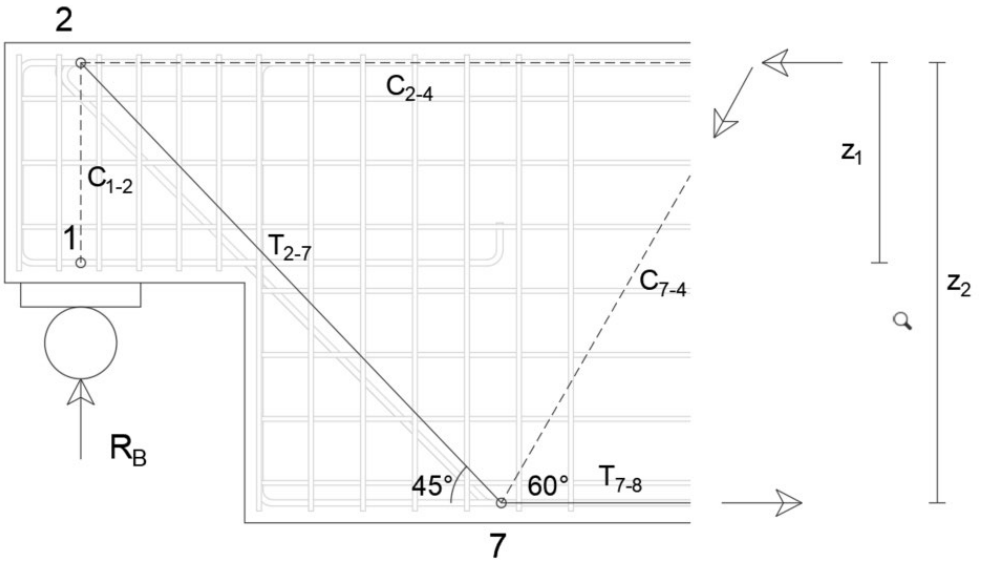

Figure 80. Strut and tie model: type B resisting mechanism.

Table 8. Equilibrium equations the strut-and-tie model B.

Node	Equilibrium equations
1	$R_B - C_{1-2} = 0$
2	$C_{1-2} - T_{2-7}\sin(45^\circ) = 0$
	$T_{2-7}\cos(45^\circ) - C_{2-4} = 0$
7	$T_{7-8} - T_{2-7}\cos(45^\circ) - C_{4-7}\cos(60^\circ) = 0$
	$T_{2-7}\sin(45^\circ) - C_{4-7}\sin(60^\circ) = 0$

By solving the linear system reported above, the maximum capacity of the mechanism B is 54.98 kN, which causes the yielding of the $T_{2\text{-}7}$ tie. All the forces of the strut-and-tie model are reported in Figure 81.

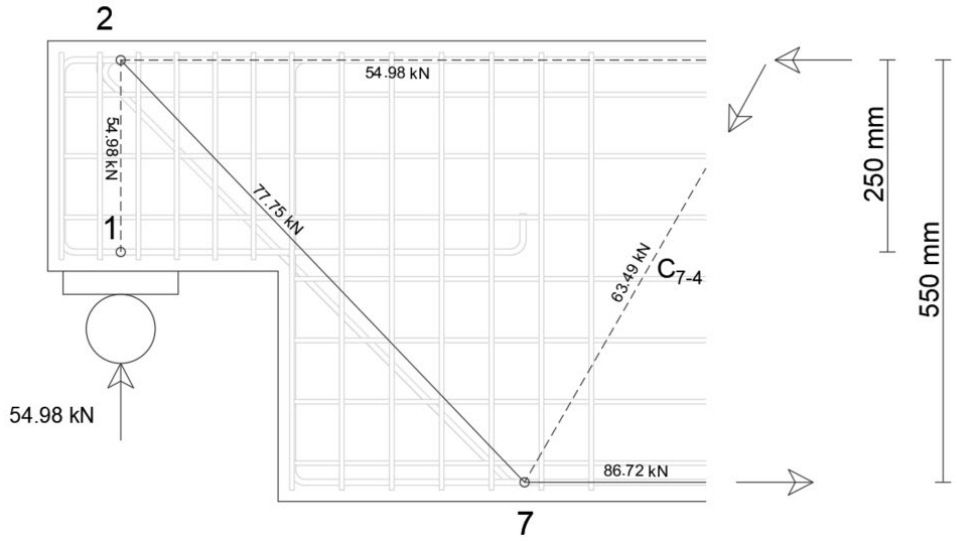

Figure 81. Internal forces distribution in struts and ties for the scheme B.

After the determination of the two resistant mechanisms of the RL-C half-joint, the ultimate capacity can be expressed as the sum of the two shear capacity, R_A and R_B, for a total shear resistant of 130.07 kN. A similar result of 118.67 kN is obtained by adopting the scheme C with zero prestressing forces P_1 and P_2. The internal forces of the combined strut-and-tie model are showed in Figure 82.

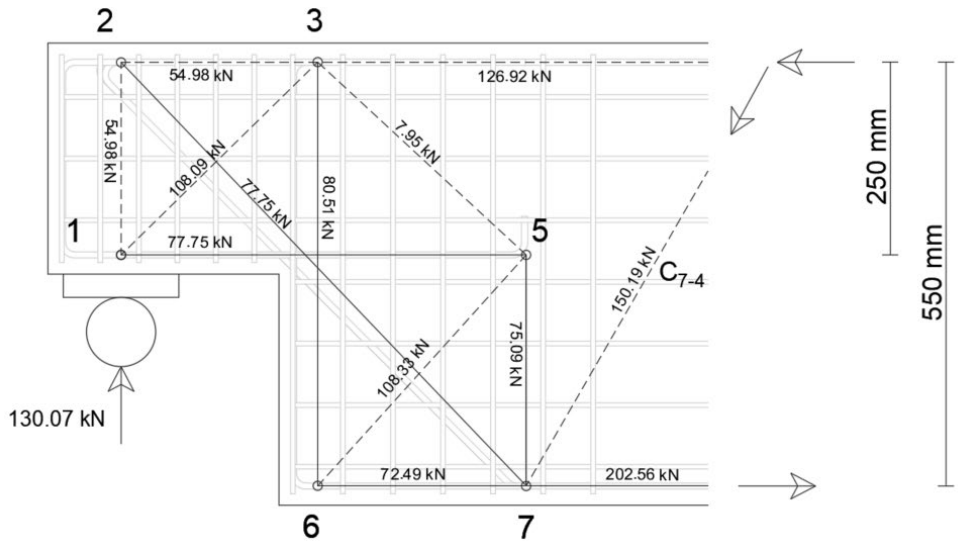

Figure 82. Force distribution in the disturbed region of the combined strut-and-tie model (A+B).

The support reactions R_1 and R_2 are directly dependent on the isostatic beam scheme, which can be represented as a simply supported beam of total length of 3580 mm with a concentrated load, F_{ext}, at 800 mm distance from the roller support, as shown in Figure 83. Based on the expected ultimate capacity of the half-joints calculated with the strut-and-tie models, the minimum concentrated loads to be applied for the specimens failure are summarized in Table 9.

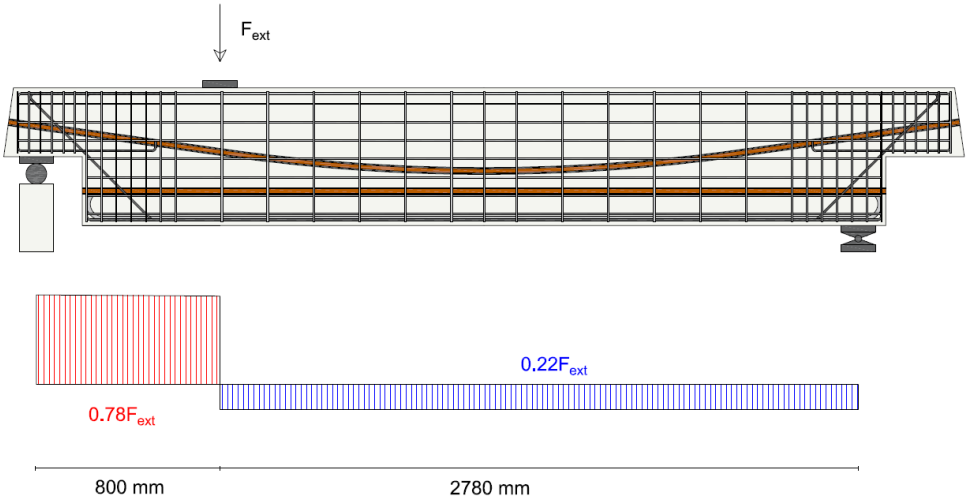

Figure 83. Shear diagram of the isostatic beam.

Table 9. Support reactions and expected failure loads.

Specimen	F_{ext}	R_1	R_2
RL-A1 [kN]	270.76	211.19	59.57
RL-A2 [kN]	255.13	199.00	56.13
RL-A3 [kN]	167.50	130.07	37.43
RL-B1 [kN]	270.76	211.19	59.57
RL-A1D [kN]	237.40	185.17	52.23
RL-C [kN]	167.50	130.07	37.43

Finite Element Analysis

The ultimate capacity of the specimens are calculated by performing non-linear analyses on refined solid models developed in ANSYS ambient [52], which are capable of giving additional information about the failure mechanism. The models are widely described below, starting with the definition of the elements and materials and ending with the modelling of reinforcements and prestressing system. The influence on the ultimate capacity and failure mechanism of the two parameters, shear span and fracture energy of concrete, is also investigated.

For simulating the behavior of the bonded aggregates as concrete, a nonlinear geomechanics model is adopted. The concrete constitutive law is the Menetrey-William model [53] based on the William-Warneke yield surface [54], which shares some characteristics of both Mohr-Coulomb and Drucker Prager [55] failure criterions and has less difficulty finding surface stress solution with respect to the others. The yield function in compression shows an power hardening law for a plastic strain $\kappa<\kappa_{cm}$ and an exponential softening function for κ in the range $\kappa_{cm}<\kappa<\kappa_{cu}$, as reported in Figure 84a. The yield function in tension (Figure 84b) is given by an exponential softening function, where the volumetric energy lost during the softening is proportional to the tension fracture energy of the mode I area; more details are available in the ANSYS Mechanical User's Guide [52].

The model parameters values used to simulate the C40/50 concrete, in accordance to the fib 2010 Model Code [50] are summarized in Table 10.

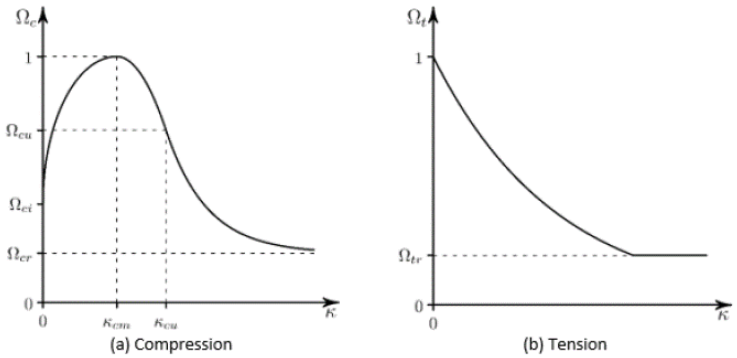

Figure 84. The yield function of Menetrey-William model in compression (a) and in tension (b).

Table 10. Menetrey-William material properties.

Parameter	Value
Uniaxial compressive strength, R_t [MPa]	52
Uniaxial tensile strength, R_t [MPa]	3.5
Biaxial compressive strength, R_b [MPa]	67.6
Dilatancy angle, ψ [°]	9
Plastic strain at uniaxial compressive strength, κ_{cm} [-]	0.0024
Plastic strain at transition from power law to exponential softening, κ_{cu} [-]	0.0035
Relative stress at start of nonlinear hardening, Ω_{ci} [-]	0.4
Residual relative stress at κ_{cu}, Ω_{cu} [-]	0.5
Residual compressive relative stress, Ω_{cr} [-]	0.05
Mode I area-specific fracture energy, G_{ft} [N/m]	146.5
Residual tensile relative stress, Ω_{tr} [-]	0.05

For steel elements, two different constitutive laws are defined, both with a bilinear isotropic hardening function; one for the reinforcements and another one for the high-tensile steel bars.

The 3D finite element chosen for the concrete solid elements is the CPT215, a three-dimensional hexahedral element characterized by having eight coupled nodes with four degrees of freedom each (Figure 85). The element is also suitable for prismatic and tetrahedral elements, but the last option is not recommended. To simulate the extra reinforcing provide by the reinforcements embedded in concrete, the discrete element REINF264 available in the ANSYS Library is adopted (Figure 85).

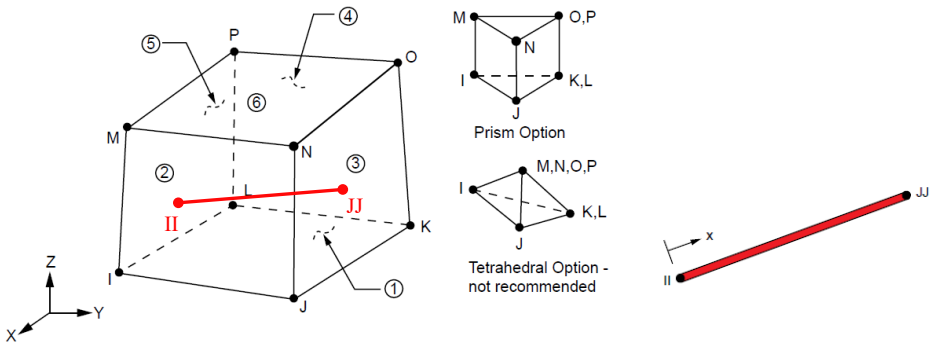

Figure 85. CPT215: 3D element with 8 coupled nodes from ANSYS Mechanical Library.

The REIFN264 element does not allow the direct application of loads on the fibres, therefore, the bars of the post-tensioning system are modelled using BEAM188 elements based on the classic Timoshenko beam theory. An infinitely rigid element is inserted in the beam mid section to prevent vertical displacements of the curved bar, by assuming that the contact between bar and metallic duct during tensioning takes place there (Figure 86).

Finally, the solid element SOLID185 is used to model the steel diffusion plates located in the supports and the hydraulic jack region.

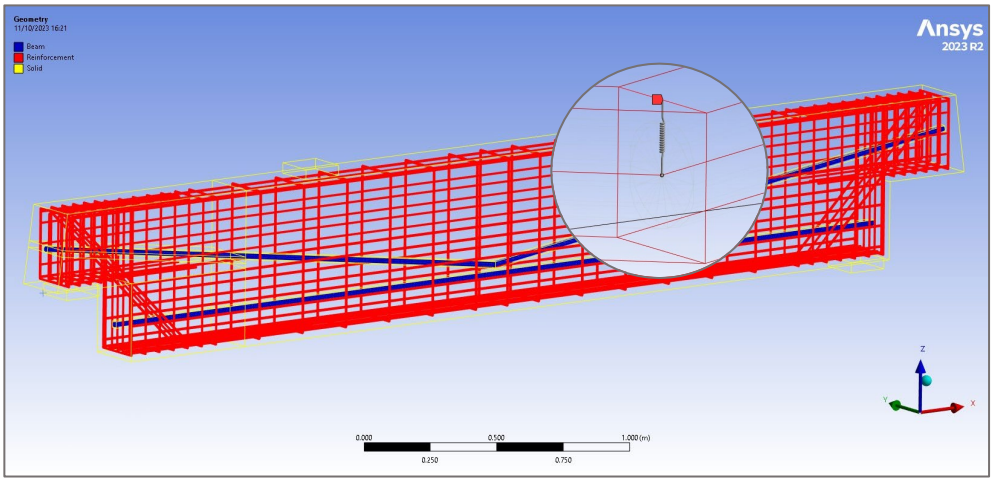

Figure 86.View finite element categories: solid in yellow, beam elements in blue and reinforcements (truss) in red.

The connections between the finite elements are managed using connections with the multi-points constraint formulation; in detail, a bonded contact is inserted to join the faces of the beam plate interfaces and the tensioning bar edges with the internal faces of the metal duct. In order to obtain a realistic tensioning load distribution, the anchor plates of the post-tensioning system are simulated with a body-body joint connection, which links the end node of the beam element with the external concrete face; by adopting a pinball region radius equals to half plate width, a real distribution of MPC constraint is obtained (Figure 87). The constraints are body-ground joint connections, which release the translation along the global x-axis and the rotations in the y-axis in the roller support, while release only y-axis rotations in the hinge support.

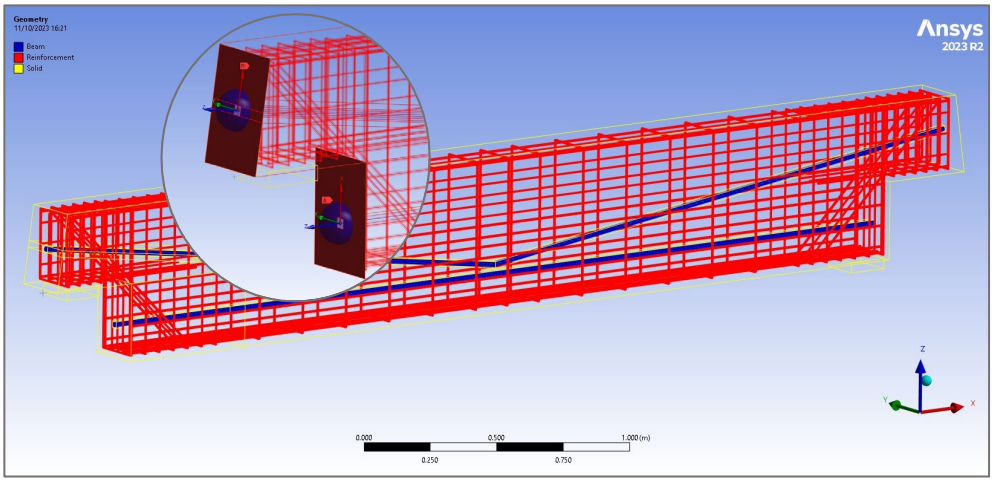

Figure 87. Multi-point constraint application to the post-tensioning system anchorages.

In order to use the CPT215 with three-dimensional hexahedral element, the linear meshing order is imposed and the hex dominant method is selected. The sizing of the half-joint region is approximately 40 mm, while a 50 mm sizing is chosen for the remaining part of the model. In total, 16541 nodes and 13342 elements are obtained, as shown in (Figure 88).

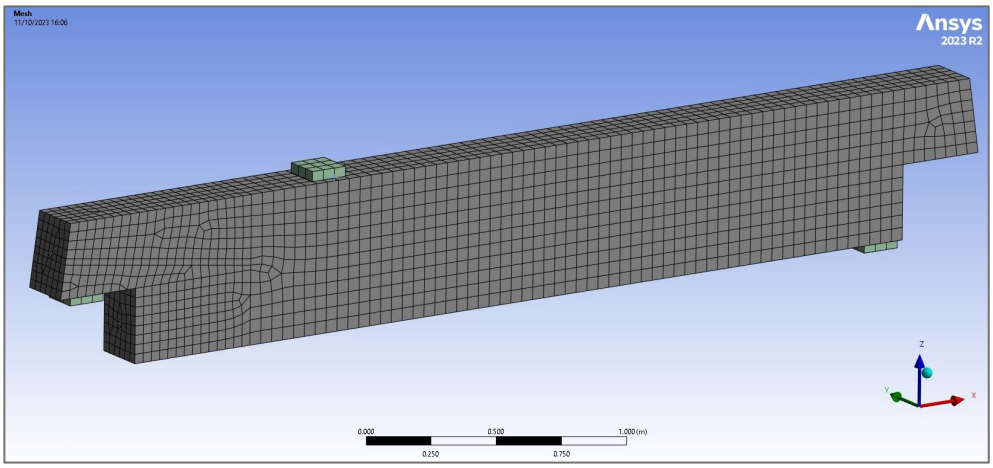

Figure 88. Mesh view of the model RL-A(1-2-1D) and RL-B1.

Nonlinear analyses are performed with admissible large deflections and requiring a minimum of 50 sub-steps and a maximum of 10,000 iterations for the final load application step. The analysis of the pre-stressed beams is composed of 3 main steps:

1) **Self-weight application**: in this phase, the contact between the high-tensile bars and the metal duct faces is deactivated, using the contact control command to simulate the absence of duct injection.
2) **Prestressing application**: the prestressing force is applied to the bars by the bolt pretension command. Also in this phase, the beam-solid contact is still deactivated.
3) **Application of external load**: in the final step, before beginning load application, the contact between bars and beams is activated and the bars tension is put in locked status. The external load is applied until the model fails to converge.

On the contrary, the sample without prestressing involves only the phases of self-weight and external load application. In the case of sample RL-B, to reduce the quantity of stirrups on the half-joint by 50%, the 50% of the stirrups elements are removed. The sample RL-AD, characterized by corrosion phenomena leading to 20% loss of section, is modeled by removing the first stirrup located in the full-depth nib interface and assigning a reduced cross section to the horizontal, vertical and diagonal bars affected by corrosion phenomena.

At this stage, to evaluate the maximum capacity of the half-joints, the precompression losses due to steel relaxation, and to shrinkage and creep of the concrete are neglected.Model validation

The modelling technique is validated by performing a simple three-point symmetrical bending test and comparing the numerical result with the expected bending resistance based on the cross-section properties. By analyzing the mid-span section of the beam, at the ultimate limit state, the level of prestressing does not affect the ultimate capacity of the cross section since both the bars reach the yield strain. The ultimate bending moment, obtained using the VCA-SLU software, is 495 kNm, as shown in Figure 89.

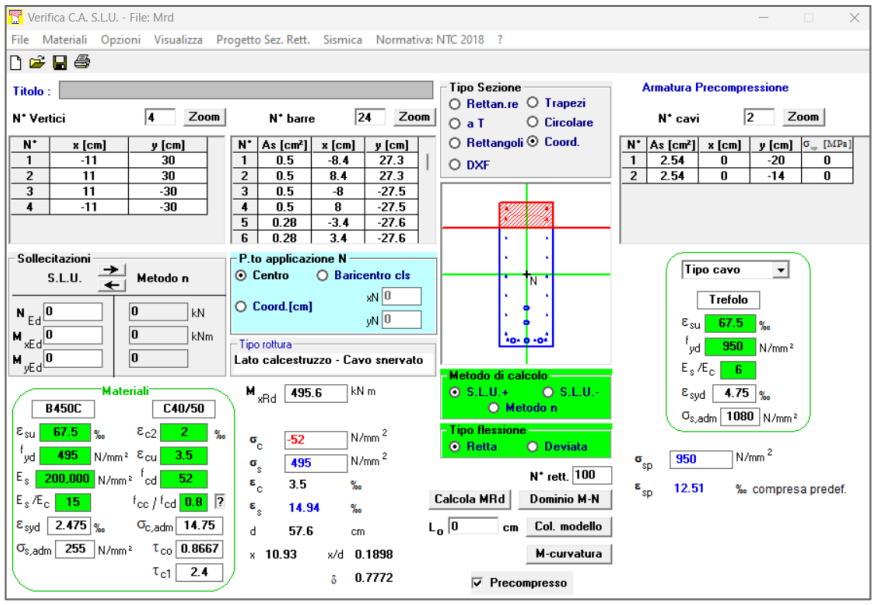

Figure 89. Cross section properties in mid-span section of the specimens calculated by VCA-SLU software.

The results obtained from the FE model are shown in the Figure 90, in terms of equivalent stresses (Von-Mises) acting on the reinforcement bars and in terms of normal stresses in the X-axis direction for the concrete elements, where it can be seen that the neutral axis depth reaches 15 cm, compared to 10.93 cm of the VCA-SLU calculation.

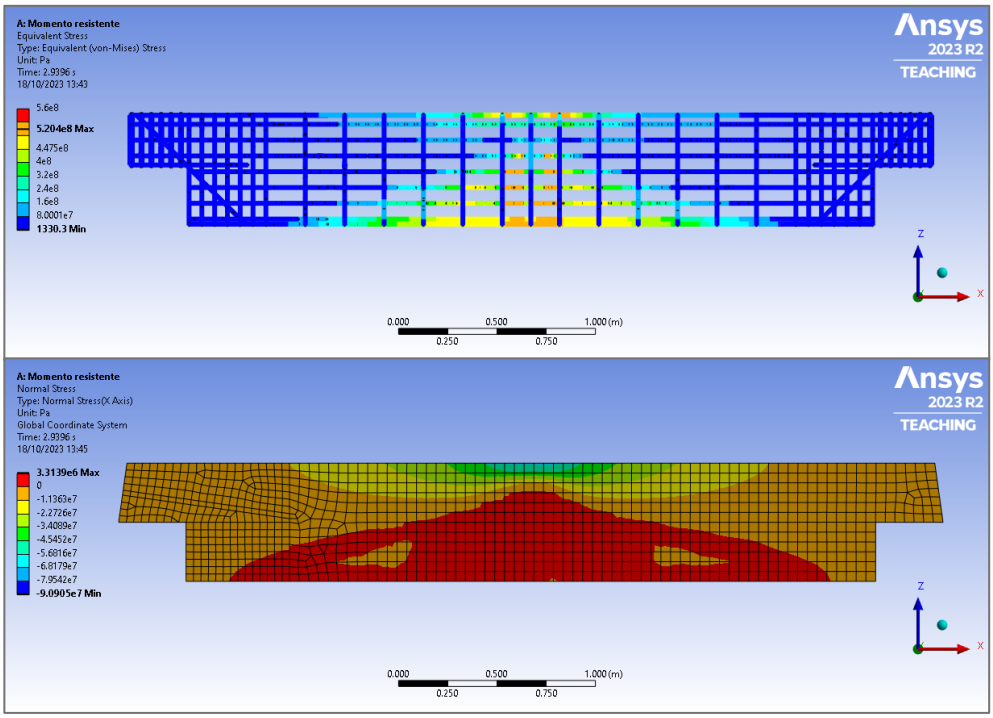

Figure 90. Von-Mises stress distribution on the reinforcements (above) and normal stress in X direction in the concrete material (below).

The FE model, as shown in Figure 91, achieves an ultimate resistant moment of 570 kNm, thanks to the positive effect of concrete confining offered by the reinforcements.

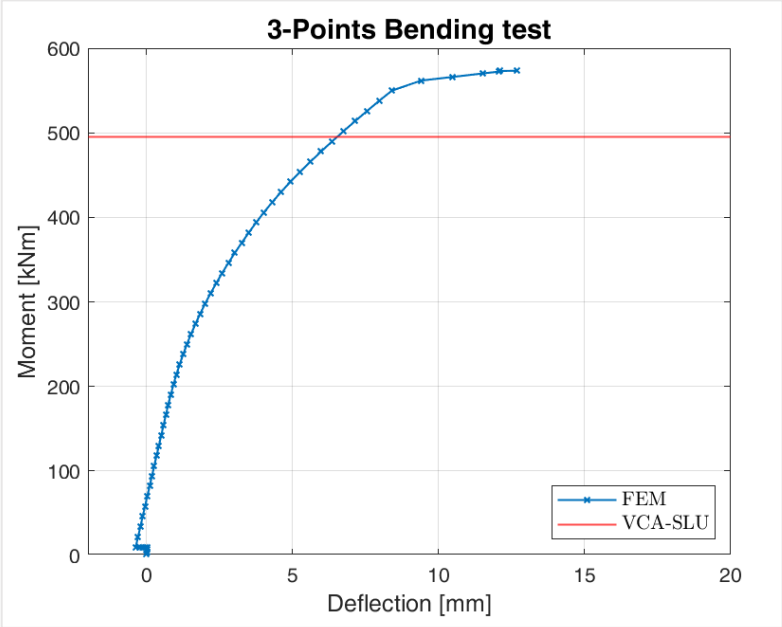

Figure 91. Bending test simulation.

Another validation of the model was done by adopting the experimental data published by Desnerck et al. [13]. The selected specimen is the NS-REF, which consists of a dapped-end beam with a 260 mm depth nib of 375 mm height and a full-depth section of 700 x 400 mm, with a total length of 2.8 m. The half-joint reinforcements consist of both diagonal (4ϕ12) and vertical (2ϕ10) and horizontal (4ϕ12) bars. The geometry and dimensions of the reinforcement are summarized in Figure 92 below.

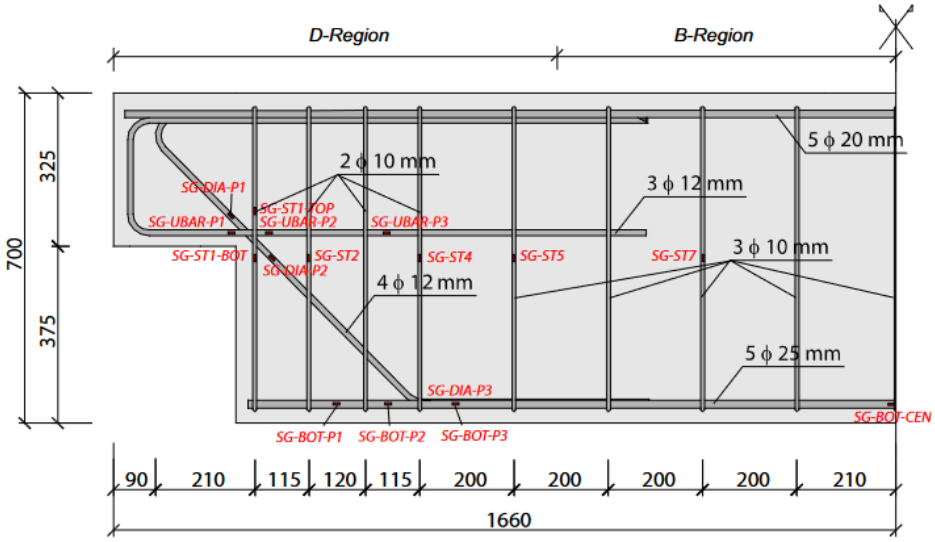

Figure 92. Geometry and dimensions of the NS-REF specimens [13].

The ultimate capacity of the dapped-end beam was tested by means of a symmetrical three-point test with the external load applied by a hydraulic jack positioned in the mid-span section of the beam (Figure 93).

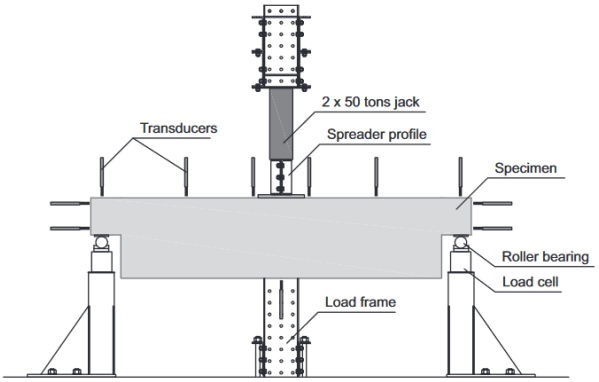

Figure 93. Test configuration for the NS-REF specimen [13].

The material characteristics adopted in the model are those stated by the authors and are summarized in Table 11 below.

Table 11. Properties of materials for the NS-REF model.

	Parameter	Value
CONCRETE	Young's Modulus, E_c [GPa]	36
	Poisson's Ratio, v_c [-]	0.2
	Uniaxial compressive strength, R_t [MPa]	52
	Uniaxial tensile strength, R_t [MPa]	3.5
	Biaxial compressive strength, R_b [MPa]	67.6
	Dilatancy angle, ψ [°]	9
	Plastic strain at uniaxial compressive strength, κ_{cm} [-]	0.0024
	Plastic strain at transition from power law to exponential softening, κ_{cu} [-]	0.0035
	Relative stress at start of nonlinear hardening, Ω_{ci} [-]	0.4
	Residual relative stress at κ_{cu}, Ω_{cu} [-]	0.5
	Residual compressive relative stress, Ω_{cr} [-]	0.05
	Mode I area-specific fracture energy, G_{ft} [N/m]	146.5
	Residual tensile relative stress, Ω_{tr} [-]	0.05
STEEL	Young's Modulus, E_s [GPa]	200
	Poisson's Ratio, v_s [-]	0.3
	Yield Strength, F_y [MPa]	500
	Tangent Modulus [MPa]	1450

The FE model of the NS-REF specimen is obtain by adopting the previously described modelling techniques. After the meshing procedure, the model dimensions are constitute of 14137 nodes and 10019 elements and the finale result is shown in Figure 94.

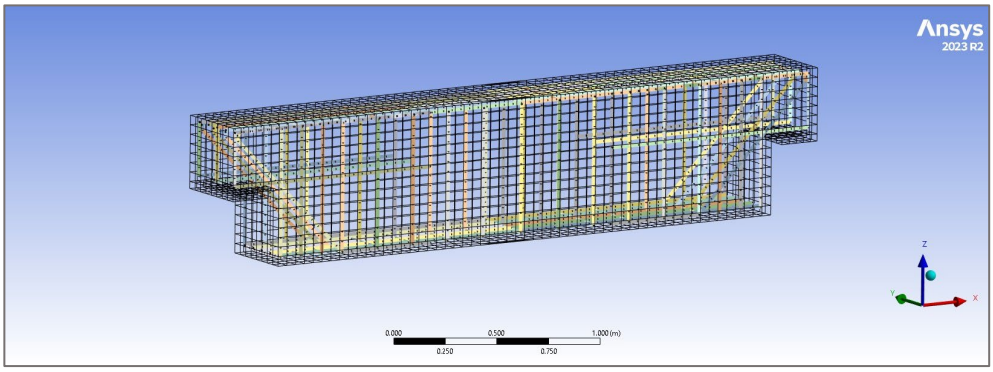

Figure 94. Mesh view of the NS-REF model.

In order to calibrate the model with the experimental data, analyses were performed by varying the fracture energy parameter, G_F, of the Menetrey-William concrete model. The starting values are calculated according to the formulations reported in the fib model codes [56,50]. For the NS-REF specimen made by C40 concrete class, the fracture energy is equal to 70 N/m and 146.5 N/m, respectively, according to the 1990 and 2010 model codes.

Table 12. Fracture energy of normal weight concrete from fib Model Code 1990 and 2010.

Parameter	**Model Code 1990**	**Model Code 2010**
G_F [MPa]	$G_{Fo}\cdot(f_{cm}/f_{cmo})^{0.18}$	$73\cdot f_{cm}^{0.18}$

The capacity curve in terms of load and deflection, measured in mid-span section matches, matches with a good approximation the experimental data by adopting a fracture energy value of 20 N/m, which is much lower than the minimum value obtained from the formulations in the codes (Figure 95).

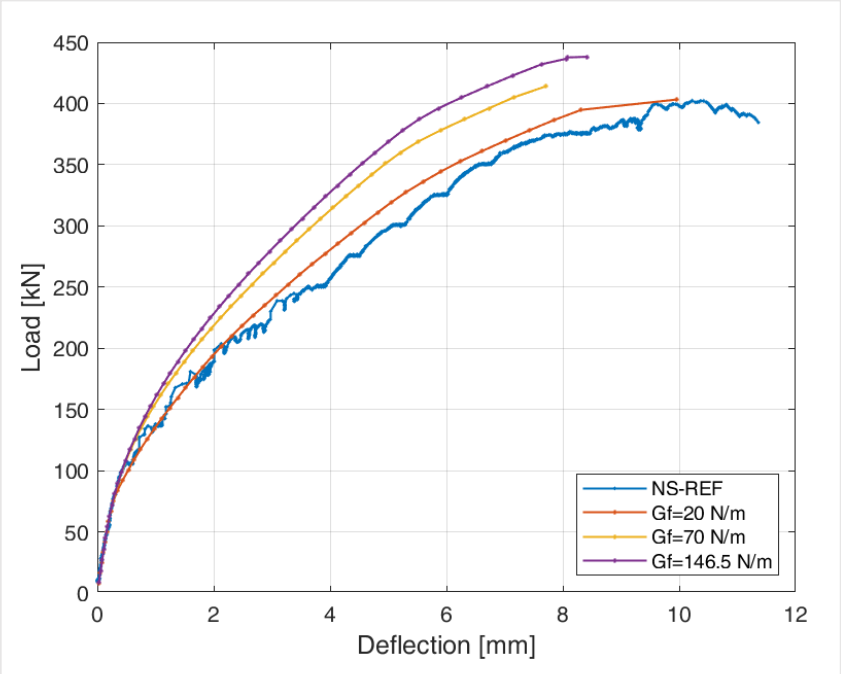

Figure 95. Load-deflection curve of the NS-REF FE model versus the experimental data.

In the last step of the analysis before the model fails to converge, the reinforcement of the saddle, in particular the horizontal, vertical and diagonal reinforcement, register stresses exceeding the yield threshold of 500 MPa (in red in Figure 96a). The accumulation of plastic deformations on the concrete (Figure 96b) shows widespread bending cracks in the central part of the beam, where the bending moment is greatest, and a large cracked area in the inner corner of the nibs, where the plasticity of the reinforcements is concentrated.

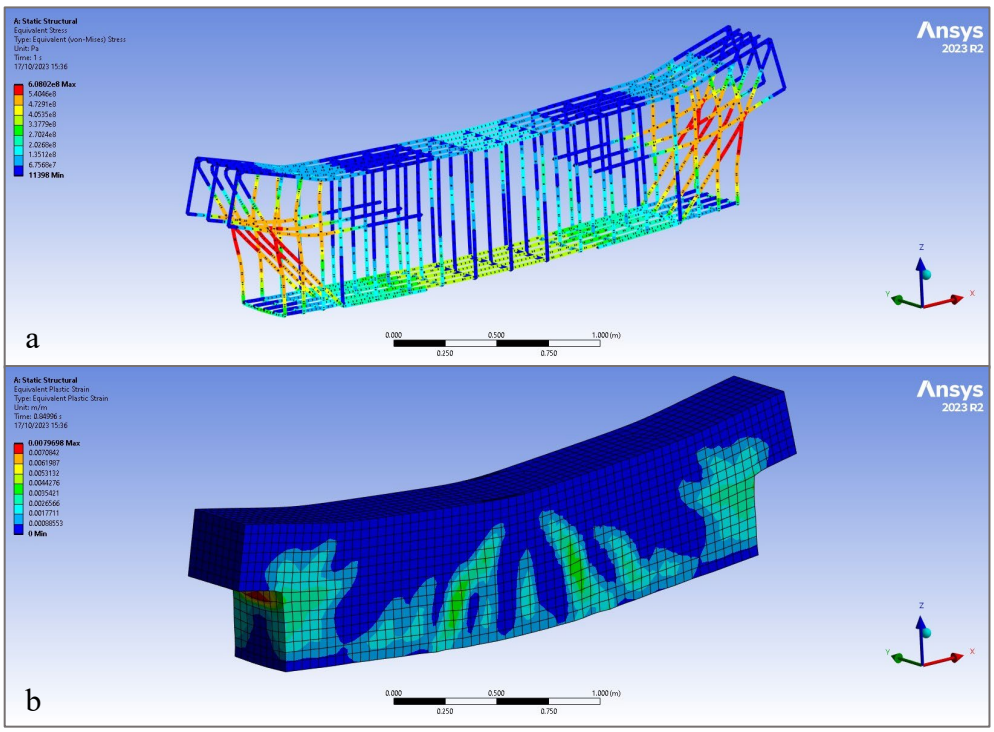

Figure 96. Equivalent Von-Mises stresses on steel reinforcements (a) and equivalent plastic strain on concrete (b).

Influence of shear span

To investigate the influence of shear span on the ultimate capacity of the half-joints, a numerical investigation proposed assuming three different load positions: 600 mm, where the shear span-to-full depth ratio is equal to 1, 800 mm and 1100 mm, which correspond to a shear span-to-full depth ratio, respectively, of 1.3 and 1.8 (Figure 97).

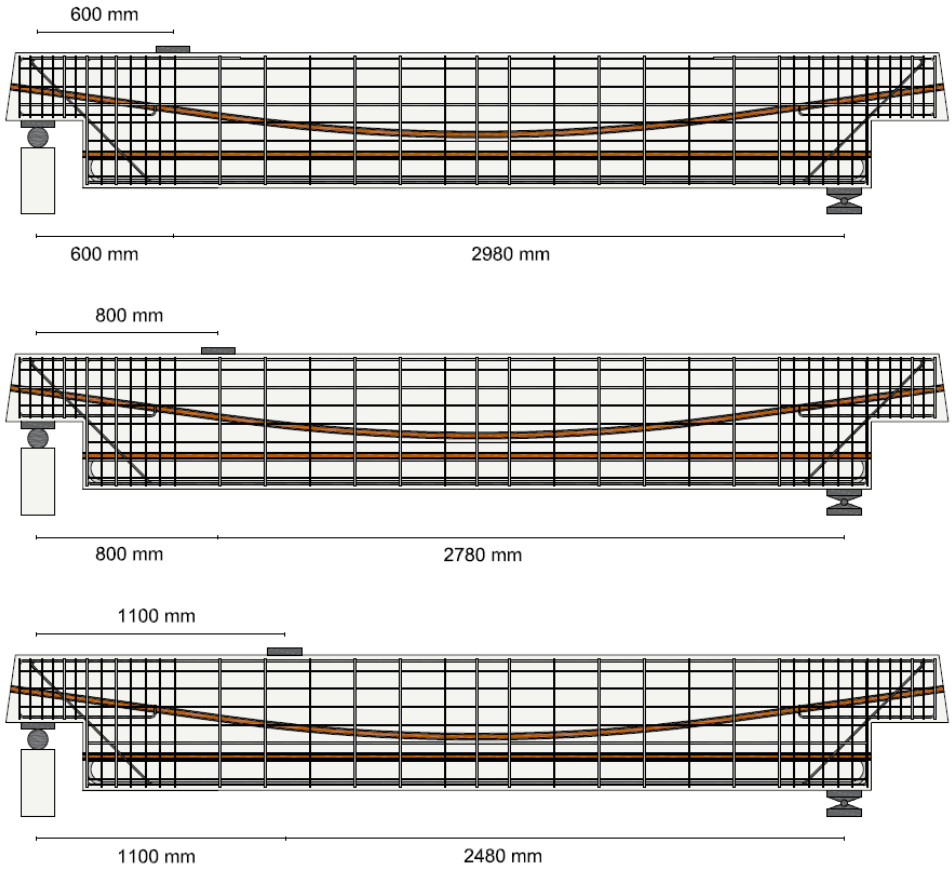

Figure 97. Loading configuration for the shear span investigation.

Results

The results of the parametric analysis show that the parameters investigated, shear span length and concrete fracture energy, do not significantly affect the ultimate capacity of the dapped-end beam specimens. This can be seen by comparing the pushover curves, in Figure 98, obtained by recording the support reaction and the deflection below the point of load application.

Analyzing the first parameter in detail, the assumed minimum shear span value of 600 mm proved sufficient to avoid the formation of the resistant arch mechanism that would lead to an overestimation of the dapped end strength. For larger values of shear span, the developed resistant mechanism remained unchanged and the fracture did not shift toward the shear-bending fracture of the beam, demonstrating the effectiveness of the design of the beam shear and bending reinforcement.

The fracture energy, contrary to the findings for the Desnerck's group specimen, has a minor influence on the ultimate capacity of the dapped-beam end. In fact, a small increase in ultimate capacity is noted as the fracture energy increases, which remains for all cases analyzed below the maximum value of 3.29%. It is worth noting that the lower value of 20 kN/m suited on the benchmark case caused numerical instability and marked brittleness for specimens RL-C (in purple) and for RL-A3 (in orange) with shear span equal to 1100 mm; In these cases, the absence of ductility did not allow the expected ultimate capacity to be reached, as it does for higher values of fracture energy; the ultimate capacity has reached a decrease in capacity by as much as 72%. The results obtained in terms of ultimate capacity are summarized in Table 13.

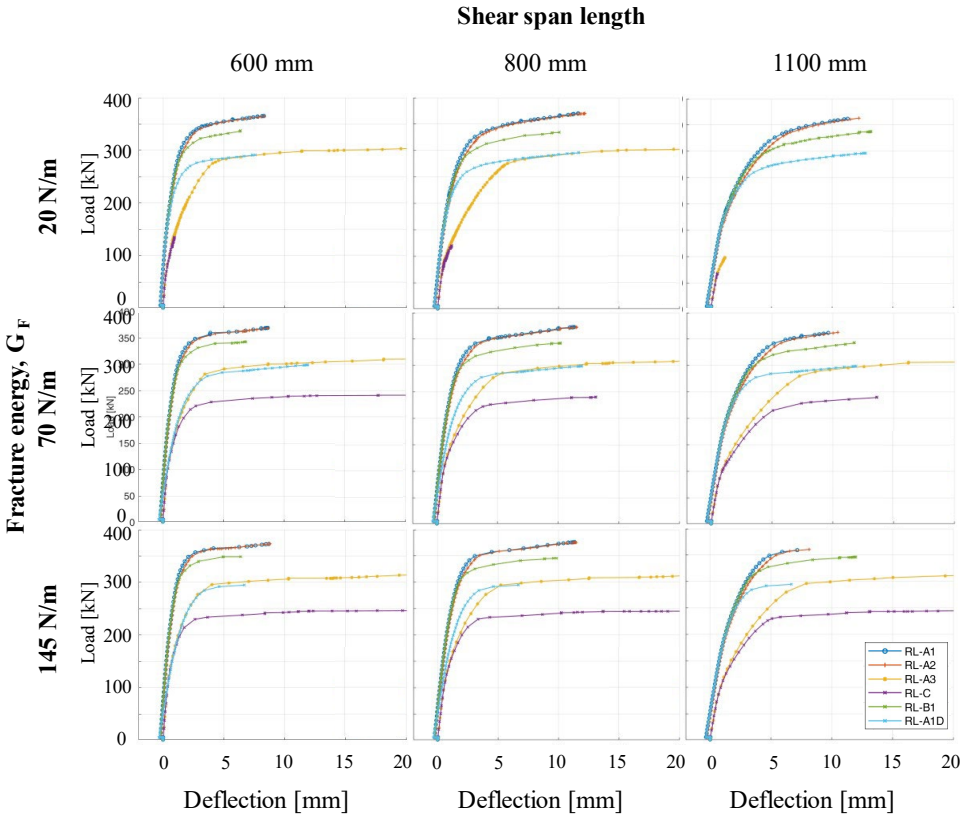

Figure 98. Parametric analysis results for different fracture energy and shear span length values.

Table 13. Parametric analysis results in terms of ultimate shear capacity.

	Ultimate Shear Capacity [kN]								
Shear Span [mm]	600	600	600	800	800	800	1100	1100	1100
G_F [kN]	20	70	145	20	70	145	20	70	145
Specimen **RL-A1**	365.36	369.42	373.08	370.39	372.88	376.43	362.85	362.85	362.99
RL-A2	364.44	368.81	373.24	370.13	372.65	375.70	364.23	364.27	364.38
RL-A3	307.50	318.13	316.58	315.31	312.95	314.78	98.34	316.83	314.07
RL-C	134.96	242.55	246.95	119.94	240.29	245.63	67.98	239.70	245.49
RL-B1	337.65	342.96	348.46	334.75	342.49	346.16	337.49	343.60	348.46
RL-A1D	290.95	299.69	294.68	296.61	299.69	294.68	296.55	298.82	294.68

Given the numerical instability found in the RL-C and RL-A3 specimens for the G_F value of 20 N/m, and given the minimal influence of fracture energy on ultimate capacity, the reference value of 70 N/m is selected for estimating the ultimate capacity of the laboratory specimens, in accordance with the *fib* Model Code 1990.

As predicted, the variation in shear span did not have a significant impact on the ultimate capacity of the elements. In fact, the changes recorded were less than 3% (for G_F equals to 70 N/m).

Given the results of the parametric investigation, the shear span for laboratory experimentation is set equal to 800 mm. This value was found to prevent the formation of the arch unloading mechanism and is short enough to prevent shear/flexural failure of the beam outside the disturbed region. The expected pushover curves are then shown in Figure 99.

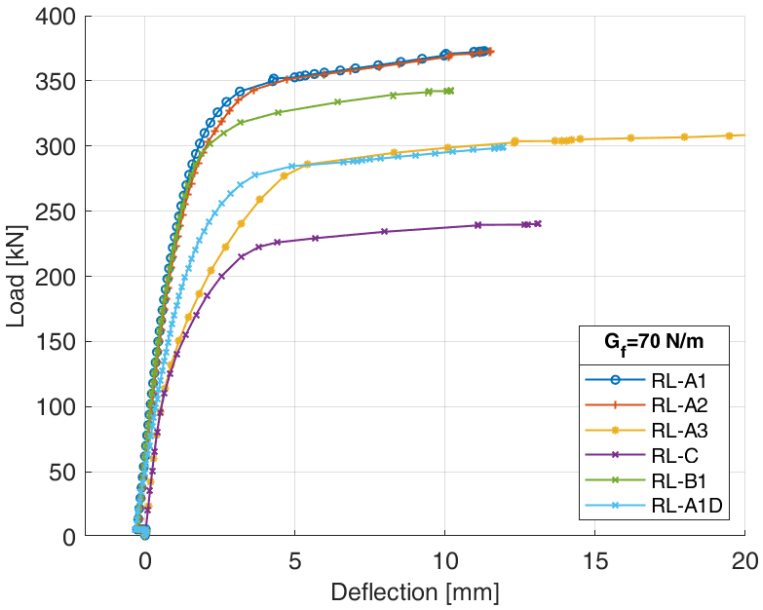

Figure 99. Pushover curve for fracture energy and shear length equal to 70 N/m and 800 mm.

The analyses show the formation of a failure mechanism involving the re-entrant corner of the nib. From this point, a 45-degree crack starts and propagates toward the point of load application. Visualizing the accumulation of plastic deformation on the concrete reveals that a large area near the internal corner is affected by plasticity phenomena (see Figure 100).

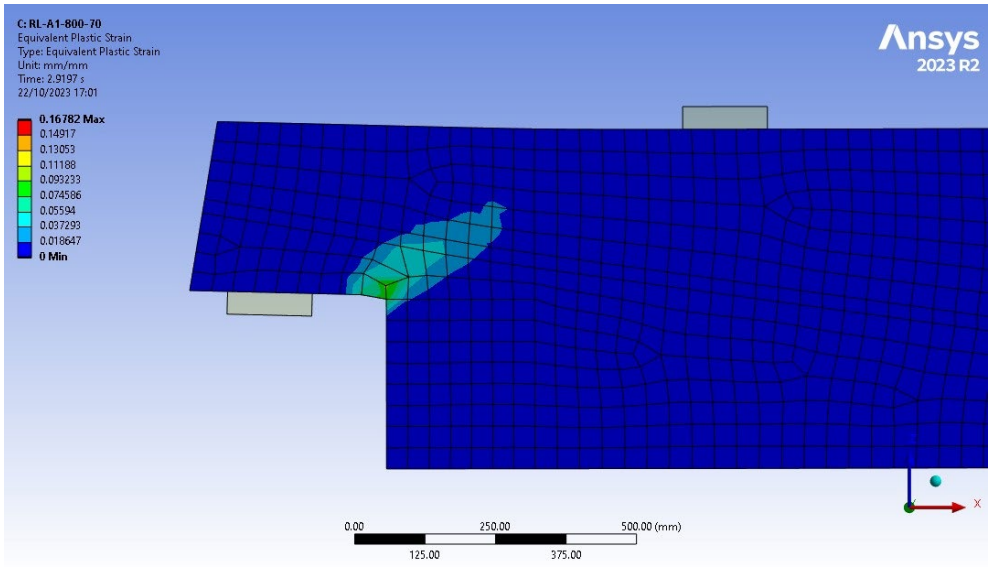

Figure 100. Equivalent plastic strain distribution on concrete elements.

In the final load steps, the diagonal, horizontal, and vertical main bars are extensively hardened. The yielding begins to involve the vertical and horizontal reinforcement arranged along the concrete cracking zone. This can be seen in Figure 101, where the equivalent stresses (Von-Mises) are shown and the stress state equals to the yielding stress of 495 MPa is represented in yellow. The reinforcements located in the plasticity zone begins to work to stitch the crack and to limit its opening, by accumulating plastic deformation, as shown in Figure 102.

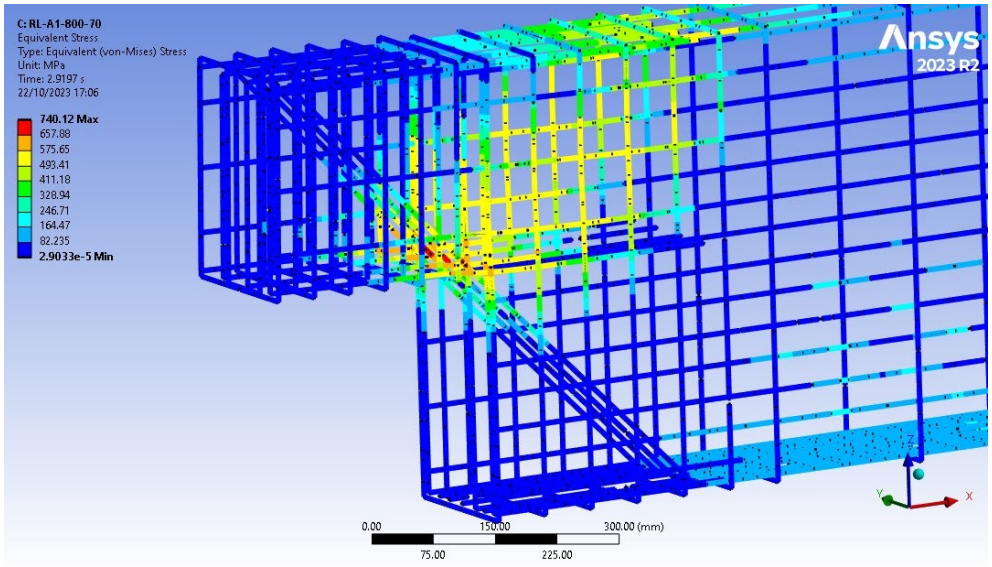

Figure 101. Equivalent Von-Mises stress distribution on reinforcements.

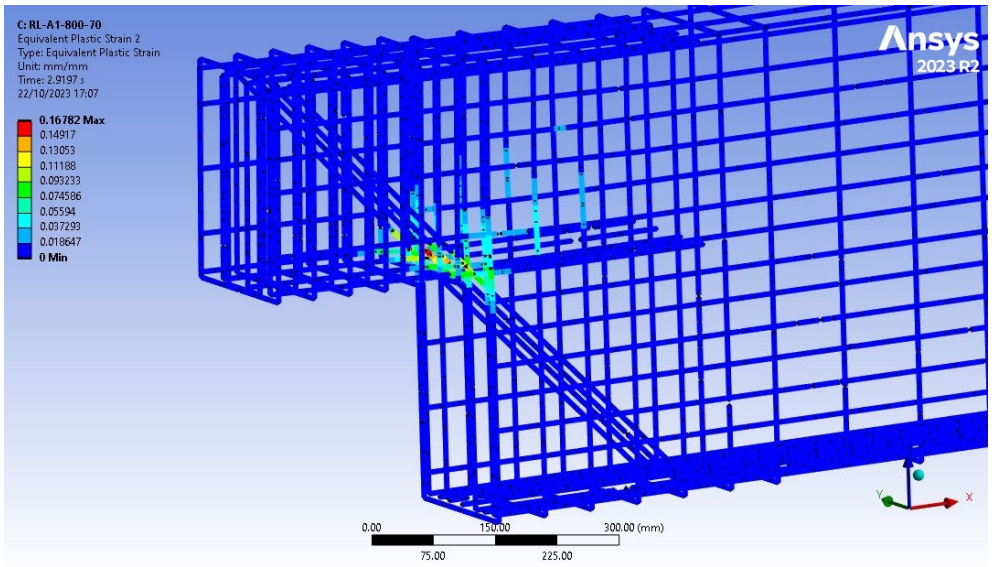

Figure 102. Equivalent plastic strain distribution on steel reinforcements.

The resisting mechanism can be divided into three main steps: diagonal reinforcement yielding, horizontal reinforcement yielding, and finally vertical reinforcement yielding. Only prestressed specimens RL-A1 and RL-A2 show a rapid transition from the first yielding step (diagonal reinforcement) to the last steps (main reinforcement yielding), without going through the intermediate stage. For each of these steps, the recorded bearing load values are shown in Table 14 below.

Table 14. Yeilding points of the main reinforcements for different specimens.

	Specimen					
Yielded bars	**RL-A1**	**RL-A2**	**RL-A3**	**RL-C**	**RL-B1**	**RL-A1D**
Diagonal [kN]	245.97	246.93	168.47	140.42	261.95	227.57
Diagonal-Horizontal [kN]	-	-	222.66	200.22	293.88	241.84
Diagonal-Horizontal-Vertical [kN]	317.89	303.10	276.82	225.95	309.81	256.08

The comparison of the ultimate capacities obtained with the FE models and the prediction made with the analytical strut-and-tie models is summarized in Table 15. In all cases, the strut-and-tie models were more conservative in predicting the ultimate load of the beams.

Table 15. Ultimate capacity comparison between FE models and strut-and-tie models.

Specimen	**FEM** [kN]	**S&T** [kN]	**FEM/S&T** [-]
RL-A1	372.88	211.19	1.77
RL-A2	372.65	199.00	1.87
RL-A3	312.95	120.22	2.60
RL-C	240.29	211.19	1.14
RL-B1	342.49	185.17	1.85
RL-A1D	299.69	120.22	2.49

5 In-situ eperimental campaign on existing drop-in span segment

In collaboration with the FABRE research group and ANAS, an extensive testing campaign was planned in conjunction with the demolition and reconstruction of one of the inspected structures, which was found to be non-compliant with the safety standards required by regulations.

Test set up

The testing program includes an initial phase dedicated to enhancing our understanding. The primary objective of these tests is to characterize the ultimate shear capacity of the typical span of an existing bridge. The primary motivations for conducting the experiments are both scientific and safety-related. The main reasons include:

- The viaduct was closed due to evident and significant states of degradation affecting the prestressed dapped-end beams and revealing defects in the integrity of the prestressing cables (e.g., traces of moisture from inside the cables).

- The viaduct, in its suspended span of 60 m, exhibits a significant permanent deflection, resulting in pavement-level depressions that are easily visible without specific measuring instruments.

- On the twin viaduct, which currently accommodates traffic from both roads, cracks inclined at about 45° were observed on the bottom corner of the nib full-depth interface. These cracks are consistent with a damage mechanism due to shear forces and may indicate a loss of prestressing level. These cracks, which were not detected during the Level 2 inspection, might indicate an evolution of the crack pattern. The main causes can be investigated by performing the tests outlined in the following testing project.

As previously mentioned, the ultimate goal of the tests is to characterize the behavior of the dapped-end beam up to failure, with a specific focus on shear behavior. This will be investigated through three-point bending tests. However, a series of additional tests are planned, that are not only functional for the design and interpretation of the load test outcomes, but also offer the opportunity to investigate specific aspects of the structure. In detail, in addition to a precise geometric survey for quantifying the permanent deformations of the span in its current configuration (through laser scanner or topographic surveys), a series of investigations are planned to assess the defectiveness of the prestressing system, according to the technical documentation published by FABRE Consortium for conducting special inspections based on the Italian bridge guidelines. The latter investigations are designed with a dual purpose: (i) to assess the operational practicality (for the case under consideration) and effectiveness of various tests, useful for surveying the cable layout and possible defects (e.g., presence of voids in the duct, irregularities in the tracks), and (ii) to assess the reliability of results among different types of semi-destructive and non-destructive tests conducted in situ.. Given the presence of defects (indicating the deteriorating

condition of the prestressing reinforcement) on the cantilevered girder section from the pier near the dapped-end beam subjected to the load tests, the aforementioned investigations will also be extended to the latter.

The investigation campaign includes an evaluation of the residual tension in the prestressing cables, both through diffractometric tests and tension release tests on both steel and concrete, in line with the dual purpose stated above. Finally, durometric tests will also be performed on the prestressing steel, which can be subjected to tensile tests following demolition. Again, this dual mode of investigation will help to define the existing correlation between the hardness assessed by in-situ durometric tests and the ultimate tensile strength of the cables. In addition, a thorough characterization of all materials and construction details (concrete, steel reinforcements, and high-tensile steel of the prestressing system) will be carried out. The necessary number of tests will be planned to estimate the mechanical properties of materials in accordance with Italian bridge guidelines, with a focus on assessing the reliability of pull-out tests for estimating the compressive strength of concrete. To this end, both destructive tests (core testing) and pull-out tests, performed around the extracted cores, will be planned.

The tests to be performed on the suspended span, which will be the subject of the experimentation, will focus on the portions of the deck that will be demolished, specifically on the lateral webs. Following the execution of the tests, the controlled demolition of the lateral webs is planned, once the diamond saw cuts have been made, in order to recover the prestressing cable ducts. The recovery of prestressing cable duct is also planned for the two cantilevered girders of the two piers near the suspended span, which will be

investigated. All the metallic ducts will subsequently be spread and opened for a direct visual inspection of cable conditions and injections. During the demolition, construction details such as concrete covers, layout and diameters of reinforcements, spacing of stirrups, and the actual position of cables will be surveyed concurrently. This is to reassess the reliability of the tests performed and to ensure compliance with the design drawings.

In summary, the purposes of the proposed tests can be summarized as follows:

- Conducting an accurate geometric survey of the span under study to reliably estimate the weight of the structure and evaluate the permanent viscous deformations accumulated over the years of service.

- Evaluating the defectiveness of the prestressing system, including the residual tension in the prestressing cables, and concurrently, assessing the effectiveness and reliability of the planned tests.

- Performing a mechanical characterization of materials, which includes concrete, reinforcement steel, and high-tensile steel.

In the following sections, we will detail the tests to be performed on the lateral webs of the girder box before proceeding with their controlled demolition.

Tests Designed for Comprehensive Bridge Survey

Considering the significant residual deflection exhibited by the suspended span, it is particularly interesting to conduct a laser scanner survey of the span and an appropriate portions of cantilevered girders, extending up to the piers.

The aim is to numerically assess the magnitude of the permanent deflection. This information can provide useful insights for indirect numerical assessments of the state of residual prestress in the cables. The laser scanner survey will also provide all the necessary information for a systematic verification of the correspondence with the design drawings. This is necessary for a reliable structural model for the design, prediction, and interpretation of the outcomes of the proposed test.

Additionally, if the removal of the road pavement from the deck is not planned, a georadar test is considered necessary to evaluate the pavement thicknesses. Also, three cores are required for the evaluation of the volumetric mass of the pavement.

Crack Identification

The suspended span beam exhibits a crack pattern at the dapped end, oriented towards Rome, on the side of the overtaking lane (Figure 103). This will be examined to determine the depth of the crack and its full extent, in order to ascertain any potential correlation with the dapped-beam end resistance mechanisms.

Figure 103. Cracks on the dapped-end beam.

Likewise, the crack patterns on the cantilevered girded on both sides of the suspended span, which show signs of defects in the cable integrity, will be charted (Figure 104. and Figure 105.).

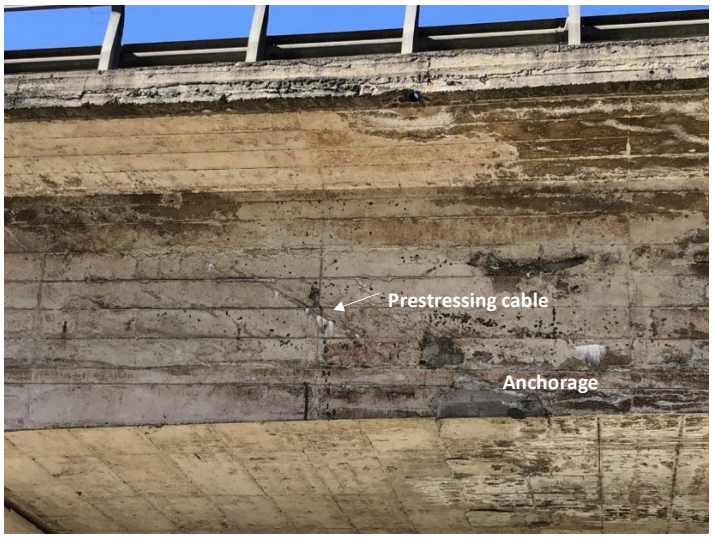

Figure 104. Cantilevered girder of the 3th span.

Figure 105. Cantilevered girder of the 5th span.

Tests on The Prestressing System

As previously mentioned, the tests on the prestressing system, conducted on the lateral webs of the box girder, serve a dual purpose. They aim to assess the technical-operational feasibility and the effectiveness of various tests that can provide the same information. Specifically, these include:

- Georadar tests with a frequency of no less than 2 GHz, intended for identifying the cable paths. The test will be conducted on one of the two lateral webs with the goal of reconstructing the entire path of the prestressing cables. For the remaining web, the test may be performed solely to identify the position of the cable to be tested, as per the following specifications.

- Ultrasonic tomographies: Given the presence of metallic ducts, ultrasonic tomographies will be carried out to detect not only the tracing but also any defects in the cable injections.

This investigation will be conducted for a lateral web of the box girder and across the entire length of the cables. The information obtained can be used to redefine the location of the investigation points for subsequent tests (diffractometric, hardness, tension release). Both the quantity and the indicative position of these points are defined below.

In areas identified as defective by tomographic tests, the execution of assays for direct detection of the defect may be considered. However, it is possible that the execution of assays may be deemed unnecessary if the complete extraction of the cable can be envisaged during the controlled demolition. Even in this case, the execution of some assays could be considered of interest

for the purpose of assessing the usefulness of the assays (and the success rate) in detecting the defect that may be in a hidden position with respect to the access area for the assay. The investigation will also include the following tests:

- Impact echo [57–59]: Similar to tomographic tests, this test provides information on the defectiveness of the cables, specifically in terms of the presence of cavities. A limited number of tests (5 tests) are expected to be performed in the defective areas identified by the tomographies.

- Pacometric surveys: These tests, like georadar tests and tomographies, provide an indication of the location of prestressing cables. Sample tests (at least 5 assays) are expected to evaluate the efficiency of this test in returning information of equal accuracy to tomographic and georadar tests.

- Corrosion potential mapping: At the locations of the cables subjected to release, hardness, and diffractometric tests, corrosion potential tests will be concurrently performed to assess the susceptibility of the reinforcement to corrosion in the context of the structure under study.

- Tension release tests on cables : Each web of the deck contains 2 M5/20 cables (20 strands, 7 strands each) and 1 M5/16 cable (16 strands, 7 strands each), totaling 392 strands. The M5/16 cable is anchored in the slab, follows a symmetrical path, and is tensioned on both sides. The two M5/20 cables, on the other hand, follow a path

that is not symmetrical but mirrored with respect to the centerline, with one side anchored and the other tensioned (to restore tensional symmetry in the presence of friction losses). There will be 2 tension release tests near each support (1 on the M5/20 cable and 1 on the M5/16 cable), and for each web (2 supports x 2 cores x 2 cables = 8 tests), and 2 tests in the centerline (1 on the M5/20 cable and 1 on the M5/16 cable) of each web (2 cores x 2 tests = 4 tests). This totals 12 tension release tests, as shown in Figure 106. The exact location of the test will be determined after the outcome of the tomographic tests. The release tests should be performed after the diffractometric tests, hardness tests, and corrosion potential mapping.

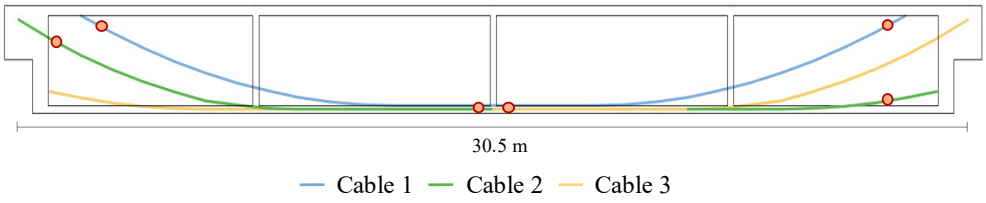

Figure 106. Test points on prestressing cables on the suspended span.

- Diffractometric tests [60–62]: these tests, which are useful for estimating the residual tension in the cables, will be conducted on 12 cables that have undergone tension release (Figure 106.). These tests will be the first to be performed once the cable has been stripped in its various positions.

- Tension release tests on the concrete: these tests, which are useful for providing the tension in specific sections of the structure based on the

assumption of plane section conservation, will be conducted in the center of the concrete for each web, in two different positions of the section, according to the scheme in Figure 107.

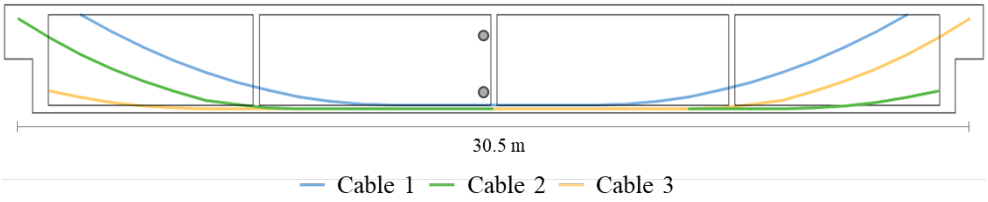

Figure 107. Test points on concrete webs on the suspended span.

- Evaluation of stress increases on the concrete and prestressing steel under load: before conducting the tension release tests on the high-tensile steel and concrete in the mid-span section only, the strain increase, measured by strain gauges installed for the execution of the tension release tests (on both concrete and steel), due to a known load placed in the mid-span section of the deck, should be measured. This load may consist of a 40 tons truck.

Tests on Prestressed dapped-end beam

As previously mentioned, the cantilevered girders adjacent to the suspended span exhibit clear signs of potential deterioration of the prestressing system (Figure 104 and Figure 105). Therefore, a limited number of investigations on the external web of the box girder of these portions of the deck are also planned. More specifically, the following are anticipated:

- Georadar tests with a frequency of no less than 2 GHz aimed at identifying the route of the cables: The test will be conducted on one

of the two lateral webs of one of the two cantilevered girders, with the objective of reconstructing the entire path of the prestressing cables from the dapped-beam end to the pier.

- Ultrasonic tomography: Assuming the presence of metallic ducts, ultrasonic tomography will be conducted to detect any defects in the cable injections, in addition to the layout. This investigation will be carried out for a lateral web of each of the two cantilevered girders, and for the entire development of the cables (up to the pier), with priority given to the cables that show signs of defects. The information obtained can be used to redefine the position of the investigation points for the subsequent tests (diffractometric and tension release), for which both the number and the indicative position are defined below. In the defective areas identified by the tomographic tests, the execution of tests for the direct survey of the defect may be considered. However, it is believed that the execution of tests may be excluded if the complete extraction of the cable duct (up to the piers) and the opening after the controlled demolition may be considered. As previously mentioned, the execution of some tests may be considered of interest for the purposes of assessing the usefulness of the tests (and the success rate) in identifying the defect that may be in a hidden position with respect to the access area for the test.

- Impact echo: similar to the tomographic tests, this test provides information on the defectiveness of the cables, in terms of the

presence of cavities. A limited number of tests (4 tests) are to be carried out in the defective areas identified by the tomographies.

- Corrosion potential mapping: at the locations of the cables subjected to the release and diffractometric tests, corrosion potential tests will be conducted simultaneously, in order to assess the susceptibility of the reinforcement to corrosion in the context of the structure under study.

- Tension release tests on the cables: on each core of the deck, there are 6 M5/20 cables (20 strands, each with 7 wires), for a total of 840 wires. One tension-relieving test is planned at the deepest cable above the pier, for each cantilever (2 side webs x 2 cantilevers x 1 cable = 4 tests), for a total of 4 tension-relieving tests, according to the diagram in Figure 108. The exact location of the test will be defined after the results of the tomographic tests. The release tests should be carried out after the diffractometric tests and corrosion potential mapping.

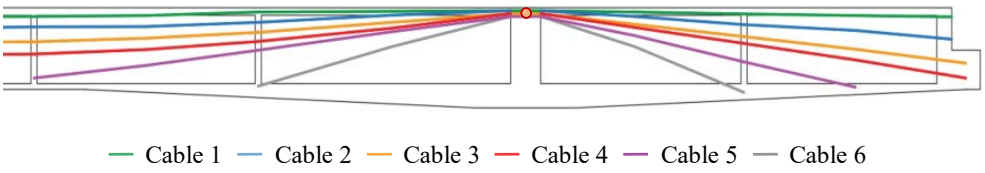

Figure 108. Test points on prestressing cables on the cantilevered girder.

- Diffractometric tests: these tests, which are useful for estimating the residual tension in the cables, will be conducted on 4 cables that have

undergone tension release (Figure 109). These tests will be the first to be performed once the cable has been exposed in its various positions.

- Tension release tests on the concrete: these tests, which are useful for providing the tension in specific sections of the structure, will be conducted for each cantilever at the support in two different positions of the section, according to the diagram in Figure 107, starting from the assumption of plane section conservation.

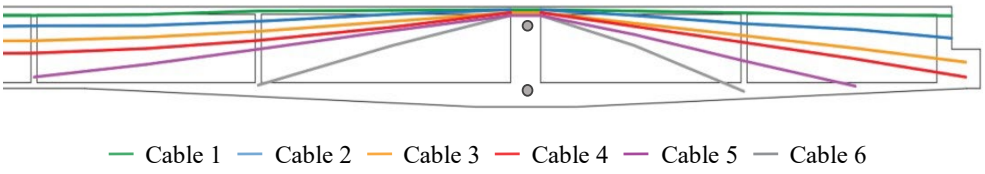

Figure 109. Test points on concrete webs on the cantilevered girder.

- Cores for concrete compression tests: eight cores are to be extracted, distributed over the two webs, with four per web (two at the dapped-beam ends, if possible, and two at the quarters of the span). The specific weight and thickness of the carbonated concrete will be measured on the extracted cores using phenolphthalein.

- Pull-out tests: three pull-out tests will be performed around each web for a total of 24 pull-out tests.

- Hardness tests on prestressing steel: the document “Special inspections on existing prestressed RC bridges according to the

Guidelines: classification and accurate assessment" [28,29] proposes different types of tests - HV (Vickers hardness), HB (Brinell hardness), HR (Rockwell hardness) - for an indirect estimate of the tensile strength of prestressing cables. Hardness tests are to be carried out at the positions of the release/diffractometer tests. The hardness test is to be carried out after the diffractometer test and before the release test. After the cable has been stripped, if the cable proves to be too defective for the test to be performed, a new section will be selected.

- Tensile tests on rebars and on prestressing cables: after controlled demolition, pieces of rebars and high-tensile steel wire will be extracted for tensile tests (10 pieces of rebars, taking care to include pieces of stirrups, and 10 pieces of high-tensile steel wire).

Direct survey of cavity defects and construction details

During the controlled demolition phase, a direct survey of the reinforcement cover, diameters, and spacing will be carried out, with particular reference to the stirrup spacing in the end sections and mid-span section, as well as the demolished portion of the dapped end. This survey will be instrumental in verifying the construction compliance with the design drawings. In addition, the complete extraction of the prestressing cable ducts of the suspended girder and the cantilevered girders (up to the piers) is planned. Their opening for a systematic mapping of the defects and a comparison with the results obtained from the previous surveys is also planned.

Summary of planned tests

Tests on suspended span

	N. Tests	Work programme
Geometric survey		
Laser scanner	1	
Georadar (road pavement)	1	
Cores (road pavement)	3	
Crack survey		
Crack path and width (dapped end)	1	
Tests on prestressing system		
Georadar	Entire path on 1 web + position of other tests	
Ultrasonic tomography	Entire path on 1 web	
Impact echo	5	
Pacometric surveys	5	
Corrosion potential mapping	12	
Diffractometric tests	12	
Tension release on steel	12	
Tension release on concrete	4	
Hardness tests	12	
Destructive tests for material characterization		
Cores	8	
Pull -out	24	
Tensile tests on rebars	10	
Tensile tests on high -tensile steel	10	

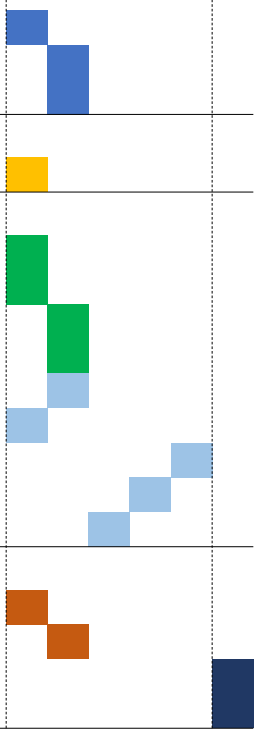

Tests on cantilevered girders

	N. Tests	Work programme
Geometric survey		
Laser scanner	1	
Tests on prestressing system		
Georadar	Entire path on 1 web + position of other tests	
Ultrasonic tomography	Entire path on 1 web	
Impact echo	4	
Corrosion potential mapping	4	
Diffractometric tests	4	
Tension release on steel	4	
Tension release on concrete	4	

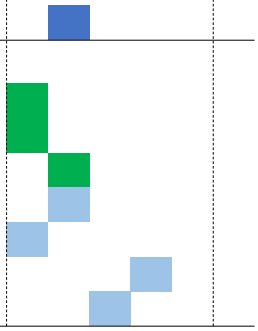

Three-point asymmetric bending test

It is proposed to conduct three-point bending tests at the construction site of the suspended span girder, which will be suitably reduced by cutting the lateral webs, in accordance with the outline diagram in Figure 110, where the current section of the viaduct is shown. Initially, destructive tests will be conducted on the construction materials by proceeding with the extraction of cores, pieces of reinforcement, and pieces of cables in the webs and slab of the portions that will be removed. Subsequently, tension release tests on prestressing cables will be carried out on the same portions.

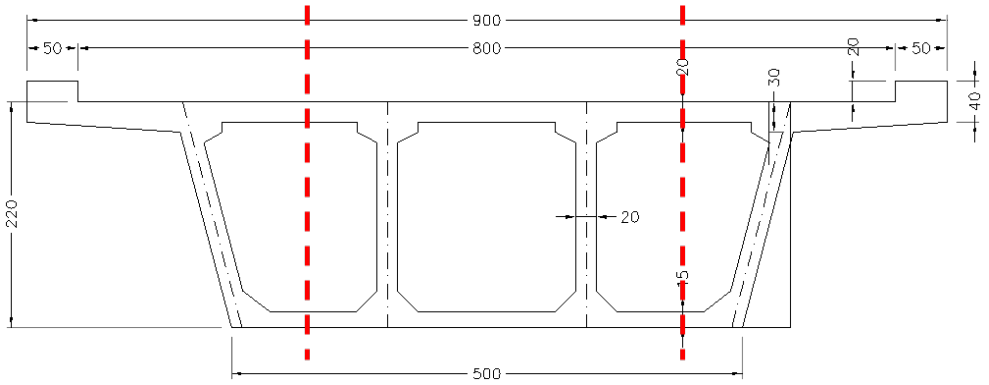

Figure 110. Cross-section reduction by cutting the external webs of the box girder.

Once the destructive investigation campaign has been carried out, the lateral portions can be cut. This will lighten the deck, allowing it to be dismantled by a crane and placed in a site area dedicated to the execution of tests. The cellular box girder will place on dedicated concrete supports, while the load will be imposed by hydraulic jacks counteracted by a crossbeam anchored by Dywidag bars to large-diameter foundation piles. The Dywidag bars will be embedded in the casting of the piles and will extend in elevation up to the

level of the top crosshead. Concrete columns (encompassing the Dywidag bars) will be built above the pile foundation, with the aim of providing support for the crosshead contrasting the jacks. The applied load will be measured using load cells, while centesimal comparators will be used to measure displacements. During the application of the load, which will increase according to steps to be defined, displacements and the evolution of the crack pattern will be monitored. Cameras may also be used to detect the deformational state of the core panels subject to shear, and vibrational measurements may be made at different damage levels to correlate the dynamic parameters to the damage.

The dimensions of the current cross section of the beam after the saw cut are shown in Figure 111. The Morandi system was used for prestressing; for each of the webs of the suspended span beam, the cables shown in Table 16 are present.

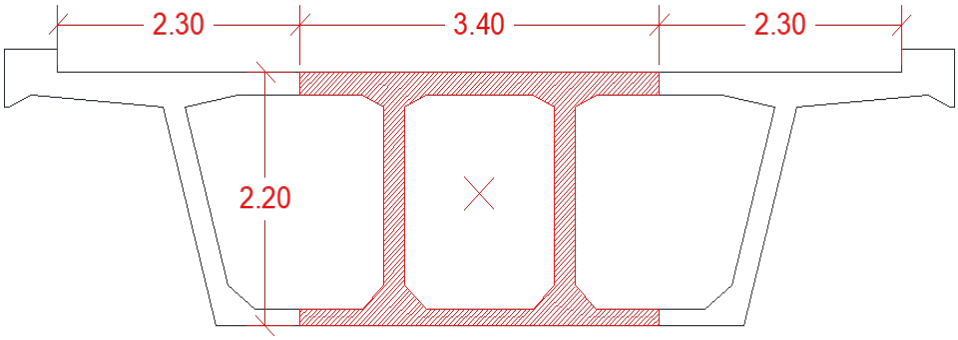

Figure 111. Cross section of the box beam after the saw cut.

Table 16. Geometric characteristics of the Morandi prestressing system.

Beam	Prestressing cable	Area section [cm^2]	Web cable number
Dapped-end beam	M5/20	18.60	2
	M5/16	14.864	1

With regard to materials, reference is made to the average strength values obtained from the survey campaigns. For concrete, since the slenderness ratio H/D of the cores is always equal to unity, the values given on the reports constitute cubic compressive strengths Rc. First, the disturbance factor is applied to these values, as indicated in the NTC 2018 Circular, C11.2.6, Table C11.2.6.I. Then, the results are converted to cylindrical compressive strengths according to the following relationship:

$$f_{c,core,sn} = f_{c,core} * [0.83 + (1 - 0.83) * (\frac{H}{D} - 1)]$$

where:

- $f_{c,cores}$ given as the result of the compression test
- $f_{c,core,sn}$ result of the compression test, corrected for buckling effects.

The results are summarized in Table 17 below.

Table 17. Results of concrete testing.

n°	Name	Position of the sample	D	H	H/D	R_c	F_d	$R_{c,is}$	$f_{c,is}$
-	-	-	mm	mm	m	MPa	MPa	MPa	MPa
1	C17C	Nord roadway-Span 8-Regular Lane	94	94	1	23.03	1.09	25.10	20.84
2	C18C	Sud roadway-Span 1-Regular Lane	94	94	1	20.94	1.09	22.82	18.94
3	C19C	Sud roadway-Span 3-Regular Lane	94	94	1	21.65	1.09	23.60	19.59
4	C20C	Sud roadway-Span 4-Regular Lane	94	94	1	21.57	1.09	23.51	19.51
5	C27C	Nord roadway-Span 4-Regular Lane	94	94	1	22.34	1.09	24.35	20.21
6	C28C	Nord roadway-Span 3-Regular Lane	94	94	1	22.84	1.09	24.90	20.66
7	C29C	Nord roadway-Span 1-Regular Lane	94	94	1	23.58	1.09	25.70	21.33
8	C30C	Sud roadway-Span 5-Regular Lane	94	94	1	23.89	1.09	26.04	21.61
9	C31C	Sud roadway-Span 8-Regular Lane	94	94	1	22.84	1.09	24.90	20.66
10	C5	Span 6-Roma direction	104	104	1	34.26	1.06	36.32	30.14
11	C6	Span 8-Fano direction	104	104	1	35.96	1.04	37.40	31.04
12	C7	Span 6-Fano direction	104	104	1	38.46	1.04	40.00	33.20
13	C8	Span 7-Fano direction	104	104	1	36.2	1.04	37.65	31.25
14	C9	Span 7-Roma direction	104	104	1	42.66	1.04	44.37	36.82
15	C10	Span 1-Fano direction	104	104	1	30.13	1.06	31.94	26.51
16	C11	Span 1-Roma direction	104	104	1	34.55	1.06	36.62	30.40
17	C12	Span 2-Roma direction	104	104	1	23.59	1.09	25.71	21.34
18	C13	Span 8-Roma direction	104	104	1	35.56	1.04	36.98	30.70
19	C14	Span 3-Roma direction	104	104	1	35.4	1.04	36.82	30.56
20	C15	Span 3-Roma direction	104	104	1	38.27	1.04	39.80	33.03
21	C16	Span 2-Fano direction	104	104	1	40.73	1.04	42.36	35.16
22	C43	Span 2-Roma direction	104	104	1	22.82	1.09	24.87	20.65
23	C44	Span 2-Roma direction	104	104	1	25.34	1.08	27.37	22.71

It is obtained for concrete:

$$f_{cm} = 25.95\ MPa$$

Similar to what was done for concrete, the average strength value obtained from the tests is also considered for reinforcement steel. The results of the tests are shown in Table 18.

Table 18. Results of tests on steel reinforcement.

N° test	ID	Location	fy
[Text]	[Text]	[Text]	[N/mm²]
1	A14C	Deck	432.15
2	A15C	Deck	431.47
3	A16C	Deck	433.62
4	A17C	Deck	433.65
5	A18C	Deck	435.66
6	A19C	Deck	431.00

The average strength value for steel is:

$$f_{ym} = 432.93\ MPa$$

For the characterization of the steel of the prestressing cables, reference was made to the tests performed for the acceptance of materials (Table 19), which provide the value of tensile strength. The strength at 1% total strain for the cables was derived by setting it equal to 85% of the rupture strength, within the range of 80-95% as indicated in DM 30.05.1974.

Table 19. Results of tensile tests on prestressing steel.

N° test [Text]	f_u [kg/mm^2]
1	193.84
2	188.15
3	167.12
4	193.27
5	187.02
6	193.27
7	181.9
8	194.97
9	194.97
10	197.82
11	193.27
12	194.41
13	192.13
14	191.56
15	193.84
16	170.53
17	181.9
18	193.84
19	191.56
20	171.1

The computational yield strength of prestressing steel determined by the tests was found to be equal:

$$f_{pm} = 1847.45\ MPa$$

With reference to bending, the expected capacity is calculated, considering the average strength values of materials and unit partial safety coefficients, in 3 sections (N, O, P) along the development of the beam (Figure 112.), as shown in Figure 113 - Figure 115.

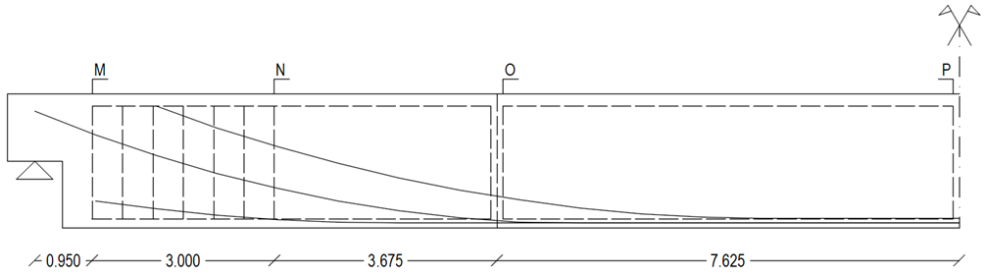

Figure 112. Section details for capacity calculation.

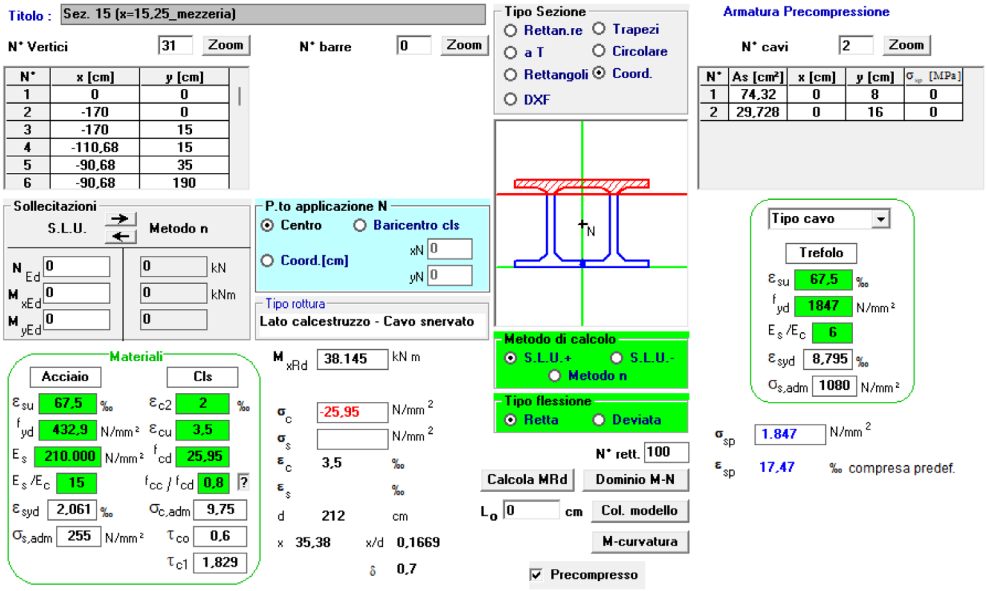

Figure 113. Bending resistance section P.

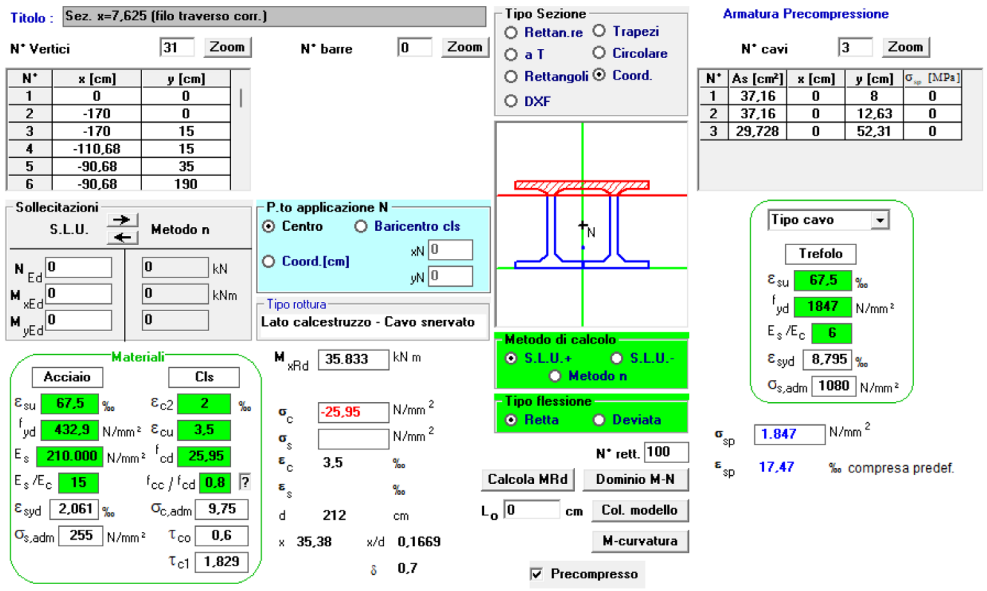

Figure 114. Bending resistance section O.

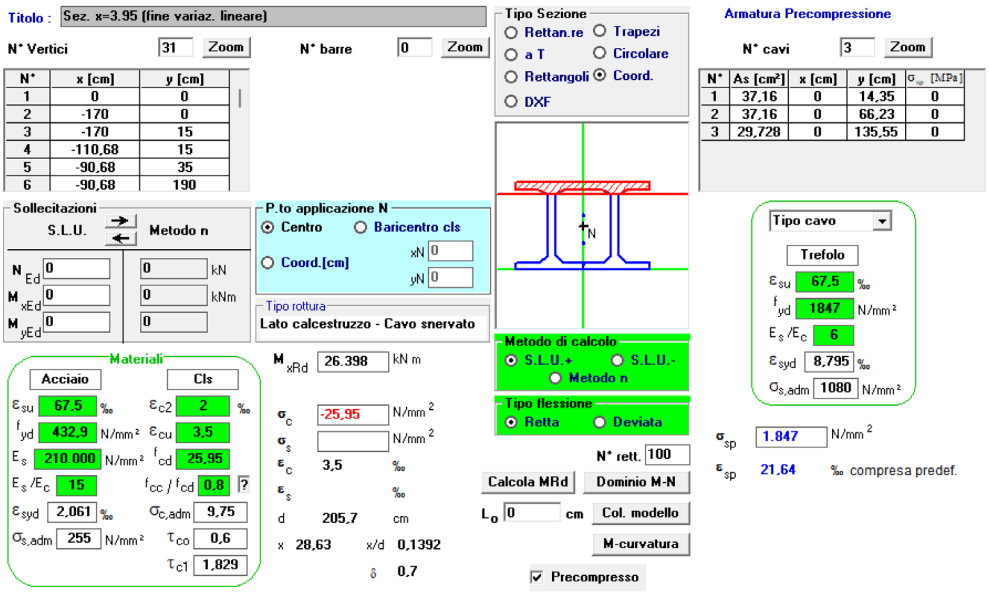

Figure 115. Bending resistance section N.

Table 20 summarizes the expected flexural strengths for different sections.

Table 20. Summary of verification results for normal stresses, suspended span beam.

Section	**Progressive**	**M_R**
[-]	[m]	[kNm]
N	3.95	26398
O	7.625	35833
P	15.25	38145

As for the bending strength, the shear strength is calculated in the sections above taking into account the shear reinforcement in each section. The strengths below refer to the development of a resistant strut-and-tie mechanism after the crack opening.

Shear capacity – Section M

Element	**b_w**	**d**	**A_{sw}/s**	**α_c**	**v**	**f_{cd}**	**f_{yd}**	**θ**	**V_{Rcd}**	**V_{Rsd}**	**V_{Rd}**
	[mm]	[kN]	[mm²/mm]	[-]	[-]	[Mpa]	[Mpa]	[°]	[kN]	[kN]	[kN]
WEB 2	400	2170	1.13	1	0.5	25.95	432.93	21.8	3495.14	2390.77	2390.77
WEB 3	400	2170	1.13	1	0.5	25.95	432.93	21.8	3495.14	2390.77	2390.77

Shear capacity – Section N

Element	**b_w**	**d**	**A_{sw}/s**	**α_c**	**v**	**f_{cd}**	**f_{yd}**	**θ**	**V_{Rcd}**	**V_{Rsd}**	**V_{Rd}**
	[mm]	[kN]	[mm²/mm]	[-]	[-]	[Mpa]	[Mpa]	[°]	[kN]	[kN]	[kN]
WEB 2	200	2170	0.63	1	0.5	25.95	432.93	21.8	1747.57	1328.21	1328.21
WEB 3	200	2170	0.63	1	0.5	25.95	432.93	21.8	1747.57	1328.21	1328.21

Shear capacity – Section O

Element	b_w	d	A_{sw}/s	α_c	v	f_{cd}	f_{yd}	θ	V_{Rcd}	V_{Rsd}	V_{Rd}
	[mm]	[kN]	[mm²/mm]	[-]	[-]	[Mpa]	[Mpa]	[°]	[kN]	[kN]	[kN]
WEB 2	400	2170	1.13	1	0.5	25.95	432.93	21.8	3495.14	2390.77	2390.77
WEB 3	400	2170	1.13	1	0.5	25.95	432.93	21.8	3495.14	2390.77	2390.77

Shear capacity – Section P

Element	b_w	d	A_{sw}/s	α_c	v	f_{cd}	f_{yd}	θ	V_{Rcd}	V_{Rsd}	V_{Rd}
	[mm]	[kN]	[mm²/mm]	[-]	[-]	[Mpa]	[Mpa]	[°]	[kN]	[kN]	[kN]
WEB 2	200	2170	0.63	1	0.5	25.95	432.93	21.8	1747.57	1328.21	1328.21
WEB 3	200	2170	0.63	1	0.5	25.95	432.93	21.8	1747.57	1328.21	1328.21

The table below summarizes the expected shear strengths for different sections, including the contribution of prestressing cables. To estimate the contribution of the prestressing cables, it is necessary to estimate the redistribution of stresses on the cables after the cut of the section, which results in a change in the inertial properties of the section. This calculation is performed iteratively by starting from the currently estimated stresses at the cables and evaluating the changes in them due to elastic deformations of the concrete caused by the change in the inertial properties of the section. The procedure converges within a few steps. The following are the essential steps.

Iter	**A**	**J**	**x_g**	**A**	**J**	**x_g**
[-]	[mm^2]	[kN]	[mm^2/mm]	[-]	[-]	[Mpa]
0	3.74	0.3771	0.55	3740000	3.771E+11	550
1	2.7002	1.6623	1.0589	2700200	1.6623E+12	1058.9
2	2.4767	1.6096	1.0556	2476700	1.6096E+12	1055.6
3	2.26	1.5617	1.0526	2260000	1.5617E+12	1052.6
4	2.05	1.5181	1.0499	2050000	1.5181E+12	1049.9
5	2.05	1.5181	1.0499	2050000	1.5181E+12	1049.9
6	2.05	1.5181	1.0499	2050000	1.5181E+12	1049.9
7	2.05	1.5181	1.0499	2050000	1.5181E+12	1049.9
8	2.05	1.5181	1.0499	2050000	1.5181E+12	1049.9

Section	$\sigma_{p1,fin}$	$\sigma_{p2,fin}$	$\sigma_{p3,fin}$	y_1	y_2	y_3	**1**	**2**	**3**	**1**	**2**	**3**	**1**	**2**	**3**	**1**	**2**	**3**
[-]	[kg/mm²]	[kg/mm²]	[kg/mm²]	[m]	[m]	[m]	[kN]	[kN]	[kN]	[kN]	[kN]	[kN]	[kN]	[kN]	[kN]	[%]	[%]	[%]
0	-	81.88	-	-	0.28	-	-	2984.67	-	-	2927.18	-	-	2984.67	-	-	2	-
1	74.76	81.34	-	1.76	0.67	-	2725.41	2965.03	-	2159.20	2255.23	-	2725.41	2965.03	-	21	24	-
2	75.05	80.84	87.21	1.89	1.01	0.20	2735.76	2947.09	2543.19	1553.20	1755.64	1583.45	2735.76	2947.09	2543.19	43	40	38
3	75.31	80.39	86.68	1.99	1.31	0.55	2745.33	2930.68	2527.93	1841.39	1737.62	1318.53	2745.33	2930.68	2527.93	33	41	48
4	75.54	79.99	86.20	2.06	0.55	0.86	2753.77	2915.98	2513.81	2173.37	1940.65	1306.07	2753.77	2915.98	2513.81	21	33	48
5	75.75	79.62	85.75	2.11	1.76	1.14	2761.40	2902.50	2500.70	2578.16	2381.29	1593.93	2761.40	2902.50	2500.70	7	18	36
6	75.93	79.30	85.33	2.12	1.92	1.38	2768.07	2890.90	2488.60	2842.52	2740.87	1895.50	2768.07	2890.90	2488.60	-3	5	24
7	76.10	79.02	84.95	2.12	2.03	1.58	2774.26	2880.68	2477.52	3008.26	3010.39	2164.12	2774.26	2880.68	2477.52	-8	-5	13
8	76.27	78.78	84.62	2.12	2.10	1.74	2780.46	2871.99	2467.86	3109.30	3177.03	2364.37	2780.46	2871.99	2467.86	-12	-11	4
9	76.44	78.59	84.31	2.12	2.12	1.88	2786.66	2865.00	2458.65	3175.22	3253.56	2532.83	2786.66	2865.00	2458.65	-14	-14	-3
10	76.61	78.42	84.04	2.12	2.12	1.97	2792.88	2858.68	2450.86	3211.26	3277.06	2634.94	2792.88	2858.68	2450.86	-15	-15	-8
11	76.78	78.25	83.81	2.12	2.12	2.02	2799.10	2852.37	2444.06	3233.99	3287.26	2694.55	2799.10	2852.37	2444.06	-16	-15	-10
12	76.96	78.07	83.61	2.12	2.12	2.04	2805.34	2846.07	2438.25	3245.77	3286.50	2712.63	2805.34	2846.07	2438.25	-16	-15	-11
13	77.13	77.90	83.43	2.12	2.12	2.04	2811.58	2839.78	2433.00	3251.76	3279.96	2707.23	2811.58	2839.78	2433.00	-16	-16	-11
14	77.30	77.73	83.25	2.12	2.12	2.04	2817.83	2833.50	2427.76	3257.77	3273.44	2701.85	2817.83	2833.50	2427.76	-16	-16	-11
15	77.51	77.51	83.02	2.12	2.12	2.04	2825.66	2825.66	2421.22	3265.30	3265.30	2695.12	2825.66	2825.66	2421.22	-16	-16	-11

The final stresses on the cables are:

Section	$\sigma_{p1,fin}$	$\sigma_{p2,fin}$	$\sigma_{p3,fin}$
[-]	[kg/mm^2]	[kg/mm^2]	[kg/mm^2]
0	-	80.30	-
1	59.23	61.87	-
2	42.61	48.16	54.30
3	50.51	47.67	45.21
4	59.62	53.24	44.78
5	70.72	65.32	54.66
6	77.98	75.19	65.00
7	82.52	82.58	74.21
8	85.29	87.15	81.07
9	87.10	89.25	86.85
10	88.09	89.90	90.35
11	88.71	90.18	92.40
12	89.04	90.15	93.02
13	89.20	89.98	92.83
14	89.37	89.80	92.65
15	89.57	89.57	92.42

In Table 21, cable strength is calculated taking into account the relative tensional state after the section cut and the relative inclination from the horizontal.

Table 21. Summary of verification results for tangential stresses, suspended span beam.

Section	Progressive	V_R	$V_{t.ref}$	V_{tot}
[-]	[m]	[kN]	[kN]	[kN]
M	0.95	4781.54	872.49	5654.04
N	3.95	2656.42	1357.18	4013.60
O	7.625	2656.42	560.63	3217.05
P	15.25	2656.42	0	2656.42

The shear cracking strength can be calculated by the formula:

$$V_{fess} = 0.7 \cdot b_w \cdot d \cdot \left(f_{ctm}^2 + \sigma_{cp} f_{ctm}\right)$$

The relative strengths in the different sections are:

Section	Progressive	V_{fess}
[-]	[m]	[kN]
M	0.95	2306.92
N	3.95	1260.65
O	7.625	1290.13
P	15.25	1341.45

Because the shear forces go beyond the beam's shear capacity (steel in the elastic domain with concrete crushing), the study on the ultimate bending capacity revealed that the beam has a brittle failure mechanism. Therefore, it is suggested to prepare a test with the aim of studying the shear behavior of the beam by investigating failure in the stirrup refinement zone and in the zones with current stirrup spacing (this assumes the need to move the beam during the tests).

Test 1: Shear failure in the stirrup refinement zones.

Shear span length: 3.95 m from the support.

Maximum Load: 5500 kN

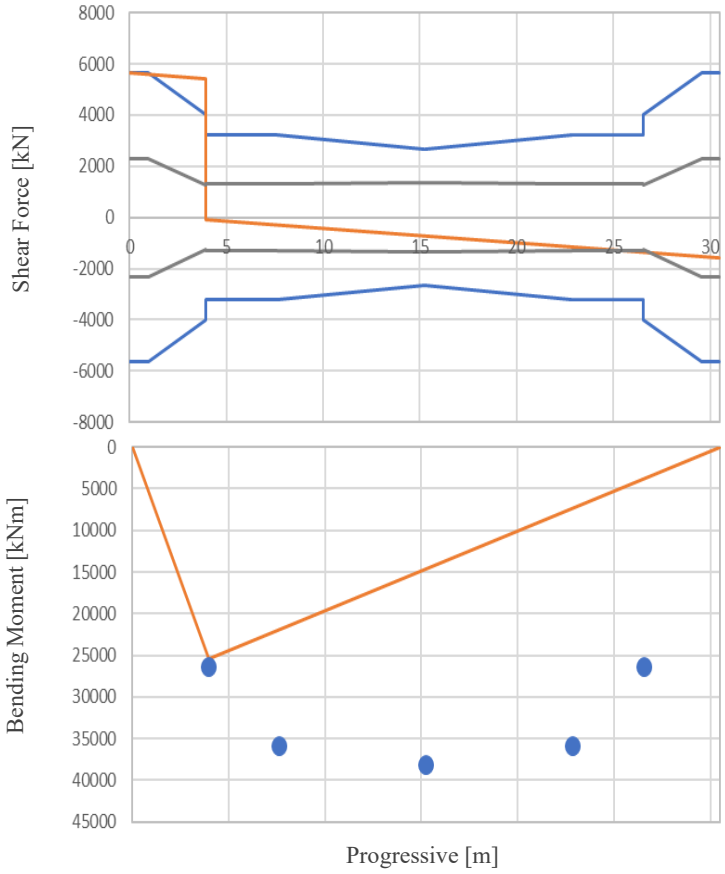

Figure 116. Shear and bending capacity of the beam (blue) versus external shear and bending forces (orange).

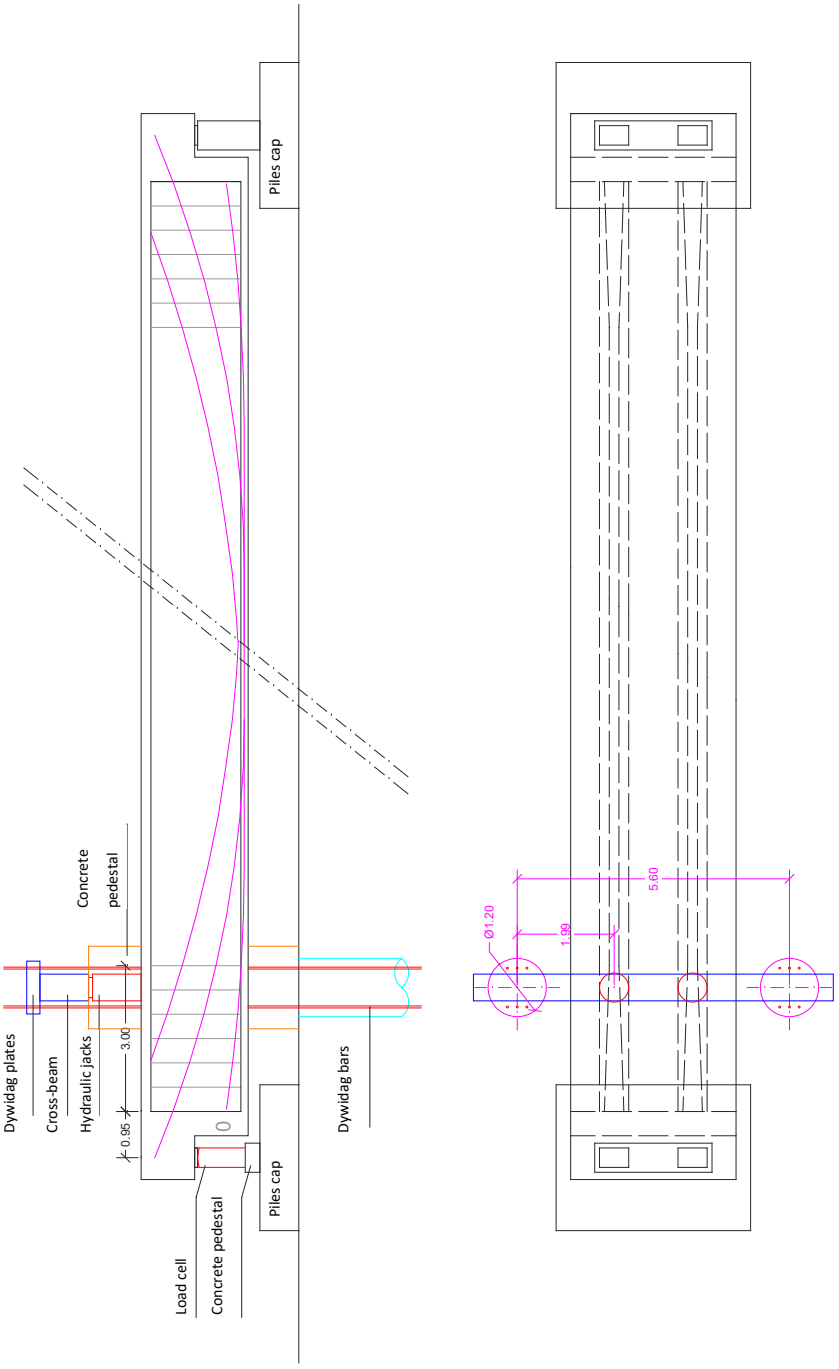

Figure 117. Test 1 scheme (length unit expresses in meters).

Test 2: Shear failure in the zones with current stirrup spacing.

Shear span length: 10 m from the support.

Maximum Load: 3500 kN

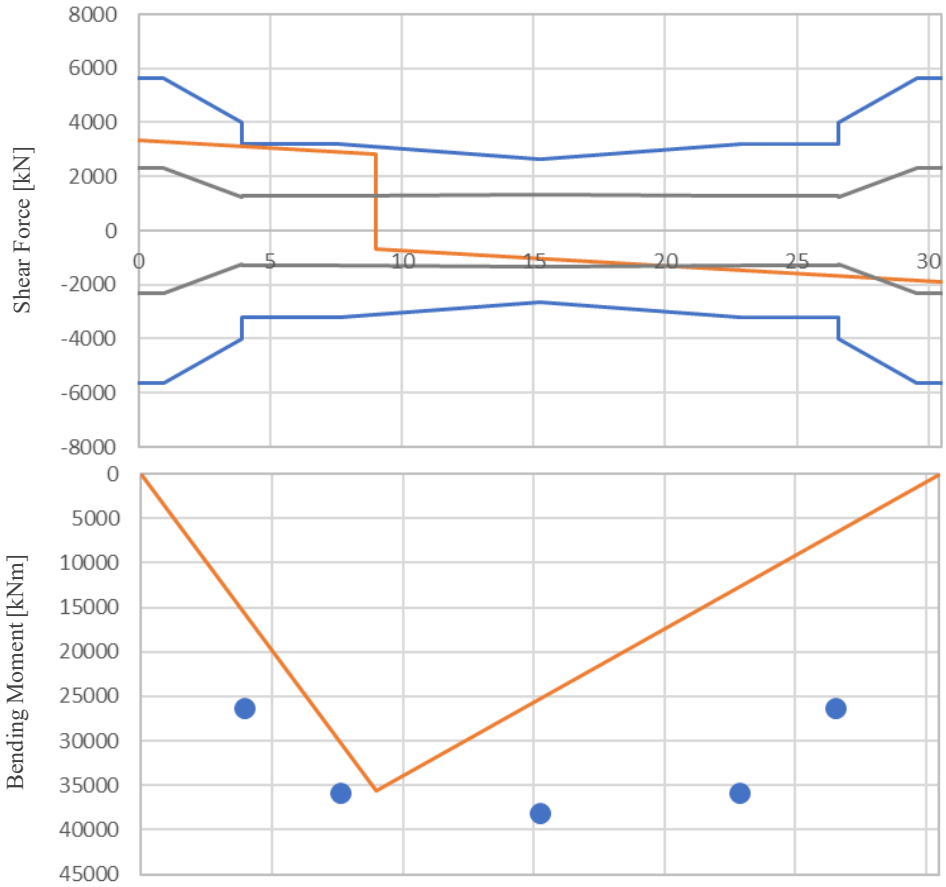

Figure 118. Shear and bending capacity of the beam (blue) versus external shear and bending forces (orange).

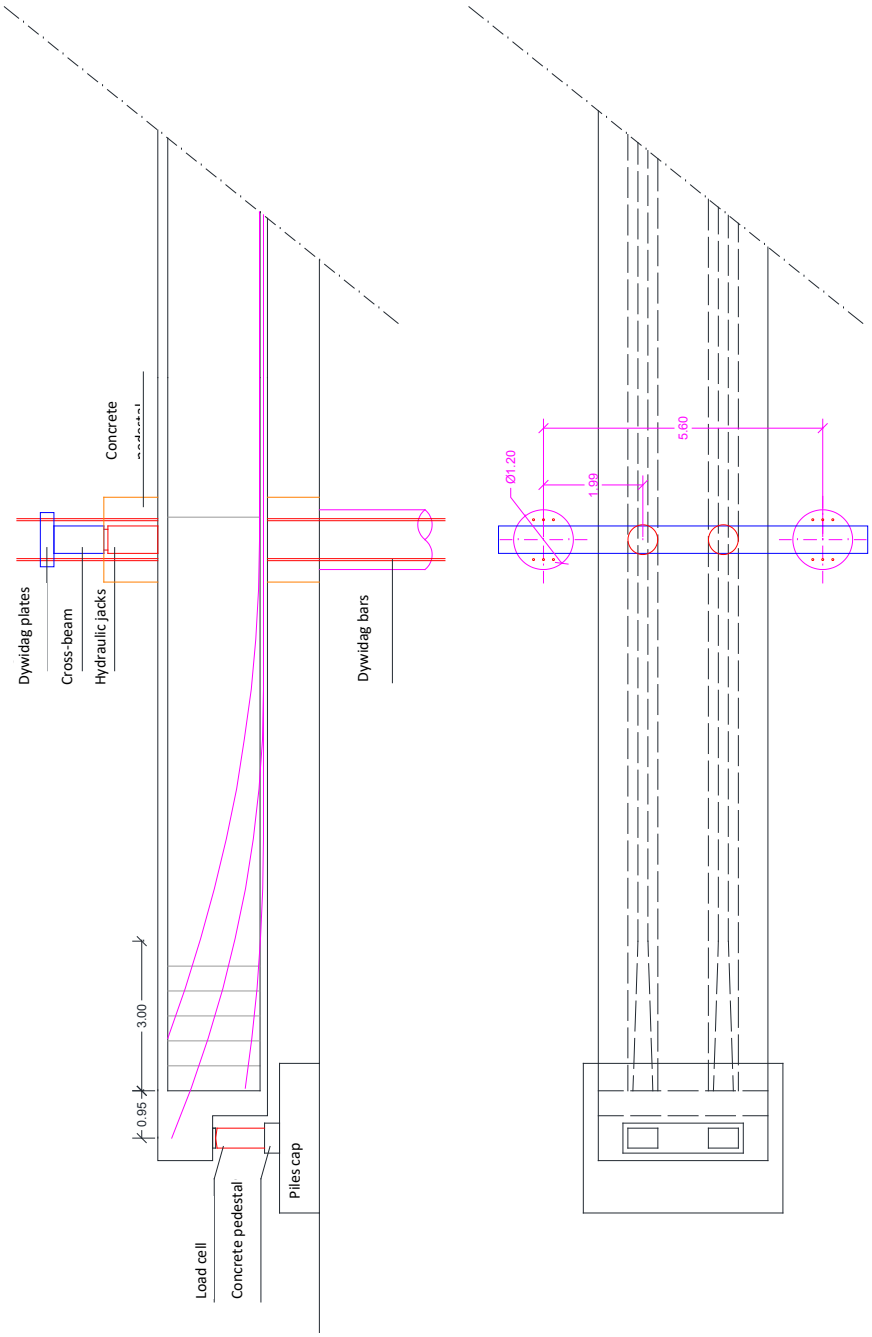

Figure 119. Test 2 scheme.

The contrast is to be provided by 2 tension piles with embedded Dywidag 40WR bars, characterized by an ultimate load of 1320 kN. Assuming as safety factor a value of 2, these are the results, considering the maximum capacity of the jacks of 5000 kN:

$T_p = 5000\ kN$ Tensile force of the pile

$F_u = \frac{1320}{2} = 660\ kN$ Ultimate load Dywidag

$N = \frac{5000}{660} = 7.57 \rightarrow 8$ Total number of bars/pile

Forces on the crossbeam are calculated taking into account the static scheme (4-point bending) and the maximum load transmissible by the jacks.

$P_u = 5000\ kN$ External load

$L = 1.99 \cong 2\ m$ Shear span length

$V_{max} = 5000\ kN$ Maximum shear force

$M_{max} = 10000\ kNm$ Maximum bending moment

By assuming a crossbeam height of 1 m and a steel class of S355, the minimum area of the flange is:

$A_{fl,req} = \frac{1E10/1E3}{355} 1.05 = 29578\ mm^2$ Minimum flange area

A flange section of 800 x 40 mm (Area: 32000 mm^2) with a safety factor of 1.08 is chosen. The minimum area of the webs is:

$A_{w,req} = \frac{5E6}{355} 1.05 \cdot \sqrt{3} = 25615\ mm^2$ Minimum web area

A web section of 920 x 15 mm (Area: 27600 mm^2) with a safety factor of 1.08 is chosen.

Finally, the weight of the crossbeam is estimated:

$A_c = 2.05\ m^2$	Current cross-section area
$L_c = 22.6\ m$	Current cross-section length
$A_r = 2.37\ m^2$	Average increased area
$L_r = 3.0\ m$	Increased area length
$A_{app} = 2.09\ m^2$	Support cross-section area
$L_{app} = 3.4\ m$	Crossbeam width
$A_{diaf} = 7.48\ m^2$	Gross section area
$L_{diaf} = 3 \cdot 0.2 = 0.6\ m$	Gross section area length

The expected weight of the crossbeam is calculated as:

$$\left[A_c \cdot \left(L_c - L_{diaf}\right) + A_r \cdot L_r + A_{app} \cdot L_{app} \cdot 2 + A_{diaf} \cdot L_{diaf}\right] \cdot 2.5 = 177.3\ t$$

The calculation of the load capacity of the dapped-beam ends is provided below. For the verification of the dapped end, a schematization of the structural element is used with strut-and-tie models based on the actual geometry of the reinforcement provided in the detailed construction design. Geometrically, the dapped end consists longitudinally of a full cross-section nib with a thickness of 0.90 m, followed by a full diaphragm with a thickness

of 0.50 m (Figure 120.). In the transverse direction, the dapped end is symmetrical with respect to the vertical axis and rests on two support devices arranged at a spacing of 3.40 m.

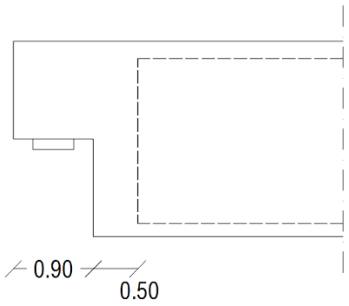

Figure 120. Geometric details of the dapped-beam ends.

Given the geometry of the box girder, the reinforcement differs depending on whether it is located in the position of the webs or in the areas between them (cells). In the following calculations, reference will be made only to the reinforcement in the webs, considering that the supports of the tested beam will be arranged beneath from them. Figure 121 shows the reinforcements in the webs, specified in Table 22 for web 2 and 3.

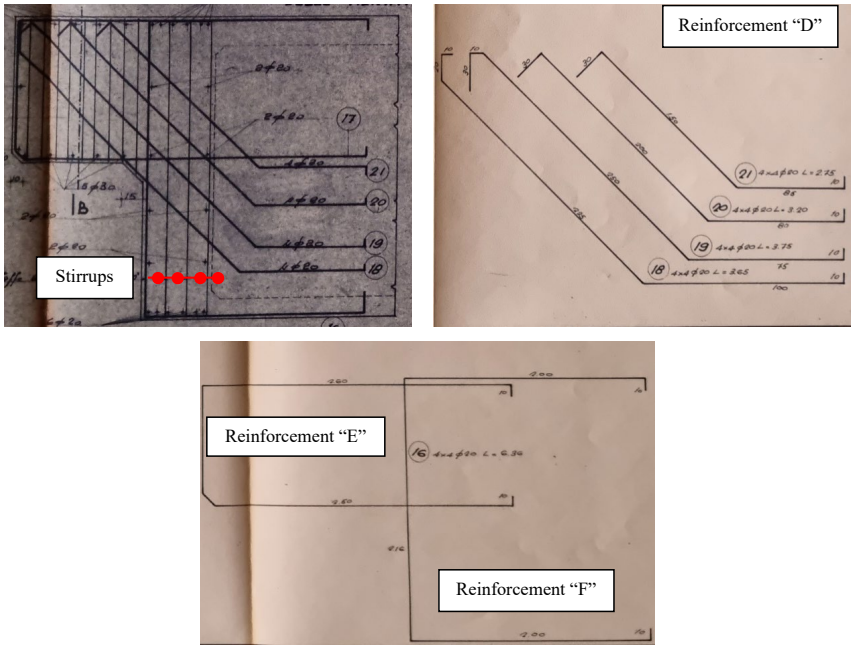

Figure 121. Reinforcement layout of the dapped end.

Table 22. Reinforcements of the dapped end webs.

	WEB 2		WEB 3	
ID	**n**	**φ**	**n**	**φ**
[-]	[-]	[cm]	[-]	[cm]
D	16	20	16	20
E	5	20	5	20
F	4	20	4	20

The stirrups characterized by four-legged Φ14/20, identified in Figure 121 with the label “Stirrups,” are added to the defined reinforcements. Given the size of the reinforcements, it can be observed that their placement is compatible with the development of the strut-and-tie model proposed by EC2, shown inFigure 122. The standard allows to evaluate the two models

independently and combine them to calculate the capacity by using the superposition of effects.

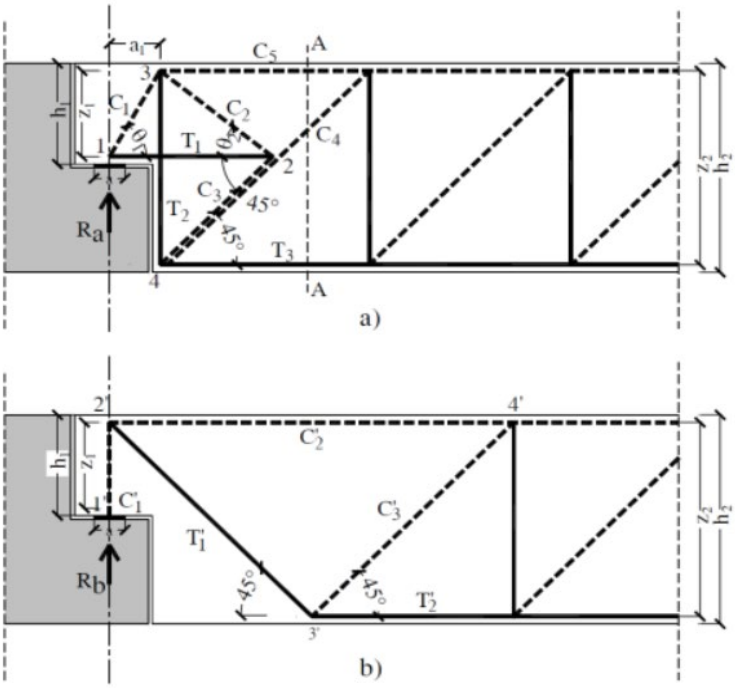

Figure 122. Stut-and-tie models proposed by the EC2 standards.

In the tables below, the capacity of the resistant mechanisms of the dapped end is calculated:

Model A

Section	**VERTICAL REINFORCEMENTS**						**HORIZONTAL REINFORCEMENTS**					
	A	**θ_1**	**θ_2**	**f_{yd}**	**T_2**	**$V_{Rd,2}$**	**A**	**θ_1**	**f_{yd}**	**T_1**	**$V_{Rd,1}$**	**$V_{Rd,A}$**
	[cm²]	[°]	[°]	[MPa]	[kN]	[kN]	[cm²]	[°]	[MPa]	[kN]	[kN]	[kN]
Webs	37.68	63.67	71	432.93	1631.28	1192.35	31.4	60	432.93	1359.40	2354.55	1192.35

Model B					
Section	DIAGONAL REINFORCEMENTS				
	A	**θ**	**f_{yd}**	**T_2**	**$V_{Rd,B}$**
	[cm^2]	[°]	[MPa]	[kN]	[kN]
Webs	50.24	45	432.93	2175.04	1537.99

The capacity of one web results equals to 2730.33 kN; therefore, the total strength of the two webs is 5460.66 kN; the latter is comparable to the web strength in the refinement stirrups zone, which is 5654 kN.

6 Conclusions

The thesis dealt with the application of the new bridge guidelines to define the attention class for a set of bridges within the research project between the inter-university consortium FABRE and the road owner ANAS. Visual inspections brought to light the main problems of existing bridges. In order to accurately assess the attention class of the structure and the structural safety in general, the investigation of defects plays a key role. Identifying defects and criticalities on post-tensioned cable-stayed bridges with dapped ends, i.e., bridges composed of two critical elements, proved not to be easy since the major defects are concealed by the geometry of the element.

The rupture behavior of dapped-end beams has been investigated in the literature, focusing on the analytical models adopted for the evaluation of the ultimate capacity and the collapse mechanisms investigated through laboratory experimental campaigns. The experimental investigations available in the literature mainly focused on the study of the influence of parameters such as the relative shear span, the reinforcement layout, and the presence of defects on the element bearing capacity. However, they did not evaluate the influence of the tensioning level on the ultimate capacity in prestressed dapped-end beams.

With the objective of investigating the failure behavior of beams prestressed with dapped ends, an extensive experimental campaign was designed that includes laboratory tests on scaled samples and in-situ tests on an existing bridge girder. The design of the experimental campaign in the laboratory was supported by numerical analyses with strut-and-tie models and more refined

finite element analyses with the objective of evaluating the expected capacity of the elements and defining the appropriate test methodology for the study of the ultimate bearing capacity.

The expected ultimate capacity was evaluated by performing a parametric analysis on the finite element model to assess the influence of the parameters such as the concrete fracture energy and the shear span length.

The results of the parametric analysis indicate that the ultimate capacity of the dapped-end beam specimens is not significantly affected by the parameters investigated, namely the shear span length and the concrete fracture energy.

Further analysis of the first parameter revealed that the assumed minimum shear span value of 600 mm was sufficient to avoid the formation of the resistant arch mechanism that would lead to an overestimation of the dapped end strength. For larger values of shear span, the developed resistant mechanism remained unchanged and the collapse did not shift toward the bending fracture of the beam, demonstrating the effectiveness of the design of the beam shear and bending reinforcement.

The fracture energy has a minor influence on the ultimate capacity of the dapped-beam end. Indeed, a small increase in ultimate capacity is noted as the fracture energy increases, which remains for all cases analyzed below the maximum value of 3.29%.

For the evaluation of the expected ultimate capacity, shear span and fracture energy values of 800 mm and 70 N/m, respectively, were chosen.

The studies highlight that the failure mechanism starts at the re-entrant corner of the nib. A crack, angled at 45 degrees, initiates from this location and extends towards the point where the load is applied. When observing the build-up of plastic deformation in the concrete, it becomes apparent that a substantial region near the internal corner is influenced by plasticity events.

At the ultimate load stages, the diagonal, horizontal, and vertical primary bars undergo significant hardening. The yielding process starts to engage the vertical and horizontal reinforcements positioned along the zone of concrete cracking.

The analysis of the expected ultimate capacities for the various specimens shows that:

- a reduction of 16% of the prestressing level does not affect the ultimate capacity.

- The complete loss of prestressing (RL-A3) bring a 16% reduction of the ultimate capacity compared to the maximum value obtained for the specimens RL-A1 and RL-A2.

- Localized damages on the main dapped end reinforcement (RL-A1D) causes a greater decrease in capacity (19.63 %) than reduction of stirrups (RL-B1).

- Strut-and-tie models were found to be too conservative for a correct estimation of specimen capacity.

Future developments

The laboratory tests and the experimental campaign on the existing bridge will be completed and the data collected will be analyzed. The conclusion of the experimental campaigns will be essential to evaluate the goodness of the numerical results and validate the adopted modelling techniques.

Further in-depth studies on the prestressed dapped-end beams may concern:

- the non destructive tests reliability on existing prestressed bridges in particular to assess the physical condition and the residual prestressing level in the prestressing wires.
- The dynamic monitoring systems which can be installed on dapped-beam ends to predict possible collapse mechanisms.

References

[1] Mitchell D, Marchand J, Croteau P, Cook WD. Concorde Overpass Collapse: Structural Aspects. J Perform Constr Facil 2011;25:545–53. https://doi.org/10.1061/(ASCE)CF.1943-5509.0000183.

[2] di Prisco M, Colombo M, Martinelli P, Coronelli D. The technical causes of the collapse of Annone overpass on SS.36 Le cause tecniche del crollo del cavalcavia di Annone 2018.

[3] Bazzucchi F, Restuccia L, Ferro G. Considerations over the Italian road bridge infrastructure safety after the Polcevera viaduct collapse: past errors and future perspectives. Frat Ed Integrità Strutt 2018;12:400–21. https://doi.org/10.3221/IGF-ESIS.46.37.

[4] Mattock AH, Chan TC. Design and Behavior of Dapped-End Beams. PCI J 1979;24:28–45. https://doi.org/10.15554/pcij.11011979.28.45.

[5] Liem SK. Maximum shear strength of dapped-end or corbel. masters. Concordia University, 1983.

[6] Chen B, Hangenberger M, Breen J. Evaluation of Strut-and-Tie Modeling Applied to Dapped Beam with Opening. ACI Struct J 2002;99. https://doi.org/10.14359/12113.

[7] Lin I-J, Hwang S-J, Lu W-Y, Tsai J-T. Shear strength of reinforced concrete dapped-end beams. Struct Eng Mech 2003;16:275–94.

[8] Lu W, Lin I, Hwang S, Lin Y. Shear strength of high-strength concrete dapped-end beams. J Chin Inst Eng 2003;26:671–80. https://doi.org/10.1080/02533839.2003.9670820.

[9] Wang Q, Guo Z, Hoogenboom PCJ. Experimental investigation on the shear capacity of RC dapped end beams and design recommendations. Struct Eng Mech 2005;21:221–35. https://doi.org/10.12989/sem.2005.21.2.221.

[10] Lu W-Y, Lin I-J, Yu H-W. Behaviour of reinforced concrete dapped-end beams. Mag Concr Res 2012;64:793–805. https://doi.org/10.1680/macr.11.00116.

[11] Aswin M, Mohammed BS, Liew MS, Syed ZI. Shear Failure of RC Dapped-End Beams. Adv Mater Sci Eng 2015;2015:e309135. https://doi.org/10.1155/2015/309135.

[12] Lu W-Y, Chen T-C, Lin I-J. Shear strength of reinforced concrete dapped-end beams with shear span-to-depth ratios larger than unity. J Mar Sci Technol 2015;23. https://doi.org/10.6119/JMST-015-0511-1.

[13] Desnerck P, Lees JM, Morley CT. Impact of the reinforcement layout on the load capacity of reinforced concrete half-joints. Eng Struct 2016;127:227–39. https://doi.org/10.1016/j.engstruct.2016.08.061.
[14] Oviedo R, Gutiérrez S, Santa María H. Experimental evaluation of optimized strut-and-tie models for a dapped beam. Struct Concr 2016;17:469–80. https://doi.org/10.1002/suco.201500037.
[15] Desnerck P, Lees JM, Morley CT. The effect of local reinforcing bar reductions and anchorage zone cracking on the load capacity of RC half-joints. Eng Struct 2017;152:865–77. https://doi.org/10.1016/j.engstruct.2017.09.021.
[16] Desnerck P, Lees JM, Morley CT. Strut-and-tie models for deteriorated reinforced concrete half-joints. Eng Struct 2018;161:41–54. https://doi.org/10.1016/j.engstruct.2018.01.013.
[17] Mata-Falcón J, Pallarés L, Miguel PF. Proposal and experimental validation of simplified strut-and-tie models on dapped-end beams. Eng Struct 2019;183:594–609. https://doi.org/10.1016/j.engstruct.2019.01.010.
[18] Özkılıç YO, Aksoylu C, Arslan MH. Experimental and numerical investigations of steel fiber reinforced concrete dapped-end purlins. J Build Eng 2021;36:102119. https://doi.org/10.1016/j.jobe.2020.102119.
[19] Rajapakse C, Degée H, Mihaylov B. Investigation of shear and flexural failures of dapped-end connections with orthogonal reinforcement. Eng Struct 2022;260:114233. https://doi.org/10.1016/j.engstruct.2022.114233.
[20] Aksoylu C, Özkılıç YO, Arslan MH. Experimental and numerical investigation of shear strength at dapped end beams having different shear span and recess corner length. Structures 2023;48:79–90. https://doi.org/10.1016/j.istruc.2022.12.076.
[21] Di Carlo F, Meda A, Molaioni F, Rinaldi Z. Experimental evaluation of the corrosion influence on the structural response of Gerber half-joints. Eng Struct 2023;285:116052. https://doi.org/10.1016/j.engstruct.2023.116052.
[22] Werner MP. SHEAR DESIGN OF PRESTRESSED CONCRETE STEPPED BEAMS. PCI J 1973;18:37–49. https://doi.org/10.15554/pcij.07011973.37.49.
[23] Mader DJ. Detailing Dapped Ends of Pretensioned Concrete Beams. University of Texas, 1990.

[24] Nanni A, Huang P-C. Validation of an Alternative Reinforcing Detail for the Dapped Ends of Prestressed Double Tees. PCI J 2002;47:38–49. https://doi.org/10.15554/pcij.01012002.38.49.
[25] Moreno-Martínez JY, Meli R. Experimental study on the structural behavior of concrete dapped-end beams. Eng Struct 2014;75:152–63. https://doi.org/10.1016/j.engstruct.2014.05.051.
[26] Ministero delle Infrastrutture e della Mobilità Sostenibili. Linee Guida per la classificazione e gestione del rischio, la valutazione della sicurezza ed il monitoraggio dei ponti esistenti 2022.
[27] ANSFISA. Istruzioni Operative per l'applicazione delle Linee Guida per la classificazione e gestione del rischio, la valutazione della sicurezza ed il monitoraggio dei ponti esistenti 2022.
[28] FABRE. Ispezioni speciali su selle Gerber di ponti esistenti in c.a. e c.a.p. ai sensi delle Linee Guida: la conoscenza e la verifica locale. 2022.
[29] FABRE. Compendio: Ispezioni speciali su ponti esistenti in c.a.p. a cavi scorrevoli ai sensi delle Linee Guida: la classificazione e la valutazione accurata 2023.
[30] Ministero delle Infrastrutture e dei Trasporti. Aggiornamento delle Norme tecniche per le costruzioni 2018.
[31] Federal Highway Administration. Guidelines for Sampling, Assessing, and Restoring Defective Grout in Prestressed Concrete Bridge Post-Tensioning Ducts 2013.
[32] Institute PC. PCI design handbook: Precast and prestressed concrete. Precast/Prestressed Concrete Institute; 1971.
[33] Leonhardt F, Mönnig E. Vorlesungen über Massivbau. Berlin, Heidelberg: Springer; 1973. https://doi.org/10.1007/978-3-662-07601-9.
[34] Leonhardt F, Mönnig E. Calcolo di progetto & tecniche costruttive: L'armatura nelle costruzioni in cemento armato. vol. 3. I. Milano: Edizioni Tecniche ET; 1997.
[35] Mattock AH. Design proposals for reinforced concrete corbels. PCI J 1976;21:18–42. https://doi.org/10.15554/pcij.05011976.18.42.
[36] Schlaich J, Schafer K, Jennewein M. Toward a Consistent Design of Structural Concrete. PCI J 1987;32:74–150. https://doi.org/10.15554/pcij.05011987.74.150.
[37] Mitchell D, Cook WD. Design of disturbed regions. Struct. Concr., 1991, p. 1. https://doi.org/10.5169/seals-47682.
[38] Consiglio Nazionale Delle Ricerche. Mensole tozze e selle Gerber: C.N.R. 10037/86 1992.

[39] Muttoni A, Schwartz J, Thürlimann B. Design of Concrete Structures with Stress Fields. Basel: Birkhäuser; 1996. https://doi.org/10.1007/978-3-0348-9047-2.
[40] Asso R, Domaneschi M, Marano GC, Palmisano F, Palombella G. Behavior of Half-Joints: Design and Simulation of Laboratory Tests. Infrastructures 2022;7:160. https://doi.org/10.3390/infrastructures7120160.
[41] Rosso MM, Asso R, Aloisio A, Di Benedetto M, Cucuzza R, Greco R. Corrosion effects on the capacity and ductility of concrete half-joint bridges. Constr Build Mater 2022;360:129555. https://doi.org/10.1016/j.conbuildmat.2022.129555.
[42] Buckingham E. On Physically Similar Systems; Illustrations of the Use of Dimensional Equations. Phys Rev 1914;4:345–76. https://doi.org/10.1103/PhysRev.4.345.
[43] Kim S, Choi SW. Experimental and Analytical Investigation Based on 1/2 Scale Model for a Cleanroom Unit Module Consisting of Steel Section and Reinforced Concrete. Adv Mater Sci Eng 2016;2016:1–11. https://doi.org/10.1155/2016/6920725.
[44] Martin BT, Sanders DH. Verification and implementation of strut-and-tie model in LRFD bridge design specifications. AASHTO Highw Subcomm Bridge Struct 2007.
[45] European Committee for Standardization (CEN). EN 1992-2-1 Eurocode 2: Design of concrete structures - Part 1-2: General rules - Structural fire design 2008.
[46] Maekawa K, Vecchio F, Bayrak O, Bentz E, Blaauwendraad J, Cervenka J, et al. fib Bulletin 45. Practitioners' guide to finite element modelling of reinforced concrete structures. fib. The International Federation for Structural Concrete; 2008. https://doi.org/10.35789/fib.BULL.0045.
[47] Highways England. CS 466 Risk management and structural assessment of concrete half-joint deck structures. 2020.
[48] Palmisano F, Asso R, Chiaia B, Marano GC, Pellegrino C. Structural assessment of existing R.C. half-joint bridges according to the new Italian guidelines. J Civ Struct Health Monit 2022. https://doi.org/10.1007/s13349-022-00652-7.
[49] Priestley MJN, Calvi GM, Kowalsky MJ. Displacement-based seismic design of structures. Pavia, Italy: IUSS Press : Distributed by Fondazione EUCENTRE; 2007.
[50] Fib Special Activity Group NMC, Taerwe L, Matthys S. fib model code for concrete structures 2010 2013.

[51] Committee A, others. ACI 318-19: Building Code Requirements for Structural Concrete and Commentary. Am Concr Inst Farmington Hills MI USA 2019.
[52] ANSYS Inc. ANSYS Mechanical version 2023 R2 User's Guide 2023.
[53] Menetrey P, Willam KJ. Triaxial Failure Criterion for Concrete and its Generalization. ACI Struct J 1995;92. https://doi.org/10.14359/1132.
[54] William KJ, Warnke EP. CONSTITUTIVE MODEL FOR THE TRIAXIAL BEHAVIOR OF CONCRETE, 1975.
[55] Drucker DC, Prager W. Soil mechanics and plastic analysis or limit design. Q Appl Math 1952;10:157–65.
[56] Concrete F-IF for S. CEB-FIP Model Code 1990: Design Code. fib Fédération internationale du béton; 1993.
[57] Yao F, Chu J, Lu X. Improved stack imaging of spectral amplitude based on the impact echo method for identification of defects in grout-filled lap connection. Constr Build Mater 2023;398:132420. https://doi.org/10.1016/j.conbuildmat.2023.132420.
[58] Terzioglu T, Karthik MM, Hurlebaus S, Hueste MBD, Maack S, Woestmann J, et al. Nondestructive evaluation of grout defects in internal tendons of post-tensioned girders. NDT E Int 2018;99:23–35. https://doi.org/10.1016/j.ndteint.2018.05.013.
[59] Muldoon R, Chalker A, Forde MC, Ohtsu M, Kunisue F. Identifying voids in plastic ducts in post-tensioning prestressed concrete members by resonant frequency of impact–echo, SIBIE and tomography. Constr Build Mater 2007;21:527–37. https://doi.org/10.1016/j.conbuildmat.2006.04.009.
[60] Hao J, Tan Z, Lu H, Deng S, Shen F, Zhao D, et al. Residual stress measurement system of the general purpose powder diffractometer at CSNS. Nucl Instrum Methods Phys Res Sect Accel Spectrometers Detect Assoc Equip 2023;1055:168532. https://doi.org/10.1016/j.nima.2023.168532.
[61] Wagner JN, Hofmann M, Wimpory R, Krempaszky C, Stockinger M. Microstructure and temperature dependence of intergranular strains on diffractometric macroscopic residual stress analysis. Mater Sci Eng A 2014;618:271–9. https://doi.org/10.1016/j.msea.2014.09.033.
[62] In-situ stress measurement with the canmet portable x-ray stress diffractometer: Nondestructive characterisation of materials 2, Montreal (Canada), 21–23 Jul, 1986. pp. 615–624. Edited by J.F. Bussiere, J.P. Monchalin, C.O. Ruud, R.E. Green Jr. Plenum Press, 1987. NDT Int 1989;22:367. https://doi.org/10.1016/0308-9126(89)91163-2.